Graduate Theses, Dissertations, and Problem Reports

2016

Investigations into the nature of magnetism in transition-metal-phthalocyanines

Zhengjun Wang

Follow this and additional works at: https://researchrepository.wvu.edu/etd

Recommended Citation

Wang, Zhengjun, "Investigations into the nature of magnetism in transition-metal-phthalocyanines" (2016). *Graduate Theses, Dissertations, and Problem Reports*. 6906.
https://researchrepository.wvu.edu/etd/6906

INVESTIGATIONS INTO THE NATURE OF MAGNETISM IN TRANSITION-METAL-PHTHALOCYANINES

Zhengjun Wang

Dissertation submitted to the
Eberly College of Arts and Sciences
at West Virginia University

in partial fulfillment of the requirements for the degree of

Doctor of Philosophy
in
Physics

Mohindar S. Seehra, Ph.D., Chair
Leonardo Golubovic, Ph.D.
Alan D. Bristow, Ph.D.
Edward Flagg, Ph.D.
Dimitris Korakakis, Ph.D.

Department of Physics and Astronomy

Morgantown, West Virginia
2016

ABSTRACT

INVESTIGATIONS INTO THE NATURE OF MAGNETISM IN TRANSITION-METAL-PHTHALOCYANINES

Zhengjun Wang

In this dissertation, the nature of magnetism in transition-metal-doped phthalocyanines (TMPc, TM = Co, Ni, Cu, V, and Mn, chemical formula: $C_{32}H_{16}N_8TM$) is investigated by measuring their magnetization (M) and ac susceptibilities in magnetic fields up to 90 kOe and covering the wide temperature range of 0.5 K to 300 K. These low temperatures and high magnetic field measurements combined with detailed analysis of the data have provided new information about the nature of magnetism of TMPc. The powder samples used here were structurally characterized using x-ray diffraction and scanning electron microscopy.

TMPc are a class of organic semiconductors with potential applications in spintronics and they are planar molecules with the TM atom at the center bound to four N atoms and forming a linear chain along the monoclinic b-axis. Because of this symmetry, the ground states of TMPc often violate the Hunds' rules; e.g. the S = 3/2 state for d^5 Mn(II) in β-MnPc, S = 1/2 state for the d^7 Co(II) in β-CoPc, and S = 0 state for the d^8 Ni(II) in NiPc. The magnetic properties of TMPc are also affected by the stack angle δ between the orientation of the molecular plane and the b-axis, δ being 65° (45°) for α (β) phase.

For both α-CuPc and β-CuPc, M vs. T data fit well with the Bonner-Fisher model for S = 1/2 antiferromagnetic (AFM) Heisenberg linear chain yielding the Cu^{2+}-Cu^{2+} exchange constant J_{ex}/k_B = - 1.7 K (- 0.2 K) for α-CuPc(β-CuPc). This order of magnitude difference in J_{ex}/k_B is likely due to the smaller Cu^{2+}-Cu^{2+} distance in α-phase than in β-phase. The M vs. H at 2 K and 5 K data are interpreted including the effect of the exchange coupling.

For β-CoPc, the predicted peak in χ vs. T data by Bonner-Fisher model was observed at T_{max} = 1.9 K for the first time yielding the Heisenberg exchange constant J_{ex}/k_B = - 1.5 K between the Co^{2+}-Co^{2+} ions. The isothermal data of M vs. H at 1 K shows good agreement with the Bonner-Fisher model; M vs. H at 5 K data is interpreted by including the effect of the exchange interaction.

For VOPc (phase II), the analysis of the M vs. T data shows VO^{2+} electronic state with spin S = 1/2 and θ = - 0.1 indicates a very weak AFM exchange coupling between neighboring VO^{2+} ions which implies the near-perfect paramagnetism of VOPc. This conclusion is also supported by the analysis of the M vs. H data at several temperatures. The diamagnetic nature of β-NiPc corresponding to the S = 0 state for the $3d^8$ Ni(II) is confirmed by measurements and analysis of the magnetization with temperature-independent susceptibility χ_D = - 3.38 $\times 10^{-7}$ emu/gOe. The observed ferromagnetic component in the β-NiPc powder sample is identified with Fe impurity.

For β-MnPc with S = 3/2, detailed analysis of the dc and ac susceptibilities leads to the conclusion of the absence of 3-dimensional long range magnetic ordering in this system contrary to previous reports. This conclusion is supported by the Arrott plots and lack of a peak in the ac

susceptibilities and specific heat near the quoted $T_C \approx 8.6$ K. Instead, β-MnPc is best described as an Ising-like chain magnet with Arrhenius relaxation of the magnetization governed by an intra-layer ferromagnetic exchange constant $J_{ex}/k_B = 2.6$ K and the single ion anisotropy energy constant $|D|/k_B = 8.3$ K. The absence of 3D long-range ordering is consistent with the measured $|D|$ being $>J_{ex}$.

DEDICATION

To my parents Mr. Yubin Wang and Mrs. Lanying Fan

and

my mentor Prof. Mohindar S. Seehra

ACKNOWLEDGEMENTS

TABLE OF CONTENTS

LIST OF FIGURES

LIST OF TABLES

CHAPTER 1.

Introduction

1.1 Organic Materials in Technology

For the past several decades, organic materials including small molecules and polymers have been of great interest for their fundamental physical properties as well as for their applications in various electronic devices. The main advantages of organic materials compared to their inorganic counterparts are the compatibility with flexible substrates and low-temperature, low-cost fabrication processes such as thermal evaporation, spin coating, and printing. Also, organic materials can be deposited on flexible, light-weight, and large area substrates which offers the possibilities of practical applications. Moreover, both physical and chemical properties can be tailored by manipulating ligands or functional groups, offering the way for scientists and engineers to design molecules with desired properties. A number of organic materials [Alq$_3$ (Al (C$_9$H$_6$NO$_3$)$_3$), Pentacene, CuPc and indigo to name a few] have been used to fabricate various organic electronic devices such as organic spintronic devices, organic solar cells (OSC), organic light emitting diodes (OLED), organic thin film transistors (OTFT), organic memory devices, and organic bioelectronics devices [1-3]. On the other hand, although crystalline inorganic materials (e.g. metals and ionic crystals) have been well understood theoretically, physical properties of organic materials such as crystal structure, band structure, magnetic, optical, and electrical properties still require a lot of theoretical and experimental research. Thus, organic materials offer scientists great opportunities to develop both theory and experimental techniques.

1.2 Introduction to Transition-Metal-Substituted Phthalocyanines (TMPc, TM = V, Fe, Co, Ni, Mn, and Cu)

Metal Phthalocyanines (MPc, chemical formula: $C_{32}H_{16}N_8M$) were successfully synthesized in the early 20th century and primarily used as pigments since then. Due to their strong absorption in the visible region and high fastness to light, weathering and numerous solvents, MPcs are used in nearly all fields of pigment industry, such as coatings, coloration of plastics, textile printing and so on. Over seventy MPc have been synthesized by placing different metal ions in the central cavity of Pc and among all the MPc, Copper Phthalocyanines (CuPc), including the chloro and bromo derivatives (important green organic pigments), are the predominant pigments.

Driven by the pigment industry, much emphasis was placed on the synthesis of different MPc molecules at the early stage without attention to their physical properties, and molecular and crystal structure. This did not change until Linstead et al. at the University of London proposed the molecular structure of MPc in 1930s [4-5]. This was soon confirmed using X-ray diffraction (XRD) by Robertson [6-7]. Other fundamental physical properties of MPcs such as optical, magnetic, and electrical properties have been investigated since the 1940s. Actually, MPc are one of the key materials for molecular physics due to their simplicity of molecular structure.

If a transition-metal (TM) atom is substituted in the center of the molecule, TMPc carry a magnetic moment because of the unpaired spin of the transition-metal atom. Transition-metal-substituted phthalocyanines (TMPc, M = V, Fe, Co, Ni, Mn, and Cu) have become materials of great interest recently not only for their unique physical properties but also for potential applications in spintronics and

2

optoelectronic devices [8-10]. One such possibility is discussed by Warner et al [10] where the use of CuPc thin films is proposed for spin-based information technology (spintronics) because of their relatively long population relaxation time T_1 (10 μs) and phase memory time T_2 (1 μs) at 80 K.

1.3 Molecular and Crystal Structure of TMPc

TMPc are planar molecules with a transition-metal atom bound at the center with four nitrogen atoms, as shown in Fig. 1.1(a). One of the interesting aspects of TMPc is their variety in crystal structure leading to different phases such as α, β, γ, etc. [11]. Different crystal structures have different properties, such as density, melting point, solubility, and color. Besides X-ray diffraction and neutron diffraction, Fourier Transform Infrared Spectroscopy (FTIR) and Electron Spin Resonance (ESR) can also be used to identify the crystal structure for TMPc [12]. This is because polymorphism leads to different inter-molecular interactions in the different crystal lattices leading to specific electronic and vibrational properties for each crystal form [13].
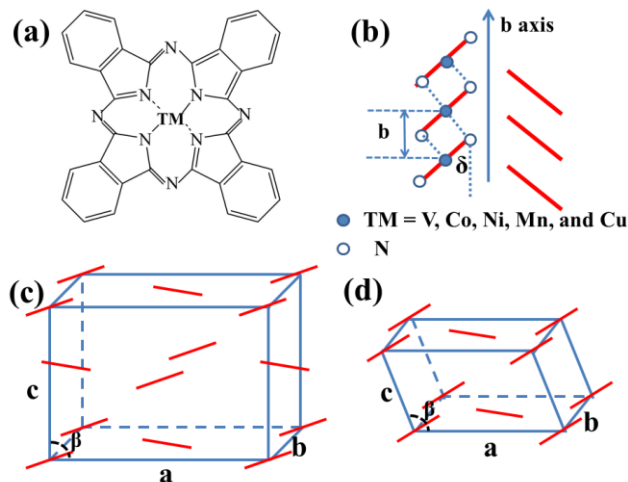
Fig. 1.1 *Molecular model (a), molecular arrangement (b), and unit cells (c and d) of α-TMPc and β-TMPc (adapted in part from Ref. 14). The red lines in the unit cell depict the orientation of the molecular plane and δ is the stack angle. The unit cell parameters of the various TMPc are listed in Table 1.1.*

Among these different crystal structures for TMPc, α-phase and β-phase are the most common phases as shown in Fig.1.1 (c) and (d). There are four and two molecules in each unit cell for the α-phase and β-phase, respectively. Usually, the β-phase TMPc is more stable than the α-phase since the latter can be converted to the β-phase by annealing in N_2 environment near 350 °C [11]. With regard to the nature of magnetism in TMPc, the distance between the nearest neighbor molecules along a-axis or c-axis is more than 1 nm which is too far for TM atoms to form the direct exchange coupling. However, the distance between the nearest neighboring molecules along the b-axis is only 0.3 nm to 0.5 nm which makes direct exchange coupling between TM atoms possible (Fig. 1.1b). Also, TM atoms along the b-axis may form superexchange coupling through nitrogen atom [15]. This is why TMPc are considered as one dimensional (1D) materials along the b-axis magnetically. Besides the distance between the nearest neighboring molecules, the other important parameter of both the α-phase and β-phase for magnetic properties is the magnitude of stack angle δ (Fig.1.1). In Table 1.1 lattice parameters for α-phase Copper Phthalocyanine (α-CuPc), β-CuPc, β-CoPc, β-MnPc, and β-phase Nickel Phthalocyanine (β-NiPc) are listed. The crystal structure for VOPc (phase II) is triclinic, which is different from the above mentioned materials and its lattice parameters are given in Chapter 6. A brief explanation of the space groups C2/c and $P2_1/c$ of Table 1.1 is given as a footnote [16].

Table 1.1 _Lattice parameters for α-CuPc, β-CuPc, β-CoPc, β-MnPc, and β-NiPc._

	α-CuPc	β-CuPc	β-CoPc	β-MnPc	β-NiPc
crystal structure	monoclinic	monoclinic	monoclinic	monoclinic	monoclinic
space group	C2/c	P2$_1$/a	P2$_1$/c	P2$_1$/c	P2$_1$/c
a (nm)	2.592	1.9407	1.4542	1.4576	1.490
b (nm)	0.379	0.479	0.4773	0.4755	0.470
c (nm)	2.392	1.4628	1.9352	1.9362	1.990
β (deg)	90.4	120.56	120.82	120.7	121.15
δ (deg)	65	45	45	45	45
Reference	[17]	[17]	ICDD # 02-061-3631	ICDD # 02-063-3894	ICDD # 00-011-0744

1.4 Electronic Structure of TMPc and Breakdown of the Hunds' Rules

The Hunds' rules as applied to electrons in a given shell of an atom affirm that electrons will occupy orbitals in such a way that the ground state is characterized by the following [18]: (i) The maximum value of the total spin S allowed by the exclusion principle; (ii) the maximum value of the

orbital angular momentum L consistent with this value of S; and (iii) the value of the total angular momentum J is equal to |L-S| when the shell is less than half full and to L + S when the shell is more than half full. When the shell is just half full, the application of the first rule gives L = 0, so that J = S. In Table 1.2, the predicted results according to the Hund's rules for the iron group ions with $3d^n$ configurations are listed [18]. As shown in Table 1.2, the spin S for Mn^{2+}, Ni^{2+}, and Co^{2+} should be 5/2, 1, and 3/2 respectively, according to Hunds' rules. However, the ground state of the TM ions in TMPc often violates Hunds' rules. Examples are the spin 3/2 intermediate state for the d^5 Mn^{2+} in β-MnPc, S = 0 state d^8 for Ni^{2+} in NiPc, and S = 1/2 state for d^7 Co^{2+} in β-CoPc [19-23]. According to ligand-field theory [24], the 3d electron energy levels of a TM atom (Fig.1.2) are split if it is placed into a D_{4h} symmetric environment, which is the case for TMPc. As a result, the $d_{x^2-y^2}$ level is pushed to much higher energy level (Fig. 1.3) and often is not occupied by electrons, and this causes the breakdown of Hunds' rules for TMPc.
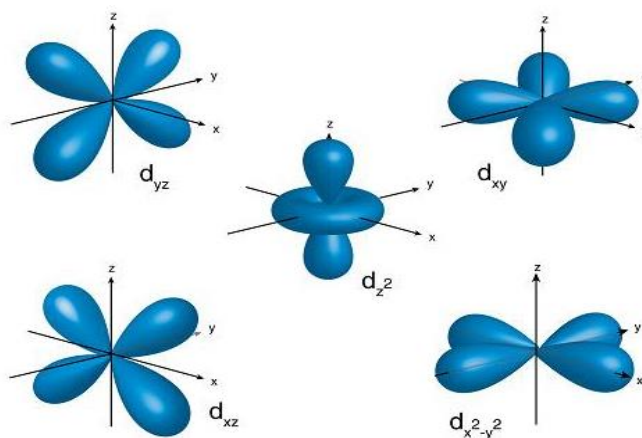
Fig. 1.2 *3d electron orbitals (adapted from http://socratic.org/ [25]).*

Table 1.2 *Electronic configuration, basic level, spin, and effective magneton numbers (p) for iron group*

ions [18].

Ion	Configuration	Basic level	Spin	p(cal) = $g[J(J+1)]^{1/2}$	p(cal) = $g[S(S+1)]^{1/2}$	p (exp)
Ti^{3+}, V^{4+}	$3d^1$	$^2D_{3/2}$	1/2	1.55	1.73	1.8
V^{3+}	$3d^2$	$^3F_2$	1	1.63	2.83	2.8
Cr^{3+}, V^{2+}	$3d^3$	$^4F_{3/2}$	3/2	0.77	3.87	3.8
Mn^{3+}, Cr^{2+}	$3d^4$	$^5D_0$	2	0	4.90	4.9
Fe^{3+}, Mn^{2+}	$3d^5$	$^6S_{5/2}$	5/2	5.92	5.92	5.9
Fe^{2+}	$3d^6$	$^5D_4$	2	6.70	4.90	5.4
Co^{2+}	$3d^7$	$^4F_{9/2}$	3/2	6.63	3.87	4.8
Ni^{2+}	$3d^8$	$^3F_4$	1	5.59	2.83	3.2
Cu^{2+}	$3d^9$	$^2D_{5/2}$	1/2	3.55	1.73	1.9

Fig. 1.3 *Schematic representation of the TMPc molecular geometry alongside a simplified and general view of the metal 3d^n electronic levels according to ligand field theory (top left corner). The molecule is planar, and the z-axis is perpendicular to the molecular plane (adapted from [26]).*

For β-MnPc, Brumboiu et al. performed detailed investigations of the electronic configuration of the ground state by Density Functional Theory (DFT) calculations and Photoelectron Spectroscopy (PES) measurements for both thin film and gas phase [26]. Mn^{2+} ($3d^5$) shows $[(d_{xy})^1(d_{xz,yz})^3(d_z^2)^1]$ as the electronic configuration for the thin film, while in the gas phase it exhibits a mixed electronic configuration with $[(d_{xy})^1(d_{xz,yz})^3(d_z^2)^1]$ and $[(d_{xy})^2(d_{xz,yz})^2(d_z^2)^1]$, as shown in Fig. 1.4. As the result, Mn^{2+} in β-MnPc is in the intermediate spin state S = 3/2 instead of usual high spin state S = 5/2 as for example in MnO [27]. They also demonstrated that the ground state of different kind of samples was determined by many factors such as temperature, preparation method, or intermolecular interactions, which opens up the possibility for manipulation of the electronic configuration for MnPc.

Fig. 1.4 *Two variations of the electron ground state of Mn^{2+} in β-MnPc, both with S =3/2 [26].*

For NiPc, Ni^{2+} ($3d^8$) shows spin S = 0 state instead of usual spin state of S = 1 as for example observed for Ni^{2+} in NiO [28]. This also can be explained by the 3d levels split due to the D_{4h} symmetry environment, as shown in Fig.1.5. If Ni^{2+} is in the S = 0 spin state, then NiPc should be a diamagnetic material as demonstrated later in this dissertation.
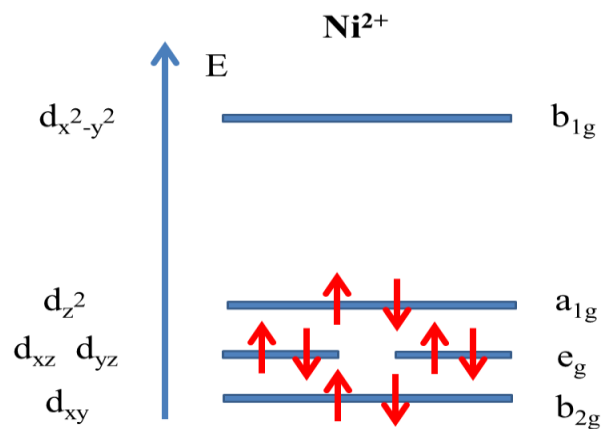
Fig. 1.5 *Electron occupation of 3d levels for the ground state of Ni^{2+} in NiPc [21].*

For β-CoPc, Co^{2+} ($3d^7$) has been shown to be in spin S = 1/2 state rather than the usual high spin

state S = 3/2 as for example in CoO [29]. Fig. 1.6 shows the electron occupation of 3d levels for the

ground state of Co^{2+} in β-CoPc. The difference between the situation of transition metals in TMPc

systems and those in the oxides such MnO, CoO and NiO[27-29] is that the crystal field in the latter

systems has the cubic symmetry compared to the planar symmetry is the TMPc systems as evident in Fig.

1.3. In both α-CuPc and β-CuPc, Cu^{2+} is in the spin S =1/2 state since there are nine electrons in the 3d

shell and one of these electrons has to fill out the $d_{x^2-y^2}$ level, as shown in Fig. 1.7.
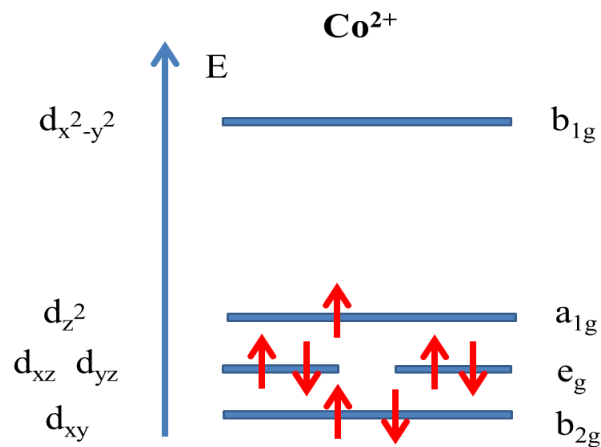
Fig. 1.6 *Electron occupation of 3d levels for the ground state of Co^{2+} in β-CoPc [21].*
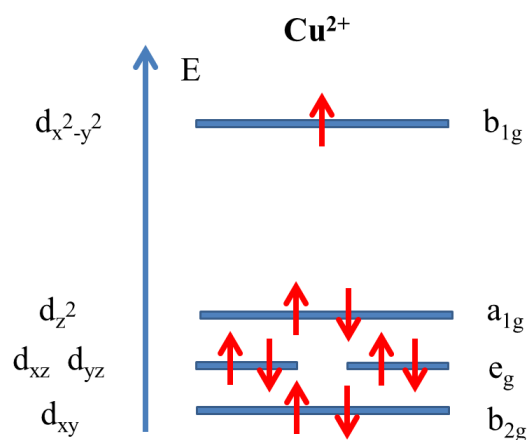
Fig. 1.7 *Electron occupation of 3d levels for the ground state of Cu^{2+} in α-CuPc and β-CuPc [21].*
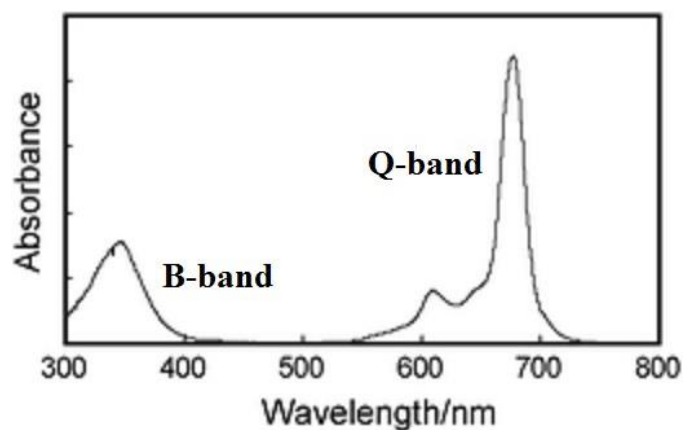
Fig. 1.8 *Optical absorption spectrum of β-CuPc (adapted from [29]).*

1.5 Optical and Electrical Properties of TMPc

The optical absorption spectrum of TMPc makes them excellent materials for pigments. For TMPc, there are two strong absorption bands denoted as Q-band and B-band, respectively (Fig. 1.8) [30]. Q-band is a strong absorption band in the visible region between 670 nm and 690 nm due to a π-π* transition from the highest occupied molecular orbital (HOMO) to the lowest unoccupied molecular

orbital (LUMO), and this is responsible for the characteristic intense blue (or blue-green) color of the TMPc compound. B-band is a strong absorption band in the ultra-violet (UV) region between 320 nm and 370 nm. Also, TMPcs show remarkable nonlinear optical properties such as the intensity-dependent refractive index and the greater absorption coefficient of the excited state than ground state, which lead to potential applications in nonlinear optical devices [31-33].

Table 1.3 *Electrical conductivity of TMPc thin films at room temperature.*

	σ (S/m)	Reference
CuPc	1.00×10^{-4}	[34]
MnPc	1.01×10^{-4}	[35]
CoPc	9.17×10^{-4}	[36]
FePc	4.54×10^{-4}	[37]
NiPc	2.75×10^{-4}	[38]

Semiconducting behavior has been observed in TMPc materials (Table 1.3). As a result, their electrical properties of TMPc are becoming a fast-growing research area in order to make organic nano-electronic devices. Vacuum thermal evaporation, organic molecular beam epitaxy (OMBE), Langmuir-Blogett (LB) method, and spin-coating are the main methods to fabricate TMPc thin films [39]. High quality of thin films, good conductivity, and high thermal stability are the key advantages of TMPc

offered to the organic nano-electronics community. One of the most famous examples is the p-type semiconductor CuPc for which carrier mobility reaches up to 10^{-2} cm^2/Vs. So CuPc has been widely used as the hole transport layer in OLED and OSC [40, 41]. TMPc also have been of considerable interest for potential applications in transistors, gas sensors, and memory devices [42].

1.6 Magnetic properties of TMPc systems

As discussed in section 1.2, TMPc are potential 1D material magnetically because the direct and/or superexchange interaction between the nearest neighboring TM atoms along the monoclinic b-axis. In 1960s, Lever performed magnetization vs. temperature measurements for several TMPc, fit the experimental data to Curie-Weiss law getting some information on exchange coupling [43]. However these measurements were quite limited in that the temperature range covered was only from 100 K to about 325 K. The main conclusions of the paper were that TMPc may have ferromagnetic (FM) or antiferromagnetic coupling (AFM) between the TM ions with very different exchange constants (J_{ex}/k_B) although they share very similar crystal structure. Since then, a number of papers have been published on magnetic properties of TMPc in the following decades. The nature of magnetism in CuPc [9] and β-CoPc [22, 23] have been reported to be Heisenberg linear chain antiferromagnets (HLCA) with spin S = 1/2 but without 3-dimensional (3D) long range order following the predictions of the Bonner-Fisher (BF) model [44]. However, the peak in the magnetization vs. temperature predicted by the BF model was not observed due to the limited temperature range of measurements. On the other hand, β-MnPc has been reported to be a canted ferromagnet below $T_C \approx 8.6$ K. [14, 45-47]. However, the recent result of the lack of a λ-type anomaly in the specific heat vs. temperature data near the quoted T_C has questioned the

presence of long-range 3D magnetic ordering in this system [19, 48]. NiPc has been reported to be a diamagnetic material but without detailed experimental data [43]. Overall, the reported results for TMPc have been primarily based on DC magnetization measurement in a limited temperature range.

1.7 Objectives of this Research and Outline of the Procedures employed

In order to better understand the nature of magnetism in the TMPc systems, more detailed magnetic measurements covering the wider temperature range of 0.4 K to 350 K and in high magnetic fields up to 90 kOe were undertaken. The objective of these investigations was the accurate determination of the nature of magnetism and exchange constants in the TMPc systems with TM = VO, Mn, Co, Ni and Cu. These investigations include not only the temperature and magnetic field dependence of DC magnetization but also those of the AC magnetic susceptibilities χ' and χ'' in the frequency range of 0.1 Hz to 10 kHz. To achieve these objectives, the use of not only the in-house Physical Properties Measurements System (PPMS) was employed but also the facilities available at the National High Magnetic Field Laboratory (NHFML) at Florida State University in Tallahassee, FL and those available at the High Magnetic Field Laboratory, Chinese Academy of Sciences (CHMFL) in China were utilized. The majority of the magnetic measurements covering the temperature from 2 K to 350 K and magnetic field up to 90 kOe were carried out at West Virginia University using the PPMS manufactured by Quantum Design Inc. Additional magnetic measurements for β-CoPc at the lower temperatures of 0.4 K to 20 K were performed using a SCM2 magnet system at the National High Magnetic Field Laboratory (NHMFL) in Florida. For VOPc, a Magnetic Property Measurement System (MPMS) manufactured by Quantum Design Inc. and available at the High Magnetic Field Laboratory, Chinese Academy of Sciences in China

was accessed to acquire data in the low temperature range of 0.5 K to 2 K.

For interpretation of the data in α-CuPc, β-CuPc and β-CoPc, magnetization vs. temperature data were fitted to the BF model offering more accurate results of the exchange constant J_{ex}/k_B. For β-MnPc, both DC and AC magnetization data, and specific heat data lead to the conclusion that the 3D long-range magnetic ordering is absent in this material contrary to the conclusions reached in all previous investigations on this system. For β-NiPc, temperature dependence of magnetization and isothermal data at various temperatures confirmed it to be a diamagnetic material. For VOPc, temperature dependence of magnetization and isothermal data at various temperatures from 0.5 K to 300 K shows the very weak antiferromagnetic exchange coupling ($\theta = -0.1$ K) between VO^{2+} ions which implies the near-perfect paramagnetism in VOPc. Details of these new results, analysis and their discussion are presented in the following chapters.

1.8 Organization of the Dissertation

Chapter 2 outlines the theory of magnetism relevant to TMPc systems including Brillouin function, Curie-Weiss law, effects of crystal field, spin-orbit interaction, Heisenberg exchange interaction, Bonner-Fisher (BF) model, and Ising chain model. In Chapter 3, brief descriptions of the experimental techniques and procedures employed in these investigations are given. In Chapter 4, experimental results and their analysis on the temperature and magnetic field dependence of the magnetization in powder samples of α- and β-CuPc followed by the discussion of the electronic state of Cu and the exchange interactions are presented. Chapter 5 deals with similar data and analysis for the powder sample of β-CoPc. In this sample, a peak in the χ vs. T data predicted by the BF model was observed for the first

time and the exchange constant J_{ex}/k_B was accurately determined by fitting χ vs. T data to the BF model over the wide temperature range of 0.4 K to 300 K. In Chapter 6, magnetic properties of the powder sample of VOPc covering the temperature range of 0.5 K to 300K and in magnetic fields up to 90 kOe are presented, analyzed and discussed. The magnetization data fits well with the Curie-Weiss law with very small $\theta = - 0.1$ K which implies the near-perfect paramagnetic nature of VOPc. In Chapter 7, temperature and magnetic field dependence of the magnetization of powder sample of β-NiPc is presented confirming the overall diamagnetism in this material. In Chapter 8, detailed measurements of both the temperature and magnetic field dependence of the DC and AC magnetic susceptibilities of powder sample of β-MnPc are presented followed by thorough discussion and analysis. From this analysis, the exchange constant J_{ex}/k_B and the single ion anisotropy are determined. In addition, a Cole-Cole analysis is carried out by plotting the ac susceptibilities χ'' vs. χ' at different temperatures to determine distribution in the magnetic relaxation rate and it is concluded that this system lacks 3-dimensional long range magnetic ordering contrary to conclusions reached in previous publications. In Chapter 9, a summary of the major results resulting from this work is presented followed by suggestions for future studies. A list of publications and presentations by the author are also included in this chapter. Finally, in appendix A, a copy of the proposal submitted to the National High Magnetic Field Laboratory for low temperature magnetic measurements of β-CoPc is presented and in appendix B, typical computer sequences used for measuring the magnetic properties using the PPMS are listed.

References

[1] V.A. Dediu, L.E. Hueso, L. Bergenti and C. Taliani, Nat. Mater. **8**, 707 (2009).

[2] S.R. Forrest, Nat. **428**, 911 (2004).

[3] M. Berggren and A. Richter-Dahlfors, Adv. Mater. **19**, 3201 (2007).

[4] R.P. Linstead and A.R. Lowe, J. Chem. Soc. 1022 (1934).

[5] R.P. Linstead and C.E. Dent, J. Chem. Soc. 1027 (1934).

[6] J.M. Robertson, J. Chem. Soc. 615 (1935).

[7] J.M. Robertson, J. Chem. Soc. 1195 (1935).

[8] S.M. Tadayyon, H.M. Grandin, K. Griffiths, P.R. Norton, H. Azizi and Z.D. Popovic, Org. Electron. **5**, 157 (2004).

[9]. H. Wang, S. Mauthoor, S. Din, J. A. Gardener, R. Chang, M. Warner et al. ACS Nano. **4**, 3921, (2010).

[10]. M. Warner, S. Din, I. S. Tupitsyn, G. W. Morley, A. M. Stoneham, J. A. Gardener et al. Nature. **503**, 505 (2013).

[11] P. Ballirano, R. Caminiti, C. Ercolani, A. Maras and M.A. Orru, J. Am. Chem. Soc. **120**, 12798 (1998).

[12] J.M. Assour, J. Phys. Chem. **69** (7), 2295 (1965).

[13] C. Ercolani, C. Neri and P. Porta, Inorg. Chim. Acta. **1**, 415 (1967).

[14] C.G. Barraclough, R.L. Martin, S. Mitra and R.C. Sherwood, J. Chem. Phys. **53**, 1638 (1970).

[15] P. W. Anderson, Phys. Rev. **115**, 2 (1959).

[16] In the space groups C2/c and P2$_1$/c of the monoclinic structure in Table 1.1, the first letter represents the Bravais lattice: P for primitive and C for centered. Next, the number 2 represents the presence of a two-fold (180°) rotation axis which for monoclinic systems is the b-axis and 2$_1$ represents a two-fold rotation axis followed by a translation of ½ of the lattice vector along the rotation axis. Finally /c represents a c-glide plane perpendicular to the b-axis.

[17] Z. Wang, K.L. Pisane and M.S. Seehra, IEEE. Trans. Mag. **51**, 2700104 (2015).

[18] C. Kittel, Introduction to Solid State Physics, 8th edition. Wiley, 2004.

[19] Y. Taguchi, T. Miyake, S. Margadonna, K. Kato and Y. Iwasa, J. Am. Chem. Soc. **128**, 3313 (2006).

[20] T. Kataoka, Y. Sakamoto, Y. Yamazaki, V.R. Singh, A. Fujimori, Y. Takeda, T. Ohkochi, S.-I. Fujimori, T. Okane, Y. Saitoh, H. Yamagami and A. Tanaka, Solid State Communs. **152**, 806 (2012).

[21] A. Mugarza, R. Robles, C. Krull, R. Korytar, N. Lorente and P. Gambardella, Phys. Rev. B. **85**, 155437 (2012).

[22] M. Serri, W.Wu, L.R. Fleet, N.M. Harrison, C.F. Hirjibehedin, C.W.M. Kay, A.J. Fisher, G. Aeppli and S. Heutz, Nature Commun. **5**, 3079 (2014).

[23] W. Wu, N.M. Harrison and A.J. Fisher, Phys. Rev. B. **88**, 024436 (2013).

[24] J.S. Griffith and L.E. Orgel, Rev. Chem. Soc. **11**, 381 (1957).

[25] 3d electron orbital: http://socratic.org/

[26] I.E. Brumboiu, R. Totani, M.D. Simone, M. Coreno, C. Grazioli, L. Luca, H.C. Herper, B. Sanyal, O. Eriksson, C. Puglia and B. Brena, J. Phys. Chem. A. **118**, 927 (2014).

[27] M. S. Jagadeesh and M. S. Seehra, Phys. Rev. B. **21**, 2897 (1980).

[28] G. Srinivasan and M. S. Seehra, Phys. Rev. B. **29**, 6295 (1984).

[29] P. Silinsky and M. S. Seehra, Phys. Rev. B. **24**, 419 (1981).

[30] H. Yaku, T. Fujimoto, T. Murashima, D. Miyoshi and N. Sugimoto, Chem. Commu. **48**, 6203 (2012).

[31] J.S. Shirk, J.R. Lindle, F.J. Bartoli, C.A. Hoffman, Z.H. Kafafi and A.W. Snow, Appl. Phys. Lett. **55**, 1287 (1989).

[32] G. de la Torre, P. Vazquez, F. Agullo-Lopez and T. Torres, J. Mater. Chem. **8**, 1671 (1998).

[33] G. de la Torre, P. Vazquez, F. Agullo-Lopez and T. Torres, Chem. Rev. **104**, 3723 (2004).

[34] A. Sussman, J. Appl. Phys. **38**, 2748 (1967).

[35] K.R. Rajesh and C.S. Menon, Eur. Phys. J. B. **47**, 171 (2005).

[36] S. Ambily and C.S. Menon, Indian J. Pure Appl. Phys. **37**, 566 (1999).

[37] K.P. Khrishnakumar and C.S. Menon, Mater. Lett. **48**, 64 (2001).

[38] K.N. Narayanan Unni and C.S. Menon, Mater. Lett. **45**, 326 (2000).

[39] M. Ling and Z. Bao, Chem. Mater. **16**, 4824 (2004).

[40] C.W. Tang, Appl. Phys. Lett. **48**, 183 (1986).

[41] S.M. Tadayyon, H.M. Grandin, K. Griffiths, P.R. Norton, H. Aziz and Z.D. Popovic, Org. Electron. **5**, 157 (2004).

[42] N.B. McKeown, Phthalocyanine Materials: Synthesis, Structure and Function. Cambridge, U.K.: Cambridge Univ. Press, 1998.

[43] A.B.P. Lever, J. Chem. Soc. 1821 (1965).

[44] J.C. Bonner and M.E. Fisher, Phys. Rev. **135**, A640 (1964).

[45] C.G. Barraclough, A.K. Gregson and S. Mitra, J. Chem. Phys. **60**, 962 (1974).

[46] H. Miyoshi, H. Ohya-Nishiguchi and Y. Deguchi, Bull. Chem. Soc. Jpn. **46**, 2724 (1974).

[47] H. Miyoshi, Bull. Chem. Soc. Jpn. **47**, 561 (1974).

[48] Y. Taguchi, T. Miyake, S. Margadonna, K. Kato, K. Prassides and Y. Iwasa, J. Magn. Magn. Mater. **310**, 1229 (2007).

CHAPTER 2.

Magnetism: Background and Theoretical Considerations

2.1 Background

The history of magnetism dates back to about 600 BC when ancient Greeks first used a mineral called lodestone which is now known to contain ferrimagnetic magnetite (Fe_3O_4). The lodestone was called a magnet because of its ability to attract other pieces of the same material and iron. However, the nature of magnetism was first truly studied by Englishman William Gilbert (1540-1603) who investigated the phenomenon of magnetism systematically using scientific methods and published his classic book *On the Magnet* in 1600. Gilbert also discovered that the earth itself is a magnet and German Carl Friedrich Gauss (1777-1855) carried out the early theoretical investigations into the nature of the earth's magnetism. Frenchman Charles Coulomb (1736-1806) initiated the quantitative studies of magnetic phenomena in 18th century, established the inverse square law of the magnetic force. The link between electricity and magnetism was first suggested by Danish physicist Hans Christian Oersted (1777-1851), later was proved by Frenchman Andre Marie Ampere (1775-1836) and Englishman Michael Faraday (1791-1869), who conducted experiments.

The modern understanding of magnetic phenomena was initiated by Pierre Curie (1859-1906) and his wife Madame Marie Curie (1867-1934), Paul Langevin (1872-1946), and Pierre Weiss (1865-1940). In 1895, Pierre Curie first reported the measurements of the magnetization of a large number of substances over an extended range of temperature and proposed the Curie law. Later (in 1905)

Paul Langevin proposed theories on both diamagnetism and paramagnetism without taking into account of interaction between the individual carriers of magnetic moment (atoms or molecules) [1]. In 1907 Weiss pointed out that the paramagnetism can be understood by postulating the elementary moments do interact with one another through so called 'molecular field' and his theory lead to the Curie-Weiss law [2]. With the powerful tool of quantum mechanics, especially the spin magnetic moment, the modern theory on magnetism was finally established in the first half of 20th century. The material given below in Sections 2.2, 2.3, 2.4 and 2.5 using the quantum theory of magnetism is based on the books by Moorish [3] and Pake [4]. These concepts and equations are used in subsequent chapters for the interpretation of the experimental data.

2.2 Magnetic Moment, Brillouin Function, and Curie-Weiss Law

In quantum theory, the magnetic moment of an atom or ion in free space is given by [3]:

$$\vec{\mu} = -g\mu_B\vec{J} \qquad (2.1)$$

where the total angular momentum $\vec{J}$ is the vector sum of orbital angular momentum $\vec{L}$ and spin angular momentum $\vec{S}$. $\mu_B = eh/4\pi mc = 9.274 \times 10^{-21}$ emu is called the Bohr Magneton and the negative sign of the electron charge is taken into account in writing Eq. (2.1). In Eq. (2.1), g is called the Lande g-factor with g = 1 and g = 2 are for the orbital and spin angular momentum respectively. For a free atom, the Lande g-factor is given by:

$$g = 1 + \frac{J(J + 1) - S(S + 1) - L(L + 1)}{2J(J + 1)} \qquad (2.2)$$

In an applied magnetic field, the Hamiltonian and potential energy of a magnetic moment are given by

$$\varkappa = -\vec{\mu} \bullet \vec{H} = g\mu_B \vec{J} \bullet \vec{H} = g\mu_B H J_z \qquad (2.3)$$

$$E = g\mu_B H m_J, \quad m_J = -J, -J + 1, \dots, J - 1, J \qquad (2.4)$$

where m_J is called the azimuthal quantum number. For example: for $J = 1/2$, $m_J = 1/2$, -1/2 giving two levels with energy $E = -g\mu_B H/2$ and $g\mu_B H/2$. For $J = 1$, $m_J = 1$, 0, -1 leading to three levels with energy $E = g\mu_B H$, 0, $-g\mu_B H$. Once the energy levels are known, the magnetization M defined as the magnetic moment per unit volume with N being the number of atoms or molecules per unit volume, can be determined from the equation [3]:

$$M = -N \frac{\sum_n \frac{\partial E_n}{\partial H} e^{-\frac{E_n}{k_B T}}}{\sum_n e^{-\frac{E_n}{k_B T}}} \qquad (2.5)$$

Using $E = g\mu_B H m_J$ from Eq. (2.4), it can be shown that Eq. (2.5) reduces to

$$M = Ng\mu_B J B_J(y) = M_S B_J(y) \qquad (2.6)$$

where $y = g\mu_B H J/(k_B T)$, $M_S = Ng\mu_B J$ is the saturation magnetization, and $B_J(y)$ is given by

$$B_J(y) = \frac{2J+1}{2J}\coth\left(\frac{2J+1}{2J}y\right) - \frac{1}{2J}\coth(\frac{y}{2J}) \qquad (2.7)$$

$B_J(y)$ is called the Brillouin function (shown as Fig. 2.1) and was first obtained in 1927. The importance

of Eq.(2.5) is that it allows calculation of M for any system once the energy level of the system are known

under the action of an applied magnetic field H.

For the special case of J = 1/2, m_J = 1/2, -1/2, the energy levels are E_n = gμ_BH/2 and gμ_BH/2.

Substituting these in Eq. (2.5) with $x = \frac{g\mu_B H}{2k_B T}$ and $M_S = \frac{1}{2}Ng\mu_B$ yields

$$M = \frac{1}{2}Ng\mu_B \frac{e^x - e^{-x}}{e^x + e^{-x}}$$

$$= M_S\tanh(\frac{g\mu_B H}{2k_B T}) \qquad (2.8)$$
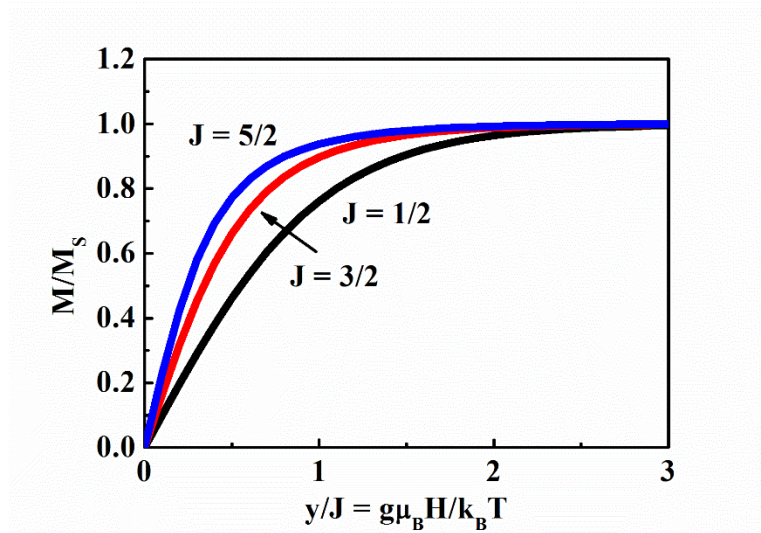
Fig. 2.1 *Plot of Brillouin function with J = 1/2, 3/2, and 5/2.*

For y << 1 (low field and high temperature case), it can be shown that Eq. (2.6) yields

$$M = \frac{Ng^2\mu_B^2 J(J+1)}{3k_B T} H \qquad (2.9)$$

From Eq. (2.9), the magnetic susceptibility is given by

$$\chi = \frac{\partial M}{\partial H} = \frac{N\mu^2}{3k_B T} = \frac{C}{T} \qquad (2.10)$$

where $\mu = g\mu_B\sqrt{J(J+1)}$ is called the effective magnetic moment and $C = N\mu^2/(3k_B)$ is known as the Curie constant. Eq. (2.10) is called Curie law (1/T variation of magnetic susceptibility). For the classical case when $J = \infty$, the Brillouin function reduces to the Langevin function L(y) (classical theory) given by

$$L(y) = \coth(y) - \frac{1}{y} \qquad (2.11)$$

So the magnetization becomes

$$M = M_S L(y) = M_S[\coth(y) - \frac{1}{y}] \qquad (2.12)$$

If $y = g\mu_B HJ/(k_B T) \ll 1$ (low field and high temperature case), the Langevin function can be expressed as a series, it is

$$L(y) = \frac{y}{3} - \frac{y^3}{45} + \frac{2y^5}{945} - \cdots \approx \frac{y}{3} \qquad (2.13)$$

L(y) as a function of y is plotted in Fig. 2.2. The solid line is the Langevin function whereas the dash line represents the Langevin function for $y \ll 1$.
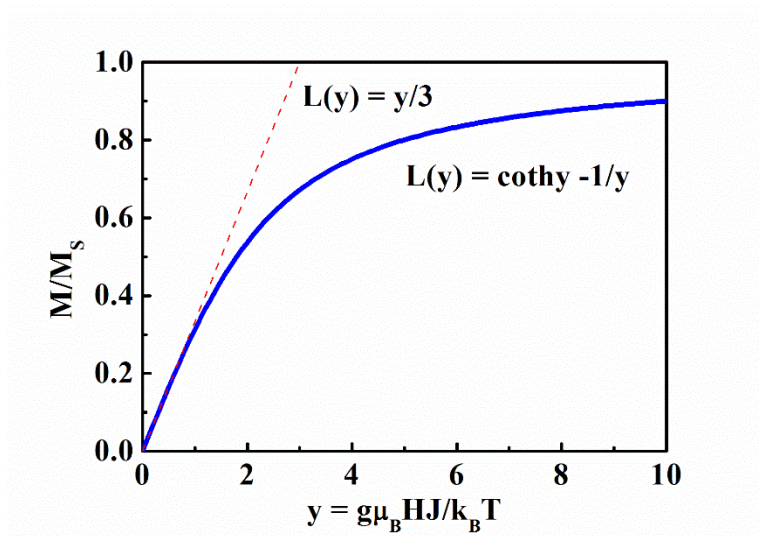
Fig. 2.2 *Variation of normalized magnetization with normalized magnetic field, Eq. (2.12)*

The above derivation of Curie law assumes no interaction between magnetic moments. In 1907, Weiss proposed the presence of an effective field H_M due to interaction between magnetic moments proportional to the magnetization given by:

$$H_M = N_W M \tag{2.14}$$

where N_W is the molecular field constant. Then the total field is

$$H_T = H + H_M \tag{2.15}$$

For Brillouin function $M = N g \mu_B J B_J(y)$ with $y = g \mu_B J H / k_B T$, H is replaced by $H_T = H + H_M$

$$y = \frac{g\mu_B J}{k_B T} H_T = \frac{g\mu_B J}{k_B T} (H + H_M) = \frac{g\mu_B J}{k_B T} (H + N_W M) \tag{2.16}$$

For $y \ll 1$, $B_J(y) = \frac{(J+1)}{3J} y$

$$M = Ng\mu_B J \frac{(J+1)}{3J} y = \frac{Ng\mu_B(J+1)}{3} \cdot \frac{g\mu_B J(H + N_W M)}{k_B T} = \frac{Ng^2\mu_B^2 J(J+1)}{3k_B T}(H + N_W M) \tag{2.17}$$

with $C = N\mu^2/(3k_B) = Ng^2\mu_B^2 J(J+1)/3k_B$, then

$$M = \frac{C}{T}(H + N_W M)$$

$$M = \frac{CH}{T - CN_W} \tag{2.18}$$

The magnetic susceptibility is then given by

$$\chi = \frac{\partial M}{\partial H} = \frac{C}{T - CN_W} = \frac{C}{T - \theta} \tag{2.19}$$

where the Weiss constant $\theta = C \cdot N_W = T_C$ and the Curie constant $C = N\mu^2/3k_B$. Eq. (2.19) is the

Curie-Weiss (CW) law. If $\theta > 0$, the material is a ferromagnet and the ordering temperature $T_C = \theta$ is

called the Curie temperature. If $\theta < 0$, the material is an antiferromagnet, the ordering temperature $T_N = \theta$

is called the Neel temperature.

2.3 Effect of Crystal Field

In a solid, the energy level of an electron on a site is affected by the crystal field of the

neighboring ions [4]. Consider a 3d^1 electron (such as in VOPc discussed later in this dissertation) in a

cubic field of six negative ions at a distance of a_0. The wave functions of the electron must obey the symmetry of the crystalline field. These orbitals of the electron, constructed from spherical harmonics of $l = 2$, are shown in Chapter 1 (Fig 1.2). It is straightforward to show that for these orbitals, the expectation value of $<Lz>$ is zero i.e. the orbital momentum is quenched. The five-fold degeneracy of $l = 2$ state is lifted by the crystal field due to Stark splitting, leading to a triplet (xy, yz, zx orbital) and a doublet (z^2, x^2-y^2 orbital) as shown in Fig 2.3. If the crystal filed is tetragonal, then there is a further splitting of the energy levels as shown in Fig 2.3. Depending on the strength of the crystal field, the magnitudes of the parameters $\Delta \approx 10^4$ cm^{-1} and $\delta \approx 10^2$ to 10^3 cm^{-1}. So at low temperatures, only the lowest energy levels will be occupied. Optical absorption measurements are usually used to determine the magnitudes of Δ and δ. The spin of the electron doubles the degeneracy of each level with + (-) designating the up (down) spin. In an applied magnetic field, this degeneracy is lifted due to the Zeeman splitting.
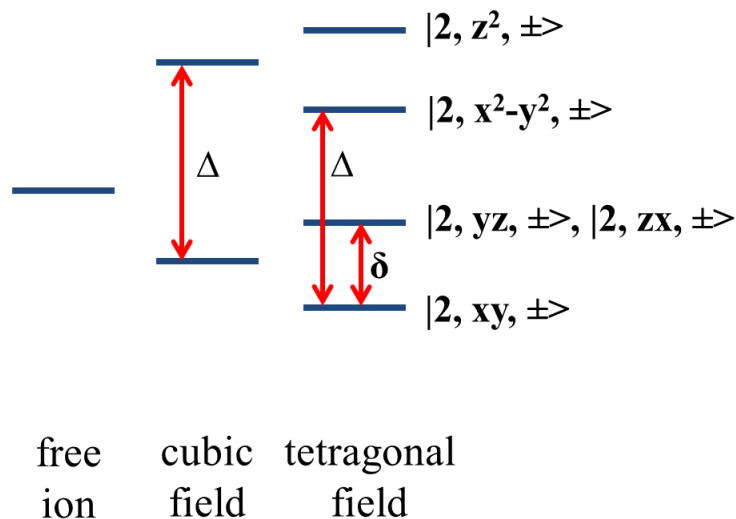
Fig. 2.3 *Splitting of the 3d^l electron energy level due to cubic field (Δ) and tetragonal field (δ).*

2.4 Effect of Spin-Orbit Interaction

As noted earlier, the expectation values of the angular momentum $<L_z>$ can be shown to be zero for each of the Stark-split levels of Fig 2.3. The spin-orbit interaction $\lambda \vec{L} \cdot \vec{S}$ partially restores some of this orbit contribution to the magnetic moment by mixing some of the excited states into the ground state. By writing $\lambda \vec{L} \cdot \vec{S}$ in terms of raising and lowering operators:

$$H' = \lambda \vec{L} \cdot \vec{S} = \lambda[L_z S_z + \frac{1}{2}(L_+ S_- + L_- S_+)] \qquad (2.20)$$

Here λ is the spin-orbit coupling constant, $L_\pm = L_x \pm iL_y$, and $S_\pm = S_x \pm iS_y$. Now consider the effect of Eq. (2.20) on the states shown in Fig. 2.3 using the first order perturbation theory according to which

$$H = H_0 + H' \text{ (perturbation)} \qquad (2.21)$$

$$\text{with } H_0|n^{(0)}> = E_n^0|n^{(0)}> \qquad (2.22)$$

$$\text{and } H|n> = E_n|n> \qquad (2.23)$$

$$E_n = E_n^{(0)} + <n^{(0)}|H'|n^{(0)}> + \sum_{m \neq n} \frac{<n^{(0)}|H'|m^{(0)}><m^{(0)}|H'|n^{(0)}>}{E_n^{(0)} - E_m^{(0)}} \qquad (2.24)$$

$$\text{and } |n> = |n^{(0)}> + \sum_{m \neq n} \frac{<m^{(0)}|H'|n^{(0)}>}{E_n^{(0)} - E_m^{(0)}}|m^{(0)}> \qquad (2.25)$$

The total effect of the $\lambda \vec{L} \cdot \vec{S}$ term on the ground state $|2, xy, \pm>$ is to modify this state to

$$|\pm>= |2, xy, \pm> \pm \frac{i\lambda}{\Delta} |2, x^2 - y^2, \pm> \mp \frac{\lambda}{2\delta} |2, yz, \mp> + \frac{i\lambda}{2\delta} |2, zx, \mp> \qquad (2.26)$$

For the applied field along z direction, the Zeeman energy is given by

$$\varkappa = -\vec{\mu} \bullet \vec{H} = \frac{\mu_B}{\hbar} (L_z + 2S_z)H_0 \qquad (2.27)$$

For the state given by Eq. (2.26), the expectation values of magnetic moment is given by–

$$\mu = \frac{\mu_B}{\hbar} (L_z + 2S_z) \qquad (2.28)$$

$$< +|L_z + 2S_z|+> = \frac{\hbar}{2}(2 - \frac{8\lambda}{\Delta}) \qquad (2.29)$$

$$< -|L_z + 2S_z|-> = \frac{\hbar}{2}(-2 + \frac{8\lambda}{\Delta}) \qquad (2.30)$$

Substituting these values in Eq. (2.27) yields

$$< +|E|+> = \frac{1}{2}(2 - \frac{8\lambda}{\Delta})H_0\mu_B \qquad (2.31)$$

$$< -|E|-> = \frac{1}{2}(-2 + \frac{8\lambda}{\Delta})H_0\mu_B \qquad (2.32)$$

$$\Delta E = < +|E|+> - < -|E|->= \left(2 - \frac{8\lambda}{\Delta}\right)\mu_B H_0 = g_z\mu_B H_0 \qquad (2.33)$$

$$g_z = g_e - \frac{8\lambda}{\Delta} \qquad (2.34)$$

with $g_e = 2.0023 \approx 2$ for the free electron. For the field applied along x direction (also equivalent to y direction for tetragonal symmetry), a similar calculation yields

$$\varkappa = -\vec{\mu} \cdot \vec{H} = \frac{\mu_B}{\hbar} (L_x + 2S_x)H_0 \tag{2.35}$$

$$g_x = g_y = g_e - 2\frac{\lambda}{\delta} \tag{2.36}$$

Here λ is positive (negative) if the shell is less (more) than half-filled. So the g-shift $(g - g_e)$ is negative (positive) for ions with shell less (more) than half full with electrons. In the following chapters, examples are given showing negative g-shift for VO^{2+} in VOPc and positive g-shifts for Co^{2+} in CoPc, Mn^{2+} in MnPc and Cu^{2+} in CuPc.

2.5 The Heisenberg Exchange Interaction

Consider two electrons, a and b, located in the neighboring sites 1 and 2, such that $\psi_a(1)$ and $\psi_a(2)$ are the wave functions of electron a at site 1 and 2 and $\psi_b(1)$ and $\psi_b(2)$ are the wave functions of electron b at site 1 and 2 respectively [3]. In addition to the above spatial part of wavefunction, we also need to consider the spin part of wavefunction of the electrons. According to Pauli's Exclusion Principle, the total wavefunction must be antisymmetric with respect to interchange of electrons at site 1 and 2. The total wavefunction is:

$$\psi_{total} = \psi_{space} \cdot \psi_{spin} \tag{2.37}$$

The spin part of the wavefunction is shown in the following table.

Table 2.1 *Spin part of the wavefunction.*

Wave function	S	S_Z	
$\frac{1}{\sqrt{2}}(\lvert \uparrow\downarrow > - \lvert \downarrow\uparrow >)$	0	0	Singlet: antisymmetric
$\lvert \uparrow\uparrow >$	1	1	
$\frac{1}{\sqrt{2}}(\lvert \uparrow\downarrow > + \lvert \downarrow\uparrow >)$	1	0	Triplet: symmetric
$\lvert \downarrow\downarrow >$	1	-1	

The spatial part of the wavefunction:

$$\psi_S = \frac{1}{\sqrt{2}}[\psi_a(1)\psi_b(2) + \psi_b(1)\psi_a(2)] \tag{2.38}$$

$$\psi_A = \frac{1}{\sqrt{2}}[\psi_a(1)\psi_b(2) - \psi_b(1)\psi_a(2)] \tag{2.39}$$

where ψ_S and ψ_A are symmetric and antisymmetric wave-functions respectively. The electrostatic

Coulomb interaction energy for the two electron system is then given by

$$V = \frac{1}{2}\int \{\psi_a^*(1)\psi_b^*(2) \pm \psi_a^*(2)\psi_b^*(1)\}\frac{e^2}{r_{12}}\{\psi_a(1)\psi_b(2) \pm \psi_a(2)\psi_b(1)\}d^3r_1 d^3r_2$$

$$= \frac{1}{2}\left\{\int |\psi_a(1)|^2 \frac{e^2}{r_{12}}|\psi_b(2)|^2 d^3r_1 d^3r_2 + \int |\psi_a(2)|^2 \frac{e^2}{r_{12}}|\psi_b(1)|^2 d^3r_1 d^3r_2\right\}$$

$$\pm \frac{1}{2}\{\int \psi_a^*(1)\psi_b^*(2)\frac{e^2}{r_{12}}\psi_a(2)\psi_b(1)d^3r_1 d^3r_2$$

$$\pm \int \psi_a^*(2)\psi_b^*(1)\frac{e^2}{r_{12}}\psi_a(1)\psi_b(2)d^3r_1 d^3r_2\}$$

$$= K \pm J_{ex} \tag{2.40}$$

$$K = \int |\psi_a(1)|^2 \frac{e^2}{r_{12}} |\psi_b(2)|^2 d^3r_1 d^3r_2 \tag{2.41}$$

$$J_{ex} = \int \psi_a^*(1)\psi_b^*(2) \frac{e^2}{r_{12}} \psi_a(2)\psi_b(1) d^3r_1 d^3r_2 \tag{2.42}$$

K and J_{ex} are known as the Coulomb term and Exchange term, respectively. J_{ex} is called exchange energy because the integral involves the exchange of the two electrons between site 1 and 2. The Hamiltonian of the two electrons can then be written as:

$$H_{ab} = K_{ab} - \frac{1}{2} J_{ex}(1 + 4\vec{S_a} \cdot \vec{S_b}) \tag{2.43}$$

$$\text{with } 2 < \vec{S_a} \cdot \vec{S_b} > = S(S+1) - S_a(S_a+1) - S_b(S_b+1) \tag{2.44}$$

For the triplet state total $S = 1$, $S_a = S_b = 1/2$ and so

$$2 < \vec{S_a} \cdot \vec{S_b} > = 2 - \frac{3}{4} - \frac{3}{4} = \frac{1}{2}$$

$$H_{ab} = K_{ab} - \frac{1}{2} J_{ex}(1 + 4\vec{S_a} \cdot \vec{S_b}) = K_{ab} - \frac{1}{2}J_{ex}\left(1 + 2 \cdot \frac{1}{2}\right) = K_{ab} - J_{ex} \tag{2.45}$$

For singlet state total $S = 0$, $S_a = S_b = 1/2$ and so $2 < \vec{S_a} \cdot \vec{S_b} > = 0 - \frac{3}{4} - \frac{3}{4} = -\frac{3}{2}$. This gives

$$H_{ab} = K_{ab} - \frac{1}{2} J_{ex}(1 + 4\vec{S_a} \cdot \vec{S_b}) = K_{ab} - \frac{1}{2}J_{ex}\left(1 + 2 \cdot \frac{-3}{2}\right) = K_{ab} + J_{ex} \tag{2.46}$$

So for $J_{ex} > 0$, the energy of triplet state is lower than the singlet state, corresponding to ferromagnetic state which neighboring spins are in the same direction; for $J_{ex} < 0$, the energy of singlet state is lower than the triplet state, corresponding to antiferromagnetic state with neighboring spins are in opposite direction. Thus, from the above derivation, the Hamiltonian can be written as:

$$H_{ab} = K_{ab} - \frac{1}{2} J_{ex}(1 + 4\vec{S_a} \cdot \vec{S_b}) = K_{ab} - \frac{1}{2} J_{ex} - 2J_{ex}\vec{S_a} \cdot \vec{S_b} \qquad (2.47)$$

The first two terms of the above equation are independent of the spin, whereas the last term depends on the spin. If J_{ex} is negligible except for the nearest neighbors and is the same for all the nearest neighbors, then the spin-dependent Heisenberg exchange term can be written as:

$$H = -2J_{ex} \sum \vec{S_i} \cdot \vec{S_j} \qquad (2.48)$$

2.6 The Bonner-Fisher Model for spin S = 1/2

Bonner and Fisher (BF) [5] considered linear magnetic chains in magnetic H with anisotropic Heisenberg Hamiltonian:

$$\varkappa = -2J_{ex} \sum_{i=1}^{N}(S_i^z S_{i+1}^z) + \gamma(S_i^x S_{i+1}^x + S_i^y S_{i+1}^y) - g\mu_B \sum_{i=1}^{N} H \cdot S_i \qquad (2.49)$$

For $\gamma = 0$ (1), the Hamiltonian reduces to the Ising (Heisenberg) case. They solved this case for the calculations of magnetic susceptibility χ and specific heat C_M for $N = 2$ to 11 spins each with spin $S = 1/2$ for both ferromagnetic ($J_{ex} > 0$) and antiferromagnetic ($J_{ex} < 0$) cases. For the antiferromagnetic case ($J_{ex} <$

0) which applies to the CuPc and CoPc systems in this dissertation, these solution showed that for $\gamma = 1$, the χ vs. T data should go through a maximum at a temperature T_{max} given by

$$T_{max} \approx 1.282 \frac{|J_{ex}|}{k_B}$$ (2.50)

For $\gamma = 0$ (Ising case), a similar maximum is predicted but at a temperature $T_{max} = |J_{ex}|/k_B$ (this will be discussed in the next section). Also the calculated magnitude of χ at T_{max} is different for the two cases so that the difference between the $\gamma = 0$ and $\gamma = 1$ cases can be verified experimentally.

Since the BF solution was valid only for the maximum of N = 11 spins, a solution for N $\rightarrow \infty$ valid for real systems was needed. Feyerherm et al. [6] provided such a solution valid for T > 0.1 $|J_{ex}|/k_B$ and $\gamma = 1$ in terms an empirical rational function for the magnetic susceptibility χ given by

$$\chi = \frac{C}{T}F(x)$$ (2.51)

$$F(x) = \frac{1 + a_1 x + a_2 x^2}{1 + b_1 x + b_2 x^2 + b_3 x^3}$$ (2.52)

Here C is the Curie constant, $x = |J_{ex}|/(k_B T)$ and $a_1 = 0.17032$, $a_2 = 0.93404$, $b_1 = 1.46764$, $b_2 = 0.54784$, $b_3 = 4.28544$. Eq. (2.51) can be rewritten as

$$\frac{\chi|J_{ex}|}{Ck_B} = xF(x)$$ (2.53)

A plot of $(\chi|J_{ex}|)/Ck_B$ vs. $k_B T/|J_{ex}| = 1/x$ is shown in Fig. 2.4. The maxima occurs at $T_{max} = 1.3$ $|J_{ex}|/k_B$ in agreement with the BF calculations; However, Feyerherm et al. showed that for T < 0.5 $|J_{ex}|/k_B$, there is

35

some disagreement with the prediction of the BF model. In a later chapter, the experimental results of

magnetic susceptibility versus temperature in α-CuPc, β-CuPc and β-CoPc are compared with Eq. (2.51)

and Eq. (2.53).
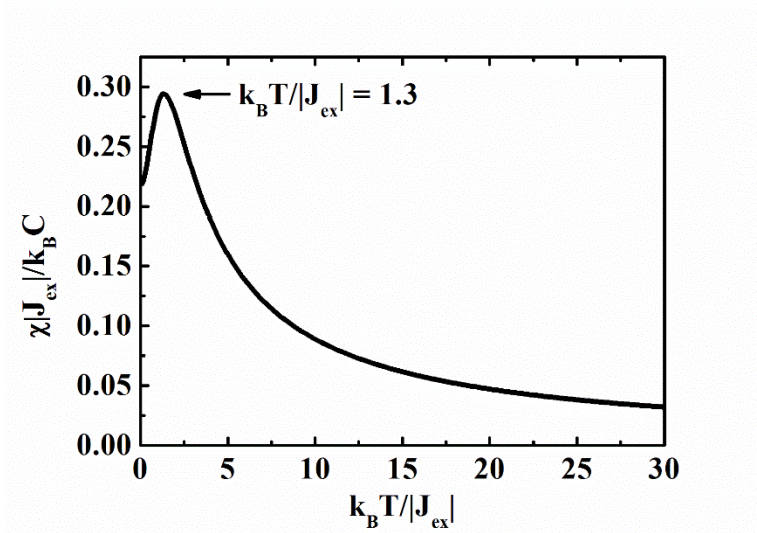
Fig. 2.4 *Plot of the normalized parameters ($\chi|J_{ex}|)/Ck_B$ vs. $k_BT/|J_{ex}|$ = 1/x.*

2.7 The Ising Chain Model for Spin S

For Ising chain, the Hamiltonian is

$$H = -2J_{ex} \sum_{i=1}^{N} S_i^z S_{i+1}^z \qquad (2.54)$$

The parallel susceptibility (when the applied field is along z-axis) is given by C. Coulon et al. [7]

$$\frac{\chi T}{C} = \frac{1 + \Gamma}{1 - \Gamma} \qquad (2.55)$$

36

Here as usual $C = N\mu^2/3k_B$ is the Curie constant and the correlation function $\Gamma = \tanh(2\beta J_{ex}S^2)$ with $\beta = 1/k_BT$ [8]. For low temperature case, the parallel susceptibility is

$$\frac{\chi_{//}T}{C} \approx \exp(4\beta J_{ex}S^2) \qquad (2.56)$$

It is noted that the perpendicular susceptibility of Ising chain has also been calculated and stays constant at low temperature remaining much smaller than the parallel susceptibility [9].For spin $S = 1/2$ antiferromagnetic system ($J_{ex} < 0$), Eq. (2.56) can be written as

$$\frac{\chi|J_{ex}|}{Ck_B} = xe^{-x} \qquad (2.57)$$

where $x = |J_{ex}|/k_BT$. A plot of the normalized parameters $(\chi|J_{ex}|)/Ck_B$ vs. $k_BT/|J_{ex}| = 1/x$ is shown in Fig. 2.5. The maxima occurs at $T_{max} = 1.0\ |J_{ex}|/k_B$ in agreement with the BF calculations.
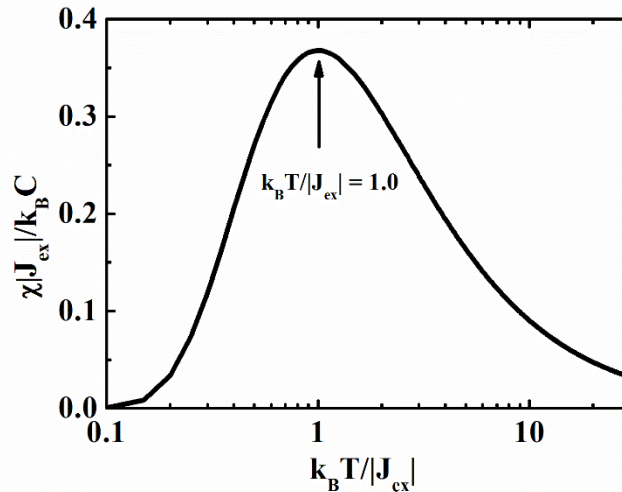
Fig. 2.5 *Plot of $(\chi|J_{ex}|)/Ck_B$ vs. $k_BT/|J_{ex}| = 1/x$ for Ising chain with spin $S = 1/2$ antiferromagnetic coupled system.*

The theoretical expression for the magnetic field dependence of the magnetization of an Ising chain magnet has been given as [10, 11]:

$$\frac{M}{M_S} = \frac{\sinh(\mu_B \beta H)}{\sqrt{\sinh^2(\mu_B \beta H) + \exp(-8\beta J_{ex} S^2)}} \qquad (2.58)$$

In Eq. (2.58), M_S is the saturation magnetization and $\beta = 1/k_B T$. In the following chapters, the theoretical expressions given above for the Ising and Heisenberg chain models will be tested against the experimental results of the temperature and magnetic field dependence of the magnetization measured in powder samples of TMPc (TM = VO, Mn, Co and Cu). These new experimental results and their theoretical interpretations based on the above models are the new contributions of this dissertation.

References

[1] P. Langevin, Ann. Chemie et Physique. **5**, 70 (1905).

[2] P. Weiss, J. de Physique. **6**, 66 (1907).

[3]. A. H. Morrish. The Physical Principals of Magnetism (IEEE Press, New York. 2001).

[4] G.E. Pake. Paramagnetic Resonance (W.A. Benjamin. Inc. New York, 1962).

[5] J.C. Bonner and M.E. Fisher, Phys. Rev. **135**, A640 (1964).

[6] R. Feyerhem, S. Abens, D. Gunther, T. Ishida, M. Meibner, M. Meschke, T. Nogami and M. Steiner, J.

Phys. Condens. Matter. **12**, 8495 (2000).

[7] C. Coulon, H. Miyasaka and R. Clerac, Struct. Bond. **122**, 163 (2006).

[8] E. Ising, J. Math. Phys. **4**, 124 (1963).

[9] M.E. Fisher, J. Math. Phys. **4**, 124 (1963).

[10] M. Steiner, J. Villain and C.G. Windsor, Adv. Phys. **25**, 87 (1976).

[11] F. Boersma, W.J.M. de Jonge, and K. Kopinga, Phys. Rev. B. **23**, 186 (1981).

CHAPTER 3.

Experimental Techniques

3.1 Introduction

In this chapter, relevant details of the experimental techniques used for the structural and magnetic characterization of the TMPc samples are described. Most of the samples used in these investigations were purchased from Alfa Aesar and Sigma Aldrich. The exception was the sample of β-CuPc which was converted from the commercial α-CuPc using thermo-gravimetric analysis (TGA). All the samples were characterized by X-ray diffraction (XRD) and scanning electron microscopy (SEM) in order to acquire the information on the crystalline phases and morphology of the samples. The major portion of magnetization measurements in this dissertation were performed by using the AC Measurement System (ACMS) option of our in-house Physical Property Measurement System (PPMS) manufactured by Quantum Design Inc. Therefore some details of the techniques of TGA, XRD, SEM and ACMS are described below.

3.2 Thermo-gravimetric Analysis

Thermo-gravimetric Analysis (TGA) is a technique in which the mass of a substance is monitored as a function of temperature or time as the sample specimen is subjected to a controlled temperature program in a controlled atmosphere. TGA can provide useful information on both the physical and chemical properties of a sample, including thermal stability, oxidative stability, composition, estimated lifetime and decomposition kinetics [1]. In addition, TGA is an important technique for material

characterization for various environmental, food, pharmaceutical, and petrochemical industries [2-4].

In principle, TGA characterizes materials that exhibit weight loss or gain due to decomposition, oxidation, and dehydration. The reasons for weight loss in a material include decomposition, evaporation, reduction, and desorption. Materials can also gain weight during oxidation and absorption. Combining data provided by TGA with proper data analysis, the kinetics of various processes can also be studied.

The essential parts of TGA (shown in Fig. 3.1) are a furnace with controlled gas flow, a balance with a sample pan, and a computer. The furnace houses the sample (in a sample pan) and can provide the temperature from 20 ℃ up to 1000 ℃ with a controlled heating rate, normally 0.1 ℃/min to 100 ℃/min. The gas is normally nitrogen. The balance can measure the sample weight precisely and the sensitivity can reach 0.1 μg. The sample pan is made of Platinum, Aluminum, or ceramics, and its usage depends on the application. The computer controls all the programs and performs data analysis.
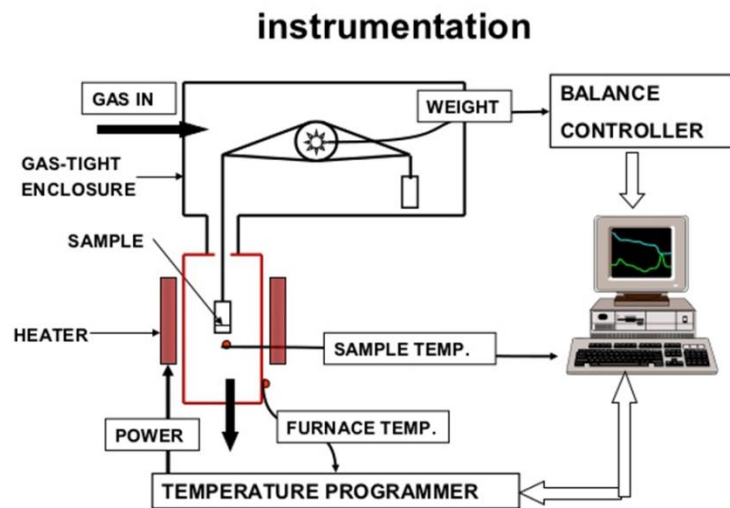
Fig. 3.1 *Instrumentation of TGA (adapted from [5]).*

41

In this research, TGA was used to convert to convert α-CuPc to β-CuPc by annealing it at 350 ℃ in nitrogen environment. The details of these results are described in Chapter 4. A Q50 TGA manufactured by TA Instruments was used for this purpose (see Fig. 3.2). About 30 mg α-CuPc powder sample was loaded onto a platinum pan and put in the furnace. After accurately weighing the sample, the temperature in the furnace was increased from 20 ℃ up to 350 ℃ with the heating rate of 10 ℃/min and kept at 350 ℃ for 3 hours. The annealing process was done in the N_2 environment by flowing N_2 gas. The weight vs. temperature and weight vs. time data are shown in Fig. 4.1 of Chapter 4 and its analysis is discussed in section 4.2.1.

Fig. 3.2 A photograph of the commercial Q50 TGA system used for experiments.

3.3 X-ray Diffraction

3.3.1: History and Production of X-rays

The discovery of X-ray in 1895 by Roentgen enabled scientists to probe crystalline structure at

the atomic level and the first diffraction pattern of a crystal was made by Knipping and von Laue in 1914. Soon after this, in 1915 Bragg developed the theory to determine the crystal structure from Bragg diffraction. Nowadays with the help of the high performance computers, X-ray diffraction (XRD) has become an essential tool for the determination of crystal structures and hence it is used extensively in academic laboratories as well as in medical, dental and pharmaceutical industries.

Solid matter can be described as amorphous or crystalline. For amorphous materials, the atoms are arranged in a random manner similar to the atomic disorder found in liquids. However, for crystalline materials, the atoms are arranged in a regular pattern which can be replicated from the unit cell of the structure. In three dimensions, the unit cell is defined by a-, b-, c-axis with angles between each two axes are called α, β, and γ. As an example, for a cubic unit cell a = b= c and $\alpha = \beta = \gamma = 90^{o}$. For basics of unit cells, x-ray diffraction and x-ray crystallography, the book by Cullity is a good source [6]. So far, diffraction patterns have been collected for about 50,000 inorganic and 25,000 organic single component, crystalline phases, which enable researchers to identify components in a sample using a search/match procedure.

X-rays are a part of the electromagnetic radiation with the wavelength from 0.01 nm to 10 nm (frequency from 3×10^{16} to 3×10^{19} Hz) depending on the source. As a result, the X-rays carry high energy photons (from 120 eV to 120 keV) and are quite penetrating. The relation of energy, wavelength, and frequency of a photon is as follows:

$$E = h\nu = \frac{hc}{\lambda}$$
(3.1)

In Eq. (3.1), E is the photon energy, h is Planck constant, c is speed of light, and λ is the wavelength.

X-rays are commonly produced by bombarding a metal target (e.g. Cu, Mo) with a beam of high-speed electrons (accelerated by high voltage) emitted from a hot filament (often tungsten), as shown in Fig. 3.3. The incident beam will ionize electrons from the K-shell (1s) of the target atom and X-rays are emitted as the resultant vacancies are filled by electrons dropping down from the L (2p) or M (3p) levels. This gives rise to Kα and Kβ lines (see Fig. 3.4 and Fig.3.5). For example, the wavelengths of Cu-Kα and Mo-Kα are 0.15418 nm and 0.07107 nm, respectively. In practical x-ray systems, Kβ lines are usually absorbed by a filter so that nearly monochromatic source of x-rays is available for experiments.

The wavelength of the emitted X-rays with applied voltage V is given by:

$$\lambda = \frac{hc}{E} = \frac{hc}{eV} = \frac{(6.626 \times 10^{34})(3 \times 10^8)(10^9)}{(1.6 \times 10^{-19})V} = \frac{1.24}{V(kV)} \, nm \qquad (3.2)$$
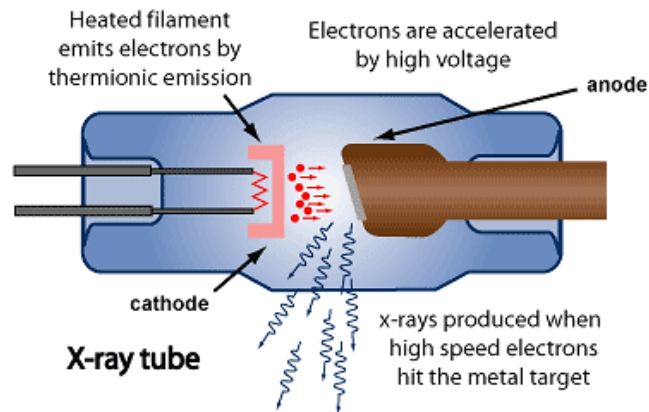
Fig. 3.3 *Schematic diagram of X-ray tube (adapted from [7]).*

In 1913, Moseley was the first person to show that the frequencies ν of X-rays emitted from

chemical elements are proportional to the square of a number which was close to the element's atomic number Z. Specifically this relation (Moseley's law) is given by $\nu = K\,(Z\text{-}\sigma)^2$ where K is a universal constant for all elements and σ is another universal constant representing electron screening effect. Soon after Moseley's discovery, in 1914 it was realized that Moseley's formula could be adapted from Bohr's equation, as following:

$$E = h\nu = E_i - E_f = \frac{m_e q_e^4 (Z - \sigma)^2}{8h^2 \varepsilon_0^2}\left(\frac{1}{n_f^2 - n_i^2}\right) \tag{3.3}$$

$$\nu = \frac{m_e q_e^4 (Z - \sigma)^2}{8h^3 \varepsilon_0^2}\left(\frac{1}{n_f^2 - n_i^2}\right) \tag{3.4}$$

Here m_e is the mass of electron, q_e is the charge of electron, Z is the atomic number, ε_0 is the permittivity of the vacuum, n_f and n_i are final and initial energy level, respectively.
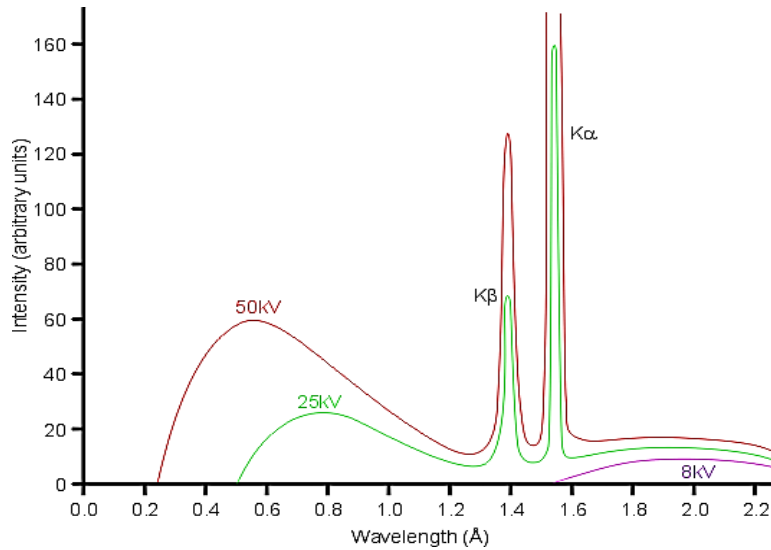
Fig. 3.4 *Intensity vs. wavelength of X-rays for three applied voltages (adapted from [8]).*
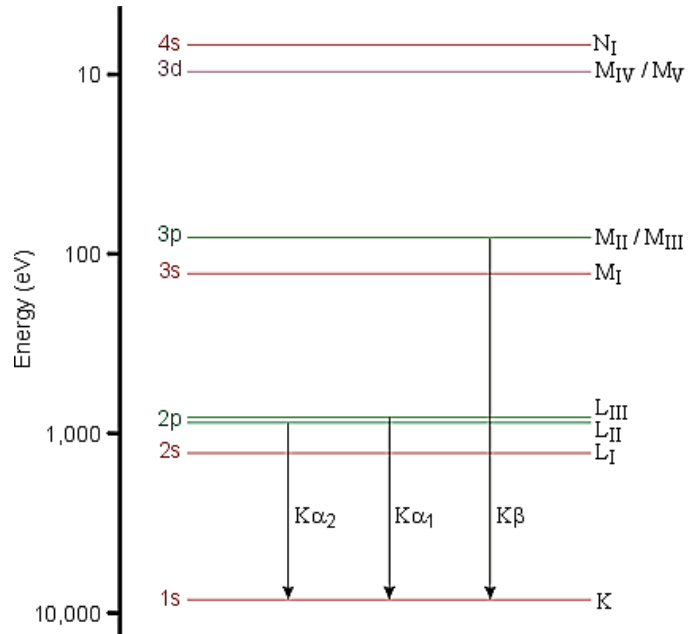
Fig. 3.5 *Energy level involved in CuK X-ray emission (adapted from [7]).*
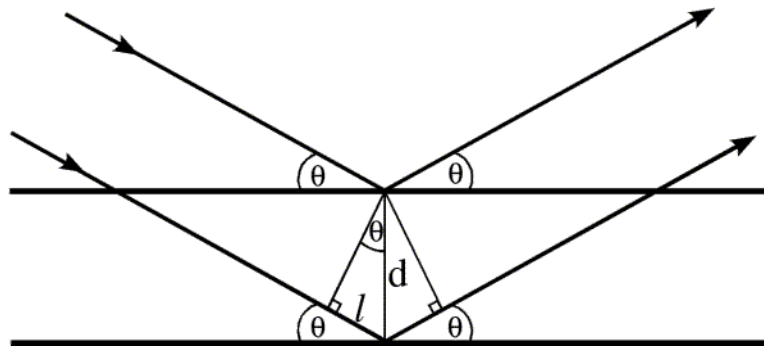
Fig. 3.6 *Diffraction of X-rays from two parallel containing atoms (adapted from [9]).*

3.3.2 Bragg's Law and Determination of Crystal Structures:

Consider an x-ray beam of wavelength λ incident on a pair of parallel planes, separated by an inter-planar spacing d, as shown in Fig.3.6. The diffraction of X-ray is governed by Bragg's law:

$$2d\sin\theta = n\lambda \tag{3.5}$$

Here θ is the incident angle and $n = 1, 2, 3 \,\text{---}$ gives the order of diffraction. The various observed Bragg peaks as a function of the diffraction angle can be indexed by Miller indices (hkl) representing various planes. For the TMPc samples, analysis of such data is presented in the subsequent chapters for each sample. This analysis requires comparing the measured d-values determined from Eq. (3.5) and comparing them with the d-values calculated for the expected structure. The d-spacings of triclinic structure in terms of the Miller indices (hkl) is given by [6]:

$$\frac{1}{d^2} = \frac{1}{V^2}(S_{11}h^2 + S_{22}k^2 + S_{33}l^2 + 2S_{12}hk + 2S_{23}kl + 2S_{13}hl) \tag{3.6}$$

with
$$S_{11} = b^2c^2\,(\sin\alpha)^2 \tag{3.7}$$

$$S_{22} = a^2c^2\,(\sin\beta)^2 \tag{3.8}$$

$$S_{33} = a^2b^2\,(\sin\gamma)^2 \tag{3.9}$$

$$S_{12} = abc^2(\cos\alpha\cos\beta - \cos\gamma) \tag{3.10}$$

$$S_{23} = a^2bc(\cos\beta\cos\gamma - \cos\alpha) \tag{3.11}$$

$$S_{13} = ab^2c(\cos\gamma\cos\alpha - \cos\beta) \tag{3.12}$$

Here α, β, γ are angles between a-b axes, b-c axes, and a-c axes respectively. The volume V is given by

$$V = abc\sqrt{1 - (\cos \alpha)^2 - (\cos \beta)^2 - (\cos \gamma)^2 - 2 \cos \alpha \cos \beta \cos \gamma} \qquad (3.13)$$

For the monoclinic structure, $\alpha = \gamma = 90°$ and so Eq. (3.6) becomes

$$\frac{1}{d^2} = \frac{1}{\sin^2\beta}\left(\frac{h^2}{a^2} + \frac{k^2\sin^2\beta}{b^2} + \frac{l^2}{c^2} - \frac{2hl\cos\beta}{ac}\right) \qquad (3.14)$$

In a similar manner, relations for d-spacing of other crystal structures is easily derived using the general equations given above. For the samples of α-CuPc, β-CuPc, β-CoPc, β-NiPc, and β-MnPc investigated here, the crystal structure is monoclinic whereas the crystal structure of for VOPc (phase II) is triclinic.

For all the samples investigated in this work, the XRD patterns were acquired at room temperature using the   PANalytical X'Pert Pro X-ray difractometer with Cu-Kα source ($\lambda = 0.15418$ nm) available from the WVU Shared Research Facilities. The patterns of the scattered x-ray intensity versus scattering angle 2θ were obtained using a step size of 0.05 ° and an integration time of 1.20 s for each step. The XRD generator was set to 40 mA and 45 kV. The analysis and discussion of the XRD data of all the investigated here is given in subsequent chapters along with the presentation and discussion of their magnetic properties.

3.4 Scanning Electron Microscopy (SEM)

At the request of the author and Professor Seehra, scanning electron microscopy of the TMPc powder samples was done by Mr. James Poston of the National Energy Technology Laboratory, U.S. Department of Energy, located in Morgantown, WV. According to the information provided by Mr. Poston, he used a JEOL 7600 FE-SEM system available in his laboratory. A brief summary of the working

principles of SEM is given below.
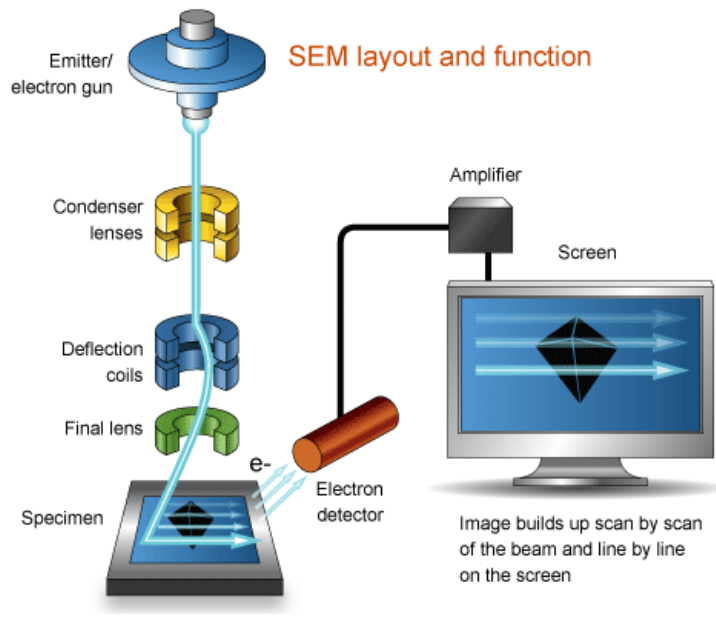
Fig. 3.7 *Schematic diagram of the key components of SEM systems (adapted from [10]).*

A scanning electron microscope (SEM) uses electrons, rather than light, to create the magnified image. Since first commercialization of SEM about 40 years ago, good quality SEM systems have now magnifications of up to 10^5 with a resolution of 1nm ~ 2 nm. When a specimen is irradiated with a fine electron beam (called an electron probe), secondary electrons are emitted from the specimen surface. Topography of the surface can then be observed by two-dimensional scanning the electron probe over the surface and acquisition of an image from the detected secondary electrons.

A schematic diagram of the instrumentation of SEM is shown in Fig. 3.7. The electron gun produces an electron beam by heating the filament (usually Tungsten) at high temperatures and the electron beam passes through a high voltage (1 keV to 30 keV) region which accelerates the electrons. Then the high energy electron beam passes through condenser lenses, deflection coils, and final lens in

order to adjust the diameter of the beam as well as getting a focused beam. When the incident beam enters

the specimen, secondary electrons are produced from the emission of the valence electrons of the atoms in

the specimen. Since the energy of secondary electrons is very small, those generated at a deep region are

quickly absorbed by the specimen. Only those generated at the top of the specimen are emitted outside of

it and as a result, the secondary electrons are very sensitive to the surface. Finally the secondary electrons

are collected by the electron detector, amplified, and sent to the computer for data analysis. In addition,

the inside of the electron optical system and specimen chamber must be kept at a high vacuum (10^{-3} Pa to

10^{-4} Pa). This is because the chemical and thermal stability is necessary for a well-functioning filament

(gun pressure). Also, the electron beam must travel to the specimen and secondary electrons must travel

from the specimen to the detector without colliding with other atoms or molecules.

3.5 Specifics of the AC Measurement System (ACMS)

The ACMS option for the in-house PPMS acquired from Quantum Design Inc. is a versatile DC

magnetometer and AC susceptometer. The available temperature range is from 2 K to 350 K in the sample

region with temperature resolution stability of 0.1 K. The available magnetic field is up to ± 90 kOe (± 9

T) for DC magnetization measurement and up to ± 10 Oe for the AC magnetization measurement in the

frequency range from 10 Hz to 10^4 Hz. As shown in Fig. 3.8, the ACMS insert houses the drive and

detection coils, thermometer, and electrical connections for the ACMS system. Note that the detection

coils consist two sets of counter-wound copper coils connected in series and separated by several

centimeters. The sample is held within the insert's coil set on the end of a thin, rigid sample rod and can

be translated longitudinally by a DC servo motor located in the ACMS sample transport assembly. The

DC servo motor provides rapid and very smooth longitudinal sample motion. The system does not use a

lock-in amplifier but a digital signal processor (DSP) that synthesizes the excitation signal and processes

the detection coils' response signal.
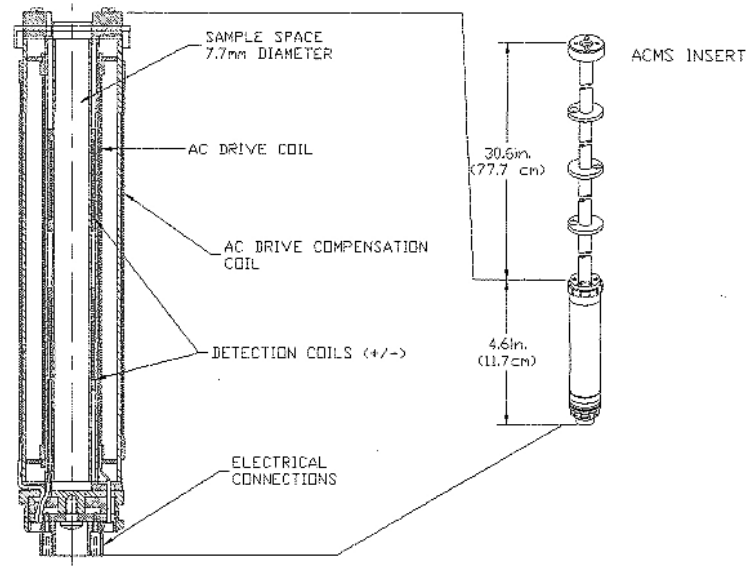
Fig. 3.8 ACMS insert and coil set (adapted from [11]).

DC magnetization measurements measure a sample's magnetic moment M in an applied field H

at a specific temperature T (M = M (H, T)). During DC magnetization measurements, a constant field

(generated by the PPMS superconducting magnet) is applied to the measurement region and the sample is

moved automatically and very quickly in 0.05 sec (v ≈ 100 cm/s) through both sets of the detection coils,

introducing a signal (induced emf) in them according to Faraday's law:

$$\varepsilon = -\frac{1}{c}\frac{\partial \Phi}{\partial t} \qquad (3.15)$$

Here ε is the induced emf and Φ is the magnetic flux which is proportional to the sample's magnetic

moment and coil geometry. This measurement method is commonly called the extraction method. The system is calibrated using a standard sample of pure Pd (supplied by Quantum Design Inc.) with temperature and magnetic field independent magnetic susceptibility $\chi = 5.24 \times 10^{-6}$ emu/gOe.

AC magnetization measurements do not directly measure a sample's magnetic moment; instead, the change of the magnetic moment is measured:

$$\chi_{ac} = \frac{dM}{dH} \tag{3.16}$$

This is the local slope of the sample's magnetization curve M(H) and not the "true" susceptibility. During AC magnetization measurements, an alternating field (up to ± 10 Oe and frequency between 10 Hz and 10^4 Hz) is generated by the AC drive coil and applied to the measurement region. The sample is positioned in the center of the detection coils and the detection coils indicate how the applied field is altered by the presence of the sample.

There are many factors to consider when determining whether to use AC or DC magnetization measurements. For the ACMS option, AC magnetization measurements are nearly three orders of magnitude more sensitive than DC magnetization measurements. Conductive samples usually yield much larger signals during AC magnetization measurements. However, in some situations, DC magnetization measurements produce better results than AC magnetization measurements. For example, weakly paramagnetic samples with magnetic moments near the noise floor of the ACMS's AC measurement capability ($\sim 1 \times 10^{-8}$ emu) can often be detected more easily in the large DC fields applied by the PPMS superconducting magnet, because the larger DC field raises the sample's moment well above the noise

52

floor for DC measurements ($\sim 2.5 \times 10^{-5}$ emu).

A computer sequence is needed for each set of magnetic measurements. Examples of such sequences generated by the author for three typical experiments are given in Appendix B.

References

[1] A.W. Coats and J.P. Redfern, Analyst. **88**, 906 (1963).

[2] D. Bom, R. Andrews, D. Jacques, J. Anthony, B. Chen, M.S. Meier, and J.P. Selegue, Nano Lett. **2**, 615 (2002).

[3] U.K. Sharma, A. Verma, S.K. Prajapati, H. Pandey, and A.C. Pandey, Appl. Nanosci. **5**, 143 (2015).

[4] I. Blanco and V. Siracusa, J. Therm. Anal. Calorim. **112**, 1171 (2013).

[5] http://www.slideshare.net/nimmidalwadi5/tga

[6]. B. D. Cullity, "Elements of X-Ray Diffraction" (Addison-Wesley Publishing Co., Reading, MA 1959)

[7] http://www.arpansa.gov.au/radiationprotection/basics/xrays.cfm

[8] http://pd.chem.ucl.ac.uk/pdnn/inst1/xrays.htm

[9] http://www-structmed.cimr.cam.ac.uk/Course/Basic_diffraction/Diffraction.html

[10] http://www.ammrf.org.au/myscope/sem/practice/principles/layout.php#detail

[11] PPMS ACMS User's Manual, Quantum Design Inc.

CHAPTER 4.

Magnetic Properties of α- and β- Copper Phthalocyanines

4.1 Introduction

In this chapter, results from the measurements of the magnetization (M) of α-CuPc and β-CuPc samples are presented covering the temperature range of 2 K to 250 K and in magnetic fields up to 90 kOe available with the in-house commercial PPMS. The data are analyzed and discussed in terms of Curie-Weiss (CW) law and the Bonner-Fisher (BF) model for a Heisenberg linear chain. The results are also compared to the previous investigations of these materials [1], which did not cover such large ranges of temperatures and magnetic fields. A major portion of the results presented in this chapter have been published by the author in a recent paper [2].

4.2 Samples and their Structural Characterization

4.2.1 Samples

The CuPc powder was purchased from Alfa Aesar (stock #43650) and confirmed as α-phase by x-ray diffraction (shown later). The structure of β-CuPc is more stable thermally than that of α-CuPc since β-CuPc can be obtained by annealing α-CuPc in N_2 gas at 350 ℃ for 3 hours as reported by Lozzi et al. [3]. This experiment was performed by using the in-house TGA (Thermo-gravimetric Analysis) system, model Q50 manufactured by TA Instruments Inc. The sample of α-CuPc powder was placed on the pan balance which was further lowered into the furnace of the TGA system and heated from 20 ℃ to 350 ℃ at a heating rate of 10 ℃/min. The N_2 gas was introduced into the furnace while the sample was heating

in order to keep the environment inert. With increase in temperature, the sample weight decreases by a few percent most likely due to the loss of adsorbed moisture in the sample. Once the temperature reached 350 ℃, there was no further loss in the weight as evident in figure 4.1(a). The sample was kept at 350 ℃ for 3 hours followed by cooling it to room temperature in flowing N_2 gas. X-ray diffraction of this annealed sample confirmed it to have the β-phase of CuPc as shown in the following section.
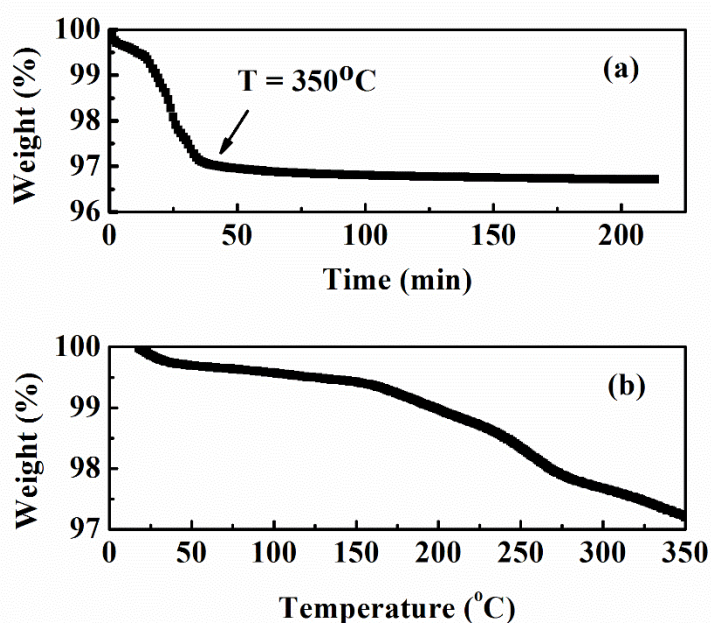
Fig. 4.1 *Plots of weight vs. time (a) and weight vs. temperature (b) of α-CuPc powder sample during the annealing process. The temperature of sample was varied from 20 ℃ to 350 ℃ at a heating rate of 10 ℃/min in flowing N_2 gas, then kept constant at 350 ℃ for three hours.*

4.2.2 X-ray Diffraction (XRD)

The x-ray diffraction (XRD) of the purchased powder sample was performed at room temperature using a PANalytical X'Pert Pro X-ray Diffractometer with monochromatic Cu-Kα radiation of wavelength λ = 0.15418 nm (Fig.4.2). The analysis of the XRD pattern showed the structure to match

perfectly with that of α-CuPc having space group C2/c with four molecules per unit cell of the monoclinic structure and lattice parameters: a = 2.592 nm, b = 0.379 nm, c = 2.392 nm, and β = 90.4° [4,5]. The XRD of the annealed sample, also shown in Fig.4.2, confirmed the conversion to the β-phase having space group $P2_1/a$ and two molecules per unit cell of the monoclinic structure with lattice parameters: a = 1.9407 nm, b = 0.479 nm, c = 1.4628 nm, and β = 120.56° [3, 6, 7]. Note that all the observed lines in Fig. 4.2 for both phases could be indexed using the respective parameters listed above although the Miller indices of only the most prominent lines are shown in Fig. 4.2 to avoid over-crowding the figures. The unit cells of α-and β-phases are shown in Fig. 1.1(chapter 1) with magnitudes of the cell parameters listed in Table 1.1. Note that the Cu-Cu chain is along the b-axis with Cu-Cu distance of 0.379 nm (0.479 nm) and the stack angle δ = 65° (45°) for the α(β) phase [8]. These structural differences are used later to interpret the observed differences in the measured magnetic properties of the two phases of CuPc.
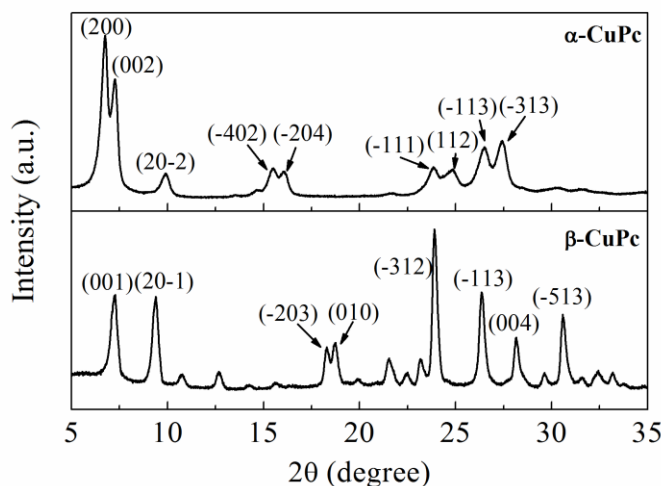
Fig. 4.2 XRD patterns of α-CuPc and β-CuPc powder sample with Miller indices of major lines shown. No impurity lines were observed in either case.

4.2.3 Scanning Electron Microscopy (SEM)

Scanning electron micrographs of both α-CuPc and β-CuPc powder samples were obtained by using a JEOL 7600 FE-SEM system at the DOE National Energy Technology Laboratory (NETL). These micrographs shown in Fig. 4.3 were acquired by Mr. James Poston of NETL. It is evident from Fig. 4.3 (a) that α-CuPc has particles of irregular shape with size of some particles as low as 30 nm where as β–CuPc has rod-like morphology (Fig. 4.3b).
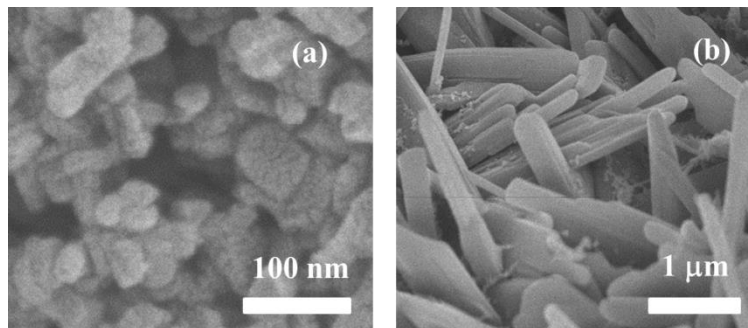
Fig. 4.3 *Scanning electron micrographs for (a) α-CuPc and (b) β-CuPc. The length scale bars are 100 nm and 1 μm for (a) and (b), respectively.*
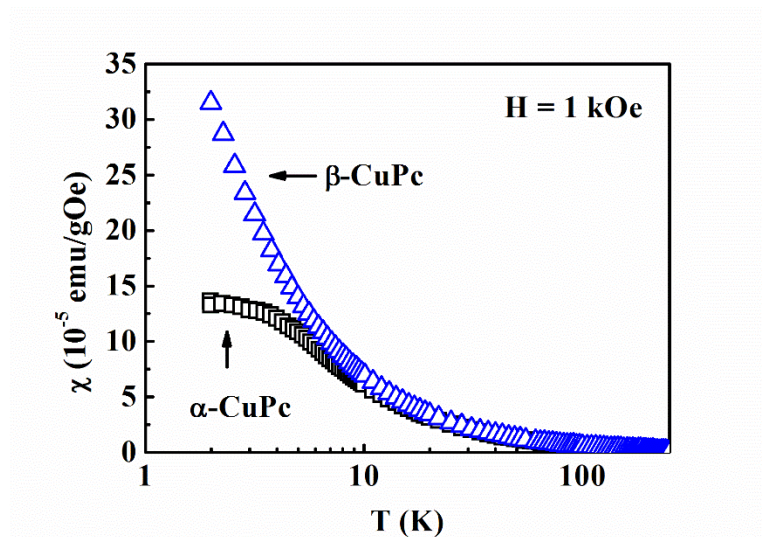
Fig. 4.4 *Magnetic susceptibility χ vs. temperature T data for α-CuPc and β-CuPc in H = 1 kOe.*

4.3 Results from Magnetic Measurements, Analysis, and Discussion

4.3.1 Temperature Dependence of DC Magnetization and the Curie-Weiss Law

Measurements of the magnetization M as a function of temperature T and magnetic field H were performed using the physical property measurement system (PPMS) described in Chapter 3. The temperature dependence of the magnetic susceptibility χ = (M/H) for both α-CuPc and β-CuPc samples measured at H = 1 kOe is shown in Fig. 4.4. For both samples, χ increases with decreasing T. However for α-CuPc, a plateau is reached around 2 K whereas it is absent for β-CuPc.

The data were first fit to the modified Curie-Weiss (CW) law, $\chi = \chi_o + C / (T-\theta)$, where χ_o is the diamagnetic contribution estimated from the high-temperature limit by plotting χ vs. 1/T and extrapolating to the limit 1/T = 0 (see Fig. 4.5). The fits give χ_o = - 2.96 $\times 10^{-6}$ (- 2.70 $\times 10^{-6}$) emu/gOe for α-CuPc (β-CuPc). The diamagnetic contributions to χ_o come from the samples as well as the sample holder used in the measurements although the effects of χ_o are only noticeable at T > about 100 K. However this correction is essential for the accurate analysis of the data in the whole temperature range.
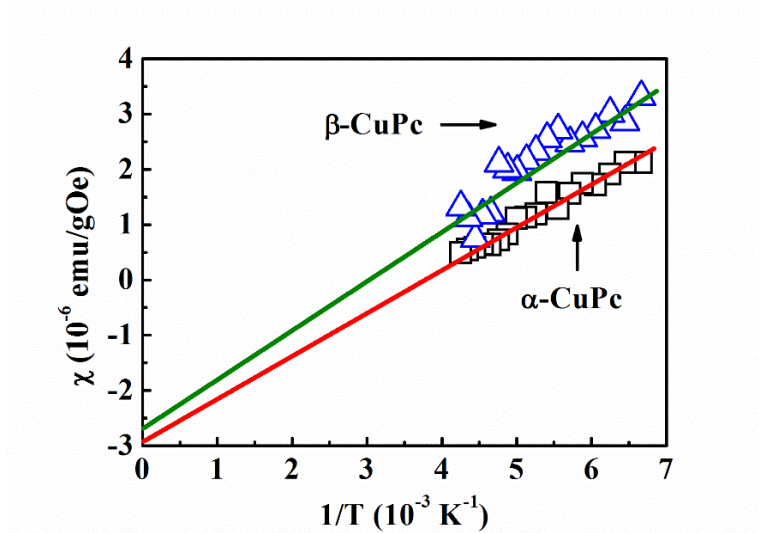
Fig. 4.5 *Magnetic susceptibility χ vs. 1/T plots for α-CuPc and β-CuPc. The solid lines are linear fits with the intercepts giving χ_o = - 2.96 × 10⁻⁶ (- 2.70 × 10⁻⁶) emu/gOe for α-CuPc (β-CuPc).*

After determining χ_o, next $(\chi - \chi_o)^{-1}$ vs. T is plotted as shown in Fig. 4.6 to check the validity of the Curie-Weiss law. The linear fits in Fig. 4.6 yielded C = 7.96 × 10⁻⁴ (7.20 × 10⁻⁴) emu-K/gOe and θ = - 2.3 K (- 0.2 K) for α-CuPc (β-CuPc), the negative θ signifying antiferromagnetic exchange coupling. Using the above magnitudes of χ_o, C, and θ, fits to the modified CW law and experimental data are compared in Fig. 4.7 for both α-CuPc and β-CuPc. From the solid lines in Fig. 4.7 representing fits to the CW law, it is evident that for α-CuPc, the data does not fit the CW law below about 4 K whereas for β-CuPc, the fit to the CW law is quite good down to 2 K, the lowest temperature attainable in these experiments.
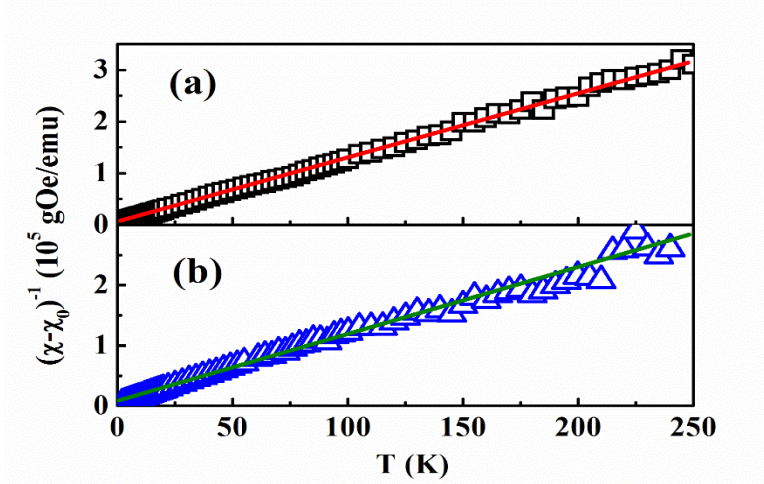
Fig. 4.6 *Plots of $(\chi - \chi_o)^{-1}$ vs. T for (a) α-CuPc and (b) β-CuPc. The solid lines are linear fits representing the CW law with $C = 7.96 \times 10^{-4}$ (7.20×10^{-4}) emu-K/gOe and θ = - 2.3 K (- 0.2 K) for α-CuPc (β-CuPc).*

As discussed in Chapter 2, the Curie constant $C = N\ \mu^2/3k_B$ where N is the number of magnetic ions per gm, μ is the magnetic moment per ion and k_B is the Boltzmann constant. Using the evaluated $C = 7.96 \times 10^{-4}$ emu-K/gOe for α-CuPc yields magnetic moment μ = 1.9145 μ_B which in turn yields S = 1/2 and g = 2.21 using $\mu^2 = g^2S(S+1)\mu_B^2$, as predicted for Cu^{2+} in α-CuPc by the DFT calculations of Mugarza et al. [9]. Also θ = - 2.3 K shows antiferromagnetic (AFM) Cu^{2+}-Cu^{2+}exchange coupling which is also evident by deviations from the CW law below 4 K in Fig. 4.7. Using the similar procedure for β-CuPc and the fitted $C = 7.20 \times 10^{-4}$ emu-K/gOe, yields μ = 1.8221 μ_B, spin S = 1/2 and g = 2.10. The magnitude of θ = - 0.2 K in β-CuPc shows a considerable weaker AFM Cu^{2+}-Cu^{2+}exchange coupling in this system. Also, note that the g-factor for both α-CuPc and β-CuPc shows the positive g-shift because the shell is more than half-filled, as discussed in Chapter 2. These g-shifts result from the partially restored orbital contributions to the magnetic moment via the spin-orbit interaction, as shown in Eq. (2.35) and Eq. (2.37).
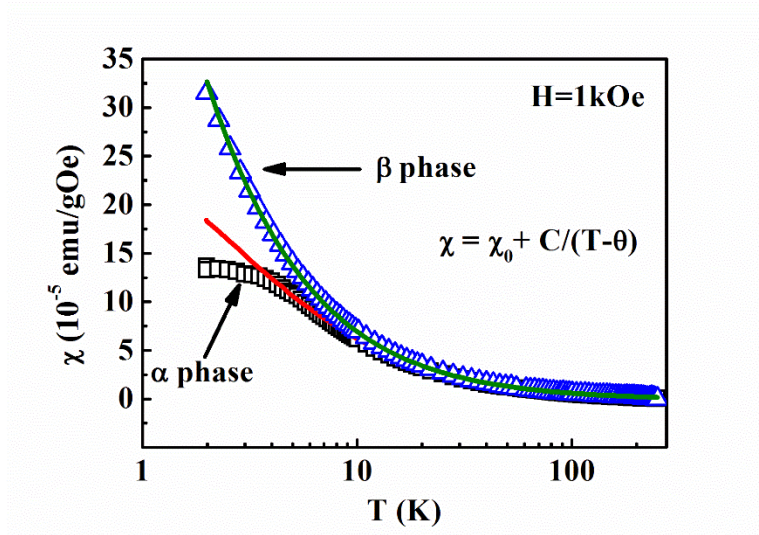
Fig. 4.7 *Magnetic susceptibility χ vs. temperature T for α-CuPc and β-CuPc. The solid lines are fits to the modified Curie-Weiss law with the fitting parameters listed in the caption to Fig. 4.6.*

The Heisenberg exchange constant J_{ex}/k_B can be estimated by the mean field theory following Eq. (4.1) derived in Chapter 2:

$$J_{ex} = \frac{3\theta}{2ZS(S+1)} \tag{4.1}$$

Here θ is the Weiss constant, S is the spin, and Z is the number of the nearest neighbors of each Cu^{2+}. For both α-CuPc and β-CuPc, Z = 2 (for a linear chain) and spin S = 1/2 yielding

$$J_{ex} = \theta \tag{4.2}$$

This gives exchange constant J_{ex}/k_B = - 2.3 K (- 0.2 K) for α-CuPc (β-CuPc) using the mean-field theory. These magnitudes of J_{ex}/k_B are compared with those obtained from fitting the χ vs. temperature T data to the more accurate Bonner-Fisher model. This analysis and discussion is presented in the following section.

61

4.3.2 Fit to the Bonner-Fisher Model

The chain configuration of the CuPc molecules along the b-axis is evident from Fig. 1.1. Consequently the data of χ vs. T was next fitted to the predictions of the Bonner-Fisher (BF) model [10] for a spin S = 1/2 linear chain with Heisenberg AFM exchange-coupling J_{ex} defined by the Hamiltonian H = $-2J_{ex}\Sigma \, \mathbf{S_i} \cdot \mathbf{S_{i+1}}$. Following Eggert et al. [11] and Feyerherm et al. [12], the variation of χ vs. T for a linear chain model S = 1/2 system with the normalized AFM coupling parameter $x = |J_{ex}|/(k_B T)$ is given by

$$\chi = \chi_o + \frac{C}{T}F(x) \tag{4.3}$$

$$F(x) = \frac{1 + a_1 x + a_2 x^2}{1 + b_1 x + b_2 x^2 + b_3 x^3} \tag{4.4}$$

Here C is the Curie constant, a_1 = 0.17032, a_2 = 0.93404, b_1 = 1.46764, b_2 = 0.54784, and b_3 = 4.28544. Note that for x = 0 (meaning J_{ex} = 0), χ = C/T is obtained which is the usual Curie-law as expected. In Fig. 4.8, the fit of the data of χ vs. T to the predictions of this model for both α-CuPc and β-CuPc are shown as solid lines with J_{ex}/k_B = - 1.7 K (- 0.2 K) for α-CuPc (β-CuPc), within uncertainty of 0.1 K in the magnitudes of J_{ex}/k_B. In these fits, the magnitude of J_{ex} was varied till the best fit was obtained in the whole temperature range. Excellent fits are obtained in both cases with the model correctly showing the broad maximum indicated in the χ vs. T data for α-CuPc. For β-CuPc, the broad maximum is predicted to occur near T = 0.25 K (inset of Fig. 4.8) because of the lower magnitude of J_{ex}/k_B = - 0.2 K in this system. However this lower temperature of T = 0.25 K was not attainable in our experiments.

The CW law can also be derived from Eq. (4.4) by retaining only the first order term in x. This

exercise leads to the CW law with θ = 1.29732 J_{ex}/k_B. Using J_{ex}/k_B = - 1.7 K (- 0.2 K) for α-CuPc (β-CuPc)

yields θ = - 2.2 K (θ = - 0.26 K) for α-CuPc (β-CuPc), comparing favorably with the experimental values

of θ = - 2.3 K and θ = - 0.2 K respectively. At lower temperatures, higher order terms in x become

increasingly important particularly for linear chains and 2-D systems [14].
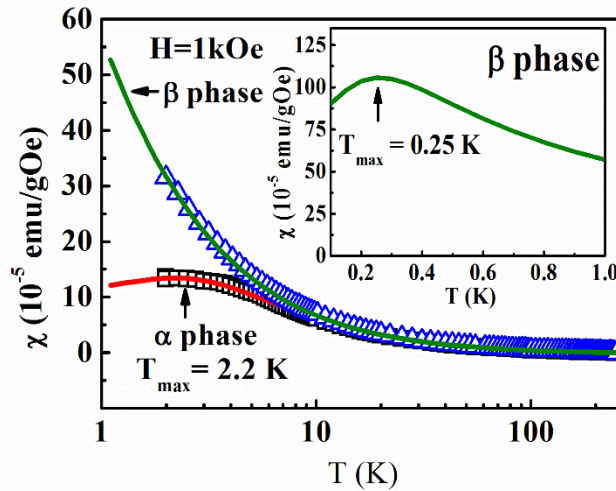
Fig. 4.8 *Data of χ vs. T of Fig. 3.5 for the α- and β-phases of CuPc are fitted to Eq. (3.1) with the solid lines as fits yielding the exchange constant J_{ex}/k_B = -1.7 K (- 0.2 K) for α(β) phase. The fit also gives T_{max} = 2.2 K for α-phase and calculated T_{max} = 0.25 K for β-phase (see inset).*

Since the Cu^{2+}-Cu^{2+} exchange interaction requires overlap of the wave functions of

neighboring Cu^{2+} ions either directly or through the intervening N atoms, this order of magnitude

difference in the magnitude of J_{ex}/k_B is likely due to the smaller Cu-Cu distance in the α-phase than in

β-phase (Fig. 1.1) as noted earlier. The difference in the stack angles δ of the two phases may also be an

important factor (see Fig. 1.1). The recent calculations of Wu et al. [13] using DFT have predicted J_{ex}/k_B =

- 1.3 K (- 0.14 K) for α-CuPc (β-CuPc). Our experimentally measured values of J_{ex}/k_B for both systems

are about 30 % larger than the DFT predictions. For S = 1/2, the temperature T_{max} where the maximum in

χ vs. T occurs is given by $T_{max} \simeq 1.3|J_{ex}|/k_B$ for the linear chain Bonner-Fisher model whereas $T_{max} \simeq$ 0.91J_{ex}/k_B for 2-D square lattice [14].
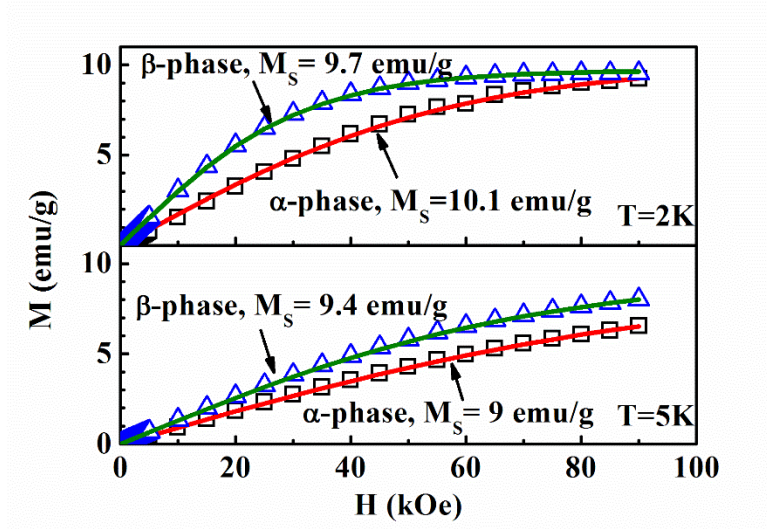
Fig. 4.9 *Magnetization M vs. magnetic field H of α- and β-phases of CuPc at 2 K and 5 K. The solid lines represent fits to Eq. (4.5) with θ = - 2.3 K (- 0.2 K) for α(β)-phase.*

4.3.3 Magnetic Field Dependence of Magnetization

The isothermal data of M vs. H up to H = 90 kOe and measured at 2 K and 5 K for both samples are shown in Fig. 4.9. In the absence of exchange interaction (θ = 0), the data of M vs. H are expected to fit the Brillouin function variation which for S = 1/2 reduces to the following Eq. (4.5) in which the effect of exchange interaction is taken into account by including θ analogous to the CW law [15]:

$$M = M_S \tanh \frac{g\mu_B H}{2k_B(T - \theta)} \tag{4.5}$$

Efforts to fit the data with $\theta = 0$ led to unsatisfactory fits especially for α-CuPc because of the larger magnitude of θ and hence exchange interaction in this system. Next, the data is fitted with $\theta = - 2.3$ K (α-phase) and $\theta = - 0.2$ K (β-phase) in analogy with the CW law noted earlier, yielding good fits to the data with $M_S = 10.1$ emu/g (9 emu/g) at 2 K (5 K) for α-CuPc and $M_S = 9.7$ emu/g (9.4 emu/g) at 2 K (5 K) for β-CuPc. The calculated magnitude of $M_S = N\ g\ \mu_B\ S = 10.7$ emu/g for α-CuPc and $M_S = 10.2$ emu/g for β-CuPc at 0 K using $S = 1/2$ and $g = 2.21$ (2.10) evaluated earlier for α-CuPc (β-CuPc). This discrepancy of few percent between the calculated and experimental magnitudes of M_S likely results from lack of saturation at 2 K and from the effects of zero-point spin deviations known to exist in antiferromagnetically coupled systems [16].

4.3.4 Temperature Dependence of AC Magnetization

The AC magnetization for α-CuPc was measured from 2 K to 20 K without DC magnetic field but with a small AC magnetic field $H_{ac} = 5$ Oe. As shown in Fig. 4.10, the real part of susceptibility χ' is the same for all three frequencies. For the imaginary part of susceptibility χ'', there is a hint of weak peaks near 2.5 K. However, the data are too noisy because of the smaller magnitudes of χ'' and so no reliable result for the shift of the peak with the measuring frequency could be obtained which is essential for determining the specifics of the relaxation phenomenon. Such an analysis is presented in the case of β-MnPc in a later chapter.
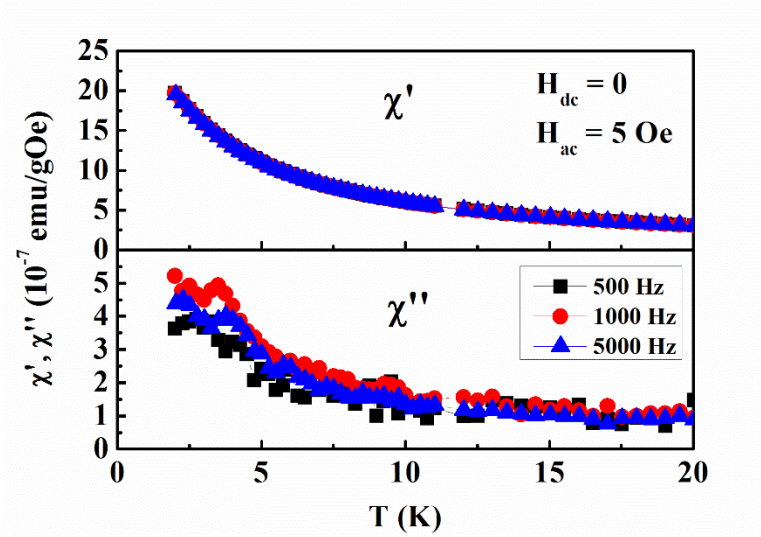
Fig. 4.10 *Temperature dependence of the ac susceptibilities χ' and χ'' for α-CuPc measured in zero applied static field with H_{ac} = 5 Oe at frequency f = 500 Hz, 1000 Hz, and 5000 Hz.*

4.4 Conclusions:

The major conclusions from the results presented in this chapter can be summarized as follows: (i) The electronic state of Cu in both α-CuPc and β-CuPc is shown to be Cu^{2+} with spin 1/2; (ii) The fits of the magnetic susceptibility versus temperature data to the Curie-Weiss law yields θ = - 2.3 K, μ = 1.9145 μ_B, and g = 2.21 for spin S = 1/2 for α-CuPc; and θ = - 0.2 K, μ = 1.822 μ_B, g = 2.10 for spin S = 1/2 for β-CuPc. The g-shifts from the free electron value of 2.0023 result from the partially restored orbital contribution to the magnetic moment via spin-orbit coupling; (iii) The fits of the magnetic susceptibility versus temperature data to the Bonner-Fisher model for linear Heisenberg chains yield the Heisenberg exchange constant J_{ex}/k_B = - 1.7 K (- 0.2 K) between the Cu^{2+}-Cu^{2+} ions in α-CuPc (β-CuPc). This order of magnitude difference in the magnitude of J_{ex}/k_B is likely due to the smaller Cu-Cu distance in the α-phase than in β-phase; (iv) The isothermal data of M vs. H at 2 K and 5 K are interpreted by including the effect of the exchange interaction; (v) Finally, the results show that both α- and β-CuPc are

good examples of antiferromagnetically coupled Heisenberg linear chains with spin S = 1/2 and negligible

interchain coupling.

References

[1] S. Heutz, C. Mitra, W. Wu, A.J. Fisher, A. Kerridge, M. Stoneham, A.H. Harker, J. Gardener, H.-H.

Tseng, T.S. Jones, C. Renner and G. Aeppli, Adv. Mater. **19**, 3618 (2007).

[2] Z. Wang, K.L. Pisane and M.S. Seehra, IEEE. Trans. Mag. **51**, 2700104 (2015).

[3] L. Lozzi, S. Santucci, R. La Rosa, B. Delley and S. Picozzi, J. Chem. Phys. **121**, 1883 (2004).

[4] A. Hoshino, Y. Takenaka and H. Miyaji, Acta. Crystallogr. B. **59**, 393 (2003).

[5] E. Jungyoon, S. Kim, E. Lim, D. Cha and B. Friedman, Appl. Surf. Sci. **205**, 274 (2003).

[6] O. Berger, W.-J. Fischer, B. Adolphi, S. Tierbach, V. Melev and J. Schreiber, J. Mater. Sci., Mater.

Electron. **11**, 331 (2000).

[7] C.J. Brown, J. Chem. Soc. A. **90**, 2488 (1968).

[8] W. Wu, A. Kerridge, A.H. Harker and A.J. Fisher, Phys. Rev. B. **77**, 184403 (2008).

[9] A. Mugarza, R. Robles, C. Krull, R. Korytar, N. Lorente and P. Gambardella, Phys. Rev. B. **85**, 155437 (2012).

[10] J.C. Bonner and M.E. Fisher, Phys. Rev. **135**, A640 (1964).

[11] S. Eggert, I. Affleck and M. Takahashi, Phys. Rev. Lett. **73**, 332 (1994).

[12] R. Feyerhem, S. Abens, D. Gunther, T. Ishida, M. Meibner, M. Meschke, T. Nogami and M. Steiner, J. Phys. Condens. Matter. **12**, 8495 (2000).

[13] W. Wu, A.J. Fisher and N.M. Harrison, Phys. Rev. B. **84**, 024427 (2011).

[14] M.S. Seehra, Phys. Lett. A. **28**, 754 (1969).

[15] V. Narang, D. Korakakis and M.S. Seehra, J. Appl. Phys. **116**, 213911 (2014).

[16] P.W. Anderson, Phys. Rev. **86**, 694 (1952).

CHAPTER 5.

Magnetic Properties of β-Cobalt Phthalocyanine

5.1 Introduction

In this chapter, results from the measurement of the magnetization (M) of β-CoPc are presented covering the temperature range of 0.4 K to 300 K and in magnetic fields H up to 90 kOe. The data are analyzed and discussed in terms of Curie-Weiss (CW) law and the Bonner-Fisher (BF) model for a Heisenberg linear chain antiferromagnetim (HLCA) with spin S = 1/2. The intrachain exchange constant J_{ex}/k_B = - 2 K for β-CoPc was reported using DFT (density functional theory) calculation by Wu et al. [1]. Also, in a recent reported magnetic studies of β-CoPc [2], the intrachain exchange constant J_{ex}/k_B = - 1.9 K was determined experimentally from the fit of the magnetization M vs. magnetic field (H) data at 2 K to the predictions of the BF model. However, since the reported χ vs. T data were limited to temperatures T > 8 K, the observation of T_{max} characteristic of an HLCA was not observed in β-CoPc [2]. Thus, in this chapter, the observation of T_{max} at 1.9 K and fits of χ vs. T data and the isothermal M vs. H data at 1 K to the Bonner-Fisher model are the important new results. A major portion of the results presented in this chapter have been published by the author in a recent paper [3].

5.2 Sample and its Structural Characterization

5.2.1 Sample

The powder sample of CoPc used here was purchased from Alfa Aesar (stock # 41496) and used as received. X-ray diffraction (XRD) analysis confirmed this powder sample as β-phase (shown later). An

attempt was made to prepare α-phase CoPc from this β-phase CoPc using the acid pasting method described in literature [4]. However this attempt was not successful. So the results presented here are only for the β-CoPc powder sample.

5.2.2 X-ray Diffraction (XRD)

X-ray diffraction (XRD) analysis of the purchased sample was performed at room temperature using a PANalytical X'Pert Pro X-ray diffractometer with Cu-Kα source (λ = 0.15418 nm). The XRD pattern of the sample shown in Fig. 5.1 agrees with the expected pattern of β-CoPc (ICDD #02-061-3631) with space group $P2_1/c$ and two molecules per unit cell in the monoclinic structure with lattice parameters: a = 1.4542 nm, b = 0.4773 nm, c = 1.9352 nm, and β = 120.82°[5]. This structure is shown in Chapter 1, Fig. 1.1(d). Note that all the observed peaks in the XRD pattern match well with the ICDD pattern for β-CoPc. The lower observed intensity of the (100) peak is likely due to the plate-like preferred orientation of the sample shown below by scanning electron microscopy.
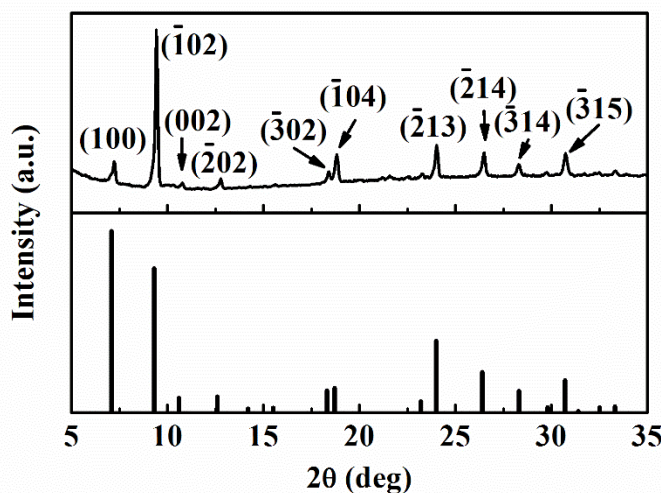
Fig. 5.1 *The top panel shows the XRD pattern of β-CoPc sample with Miller indices of major lines marked; the bottom panel shows the ICDD data of β-CoPc.*

5.2.3 Scanning Electron Microscopy (SEM)

The SEM of the β-CoPc powder sample was done using a JEOL 7600 FE-SEM system at the DOE National Energy Technology Laboratory and it shows the plate-like morphology (Fig. 5.2).
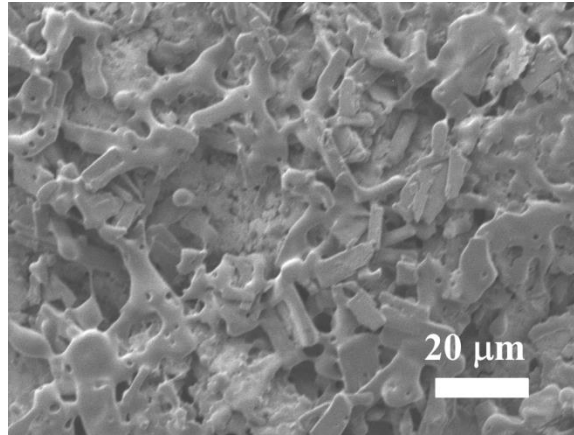
Fig. 5.2 *A Scanning electron micrograph for the β-CoPc powder sample.*

5.3 Results from Magnetic Measurements, Analysis, and Discussion

5.3.1. Temperature Dependence of DC Magnetization and the Curie-Weiss Law

Measurements of the magnetization (M) of the β-CoPc powder sample from 2 K to 300 K and in magnetic fields up to 90 kOe were carried out using the in-house Physical Property Measurements System (PPMS) described in Chapter 3. In addition, the temperature dependence of the magnetization from 0.4 K to 20 K was also measured using the Superconducting Magnet 2 (SCM2) system at the National High Magnetic Field Laboratory (NHMFL) in Tallahassee, Florida.

At the NHMFL, the M vs. T data were obtained using a home-made susceptometer from 0.4 K to 20 K with applied DC field H = 10 kOe, frequency = 331 Hz, and ac field H_{ac} = 3.3 Oe using the SCM2

facility. The ac susceptibility data acquired at the NHMFL was normalized to the DC susceptibility data acquired using the PPMS at a single temperature (20 K). This can be justified because (i) ac susceptibility was found to be frequency independence; and (ii) the temperature dependence is practically identical between the data obtained by the two techniques. In general, if the magnetic relaxation is much faster than the measurement time scale (1 - 10 ms in this case), the ac susceptibility resembles the DC susceptibility, which seems to be the case for β-CoPc at least in the measured temperature range.

The temperature dependence of magnetic susceptibility χ measured with applied H = 10 kOe is shown in Fig. 5.3. Since M vs. H data is quite linear in H up to about 20 kOe even at 2 K (see inset of Fig. 5.3), χ = M/H represents the differential susceptibility. Again, the data acquired at the NHMFL from 0.4 K to 20 K is merged with the data acquired with the PPMS from 2 K to 300 K by normalizing the former with the latter at 20 K. The combined data shows a distinct peak at T_{max} = 1.9 K, which is independent of frequency.
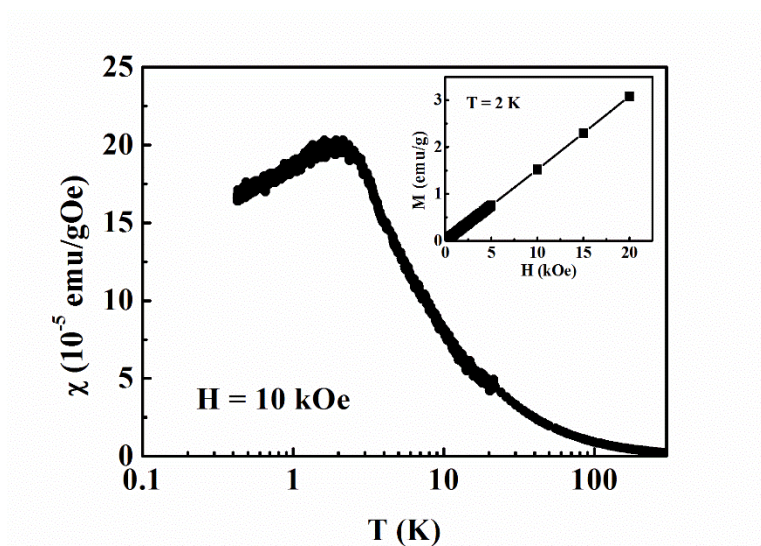
Fig. 5.3 *Magnetic susceptibility χ vs. temperature T of β-CoPc. The inset shows the M vs. H. plot.*
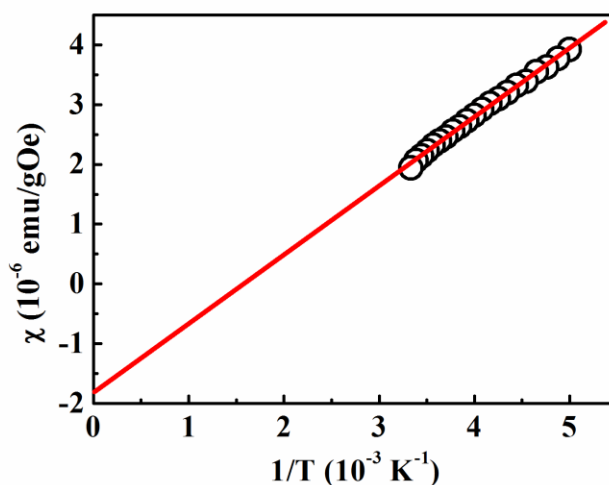
Fig. 5.4 *Plot of magnetic susceptibility χ vs. 1/T for β-CoPc with H = 10 kOe. The solid line is the linear fit of the experimental data and its intercept with y axis (χ) gives $\chi_o = -1.8 \times 10^{-6}$ emu/gOe.*

The analysis of the data was done as follows. First the data acquired from the PPMS from 2 K to 300 K was fitted to the modified Curie-Weiss (CW) law: $\chi = \chi_o + C/(T-\theta)$. For this purpose, $\chi_o = -1.8 \times 10^{-6}$ emu/gOe was determined by plotting χ vs. 1/T and linearly extrapolating the high temperature data to 1/T → 0, as shown in Fig. 5.4. This χ_o includes the diamagnetic contributions of the plastic sample holder and the sample itself. However the effect of χ_o is only noticeable for T > 100 K. Next, by plotting $(\chi - \chi_o)^{-1}$ vs. T (see Fig. 5.5), the linear fit yielded $C = 1.02 \times 10^{-3}$ emu-K/gOe and $\theta = -2.5$ K, the negative θ signifying antiferromagnetic exchange coupling. In Fig. 5.6, the solid line represents the fit to the modified CW law with the magnitudes of χ_o, C, and θ listed above. From Fig. 5.6, it is evident that the data deviates from the CW fit below about 3 K.

73
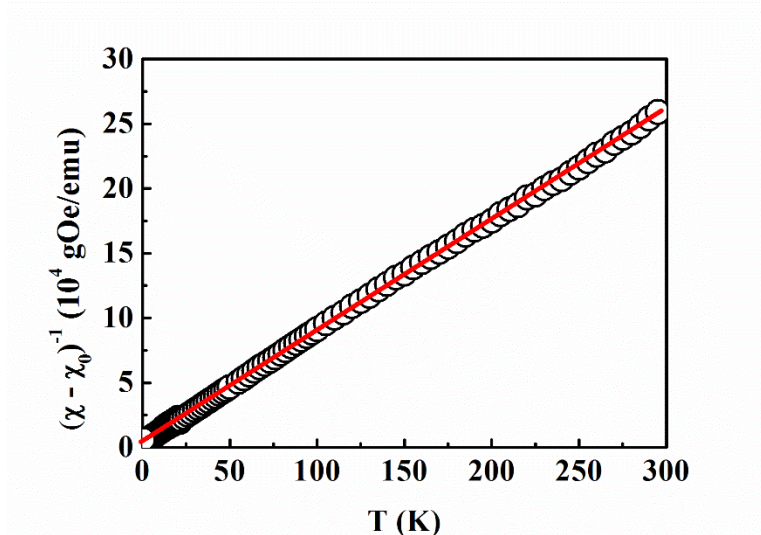
Fig. 5.5 *Plot of the temperature dependence of the inverse magnetic susceptibility $(\chi - \chi_o)^{-1}$ of β-CoPc in H = 10 kOe. The solid line is the linear fit representing CW law.*

Using $C = N\mu^2/3k_B$ where N is the number of magnetic ions per gm, each with magnetic moment μ and k_B is the Boltzmann constant yields $\mu = 2.16$ μ_B per Co^{2+} ion. If the distribution of electrons for the $3d^7$ sate of Co^{2+} obeyed the Hunds' rules, μ close to 4.8 μ_B would have been observed corresponding to spin S = 3/2 (see Table 1.2). Thus the observed $\mu = 2.16$ μ_B per Co^{2+} ion can only be explained if S = 1/2. Using $\mu^2 = g^2 S(S+1)$ yields g = 2.49 for the S = 1/2 low-spin state of Co^{2+} in β-CoPc. Also, g = 2.49 rather than 2.00 implies some contribution from the partially restored orbital moment via spin-orbit coupling as in CuPc. The g-shift is positive since for $3d^7$ state of Co^{2+}, the shell is more than half-full as discussed in Chapter 2.
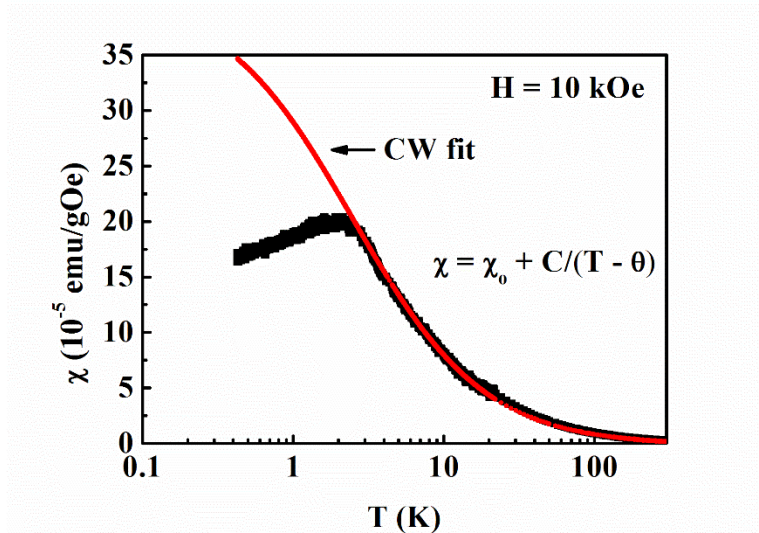
Fig. 5.6 *Magnetic susceptibility χ vs. temperature T of β-CoPc with H = 10 kOe. The Solid line is fit to the modified Curie-Weiss law: χ = χ$_o$ + C/(T-θ) with the parameters: χ$_o$ = - 1.8 × 10^{-6} emu/gOe, C = 1.02 × 10^{-3} emu-K/gOe, and θ = - 2.5 K.*

The Heisenberg exchange constant J_{ex}/k_B can be estimated by the mean-field theory following:

$$J_{ex} = \frac{3\theta}{2ZS(S+1)} \tag{5.1}$$

Here θ is the Weiss constant, S is the spin, and Z is the number of the nearest neighbors of each Co^{2+}. For β-CoPc, Z = 2 (for a linear chain) and spin S = 1/2, yielding :

$$J_{ex} = \theta \tag{5.2}$$

This gives exchange constant J_{ex}/k_B = - 2.5 K using the mean-field theory and it is compared with J_{ex}/k_B obtained from the Bonner-Fisher model discussed below.
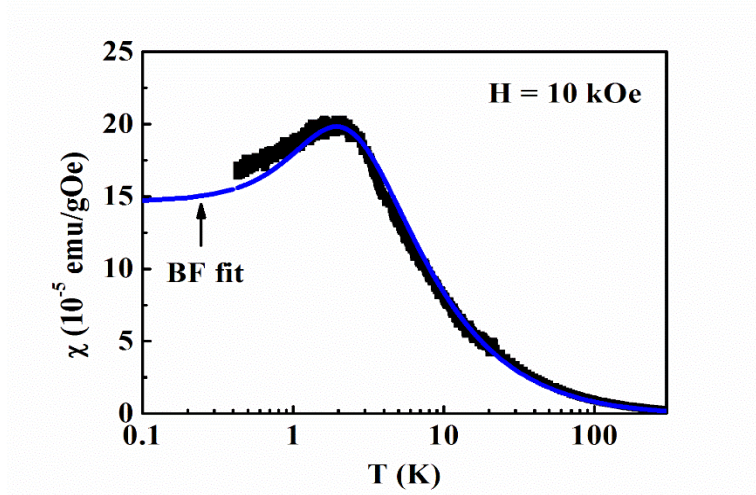
Fig. 5.7 *Magnetic susceptibility χ vs. temperature T plot for β-CoPc. The solid line is fit to the BF model (Eq. 5.3) using $\chi_o = -1.8 \times 10^{-6}$ emu/gOe, $C = 1.02 \times 10^{-3}$ emu-K/gOe, and $J_{ex}/k_B = -1.5$ K.*

5.3.2 Fit to the Bonner-Fisher Model

The data of χ vs. T for the whole temperature range of 0.4 K to 300 K was next fitted to the predictions of the Bonner-Fisher (BF) model [6] for a spin S = 1/2 linear chain with Heisenberg AFM exchange-coupling J_{ex} defined by the Hamiltonian $H = -2J_{ex}\Sigma\ S_i \cdot S_{i+1}$. Following Eggert et al. [7] and Feyerherm et al. [8], the variation of χ vs. T for a linear chain model S = 1/2 system with the normalized AFM coupling parameter $x = |J_{ex}|/(k_B T)$ is given by

$$\chi = \chi_o + \frac{C}{T} F(x) \tag{5.3}$$

$$F(x) = \frac{1 + a_1 x + a_2 x^2}{1 + b_1 x + b_2 x^2 + b_3 x^3} \tag{5.4}$$

Here C is the Curie constant, $x = |J_{ex}|/(k_B T)$ and $a_1 = 0.17032$, $a_2 = 0.93404$, $b_1 = 1.46764$, $b_2 = 0.54784$, and $b_3 = 4.28544$, similar to the analysis presented in Chapter 4 for the CuPc system which also has S = 1/2. With $\chi_o = -1.8 \times 10^{-6}$ emu/gOe and $C = 1.02 \times 10^{-3}$ emu-K/gOe as determined above, the solid line in

76

Fig. 5.7 is the best fit to Eq. (5.3) using $J_{ex}/k_B = -1.5$ K, within uncertainty of 0.1 K in the magnitudes of

J_{ex}/k_B. As for the CuPc case in Chapter 4, the magnitude of J_{ex} was varied till the best fit was obtained in

the whole temperature range. In addition, using the observed $T_{max} = 1.9$ K $= 1.28|J_{ex}|/k_B$ according to the

BF model also yields $|J_{ex}|/k_B = 1.5$ K. Thus the observation of T_{max} and the overall fit of the data to Eq.

(5.3) of the BF model with $J_{ex}/k_B = -1.5$ K provides convincing evidence for the accuracy of this analysis.

This magnitude of J_{ex}/k_B is somewhat smaller than $J_{ex}/k_B = -1.9$ K reported by Serri et al [2] which was

determined from the fit of the M vs. H data at 2 K.

The CW law can be derived from Eq. (5.3) by retaining only the first order term in x. This

exercise leads to the CW law with $\theta = 1.29732 J_{ex}/k_B$. Using $J_{ex}/k_B = -1.5$ K for β-CoPc yields $\theta = -2.0$ K

for β-CoPc, a little smaller than the experimental values of $\theta = -2.5$ K. This disagreement is due to the

fact that at lower temperatures, higher order terms in x become increasingly important particularly for

linear chains and 2-dimensional systems [9].

5.3.3 Magnetic Field Dependence of Magnetization

The data of M vs. H at 1 K and 5 K bracketing $T_{max} = 1.9$ K are shown in Fig. 5.8. The data at 1

K were acquired at the NHMFL, whereas the data at 5 K were taken at West Virginia University using the

PPMS. The expected value of the saturation magnetization $M_S = Ng\mu_B S$ is calculated to be 12.16 emu/g

using g = 2.49 and S = 1/2 which agrees well with the measured value in Fig. 5.8 at T = 1 K where the

magnetization is nearly saturated. The Bonner-Fisher paper on the HLCA [5] does not provide an

analytical expression for M vs. H but provides calculated plots of M vs. H for several $k_B T/|J_{ex}|$ valid for N

= 10 spins in the chain. Using the internet-available software "digitizer", these plots were digitized. This

software allows one to take a scanned image of a plot and digitizes the values off the plot by clicking the mouse on each data point. The data can then be saved and plotted. By following this procedure, we have digitized those plots from the original paper [6] and replotted them. Using $|J_{ex}|/k_BT = 1.5$ K evaluated in this work from the fit of χ vs. T data, the red line (marked as T = 0.9 K) in Fig. 5.8 represents fit to the BF model for the available curve of $k_BT/|J_{ex}| = 0.6$ [5]. Overall, the agreement with the experimental data taken at 1 K is quite satisfactory considering that the BF curves are calculated for N = 10 spins in a chain rather the than for an infinite chain. The agreement is excellent for H < 30 kOe, the region where the BF curves appear to be less sensitive to the magnitude of J_{ex}. This is the region used by Serri et al [2] to fit their data at 2 K to evaluate $|J_{ex}|/k_B = 1.9$ K. Because of this, it is suggested that the smaller magnitude of $|J_{ex}|/k_B = 1.5$ K evaluated here from T_{max} and the fit to the χ vs. T from 0.4 K to 300 K is likely more accurate.
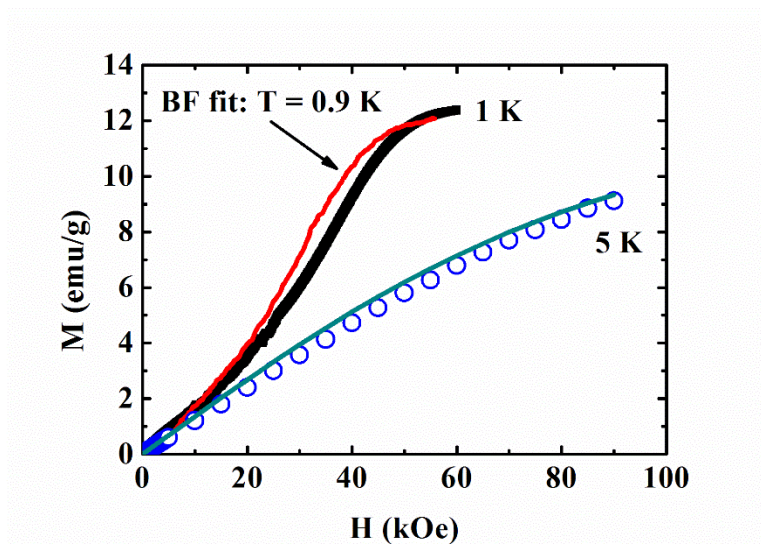
Fig. 5.8 *Magnetization M vs. H data for β-CoPc at 1 K (black solid line) and 5 K (open circles) are compared respectively with the predictions of the Bonner-Fisher model at 0.9 K (red line) [from Ref. 6] and Eq. (5.5) for 5 K (blue line).*

For the M vs. H data at 5 K, fitting the data to the BF model was not possible since the closest calculated available curve to 5 K from Ref. 6 is for $k_B T/|J_{ex}| = 3.0$ which corresponds to T = 4.5 K. Since the fit of the χ vs. T data to the Curie-Weiss law is valid for T > 3 K (Fig. 5.5), we have fitted the M vs. H data at 5 K to the prediction of the molecular-field model which for spin S = 1/2 yields the variation [10]

$$M = M_S \tanh \frac{g\mu_B H}{2k_B(T - \theta)} \tag{5.5}$$

In the above, the CW variation is taken into account by including θ. The fit of the data at 5 K to Eq. (5.5) using the experimental θ = - 2.5 K, g = 2.49 and M_S = 12.16 emu/g, shown as solid line in Fig. 5.8, is quite good.

5.3.4 Temperature Dependence of AC Susceptibilities

The temperature dependence of the ac susceptibilities were carried out for β-CoPc utilizing the in house PPMS. The ac susceptibilities for β-CoPc were measured from 2 K to 20 K with zero dc magnetic field but with a small ac magnetic field H_{ac} = 5 Oe. The frequencies of the ac signals were 725 Hz, 1000 Hz, 3000 Hz, 4000 Hz and 5000 Hz. As shown in Fig. 5.9, there is no frequency dependence for the real part of susceptibility χ'. For the imaginary part of susceptibility χ'', there is a broad peak near 4 K for each measured frequency but without any measurable peak shift, which implies the relaxation process is associated with a much higher characteristic frequency than the measurement frequencies from 725 Hz to 5000 Hz used here for β-CoPc.
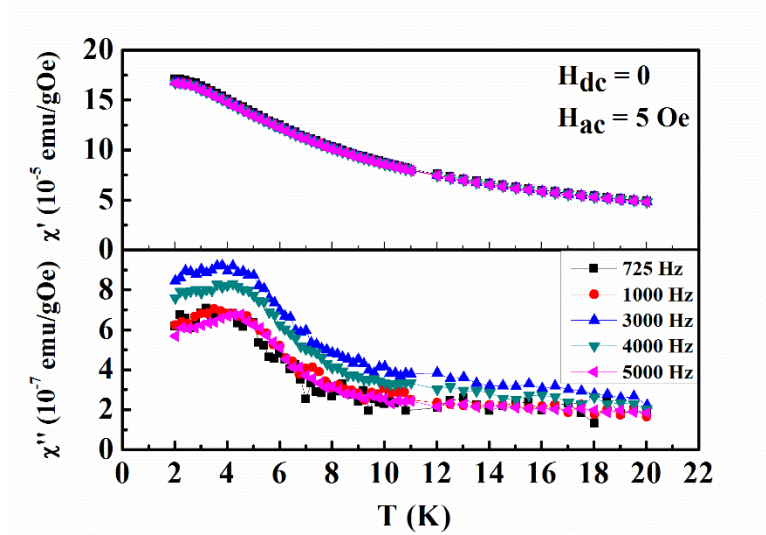
Fig. 5.9 *Frequency dependence of the ac susceptibilities χ' and χ" for β-CoPc measured in zero applied static field with H_{ac} = 5 Oe at several frequencies between 725 Hz and 5000 Hz.*

5.4 Conclusions

The major conclusions from the results presented in this chapter are as follows: (i) The electronic state of Co^{2+} in β-CoPc is shown to have the effective spin S = 1/2 violating Hunds' rules. The resulting distribution of $3d^7$ electrons of Co^{2+} is shown in Fig. 1.6. ; (ii) The fit of the magnetic susceptibility versus temperature data to the Curie-Weiss law yields θ = - 2.5 K, μ = 2.16 $μ_B$, and g = 2.49 for spin S = 1/2 for β-CoPc. The g-shift results from the partially restored contribution of orbital moment via spin-orbit coupling; (iii) The fit of the magnetic susceptibility versus temperature data to the Bonner-Fisher model for linear Heisenberg chains including the observed peak at T_{max} = 1.9 K yields the Heisenberg exchange constant J_{ex}/k_B = - 1.5 K between the Co^{2+}-Co^{2+} ions in β-CoPc; (iv) The isothermal data of M vs. H at 1 K shows good agreement with the Bonner-Fisher model. M vs. H at 5 K data is interpreted by including the effect of the exchange interaction; (v) The results show that β-CoPc is a good example of antiferromagnetically coupled Heisenberg linear chain with spin S = 1/2 of Co^{2+} and magnetic

moment $\mu = 2.16\,\mu_B$. This fit is obtained without invoking any interchain exchange coupling.

References

[1] W. Wu, N.M. Harrison and A.J. Fisher, Phys. Rev. B. **88**, 024426 (2008).

[2] M. Serri, W. Wu, L.R. Fleet, N.W. Harrison, C.F. Hirjibehedin, C.W.M. Kay, A.J. Fisher, G. Aeppi and S. Heutz, Nat. Commun. **5**, 3079 (2014).

[3] Z. Wang, M. Lee, E.S. Choi, J. Poston and M.S. Seehra, J. Magn. Magn. Mater. **407**, 83 (2016).

[4] E.B. Faulkner and R.J. Schwartz, High Performance Pigments, 2nd edition. Wiley-VCH, 2009.

[5] B.N. Figgs, E.S. Kucharski and P.A. Reynolds, J. Am. Chem. Soc. **111**, 1683 (1989).

[6] J.C. Bonner and M.E. Fisher, Phys. Rev. **135**, A640 (1964).

[7] S. Eggert, I. Affleck and M. Takahashi, Phys. Rev. Lett. **73**, 332 (1994).

[8] R. Feyerhem, S. Abens, D. Gunther, T. Ishida, M. Meibner, M. Meschke, T. Nogami and M. Steiner, J. Phys. Condens. Matter. **12**, 8495 (2000).

[9] M.S. Seehra, Phys. Lett. A. **28**, 754 (1969).

[10] V. Narang, D. Korakakis and M.S. Seehra, J. Appl. Phys. **116**, 213911 (2014).

CHAPTER 6.

Magnetic Properties of Vanadyl Phthalocyanine

6.1 Introduction

Based on the Hunds' rules, the electron configuration of the unpaired electron of the $(VO)^{2+}$ ion in VOPc ($C_{32}H_{16}N_8VO$) is expected to be $3d^1$ i.e. a single electron in the 3d shell. According to a recent report [1], the nature of magnetism in VOPc ($C_{32}H_{16}N_8VO$) is simple paramagnetism. This report is in part based on the earlier work of Lever [2] which effectively list its magnetic moment $\mu = 1.73\mu_B$, corresponding to g =2 and S = 1/2 valid for a free electron. However, temperature and magnetic field dependence of the magnetization of VOPc has not been reported so far to verify such a designation. Therefore such measurements covering the temperature range of 0.5 K to 300 K in magnetic fields up to 90 kOe were carried out in this work. Results from these measurements are presented and discussed below.

6.2 Sample and its Structural Characterization

The powder sample of VOPc was purchased from Sigma Aldrich (stock # 791997) and used as received. X-ray diffraction (XRD) of the sample was performed using a PANalytical X'Pert Pro X-ray diffractometer with monochromatic Cu-Kα radiation of wavelength λ = 0.15418 nm. The XRD pattern of the sample is shown in Fig. 6.1 along with the Miller indices of the major Bragg lines. The positions of the Bragg lines were calculated using equations (3.6) through (3.13) of Chapter 3 valid for the triclinic structure and the lattice parameters listed below. It was found that the structure matched perfectly with

that of phase II for VOPc having space group P$\bar{1}$ with two molecules per unit cell of the triclinic

structure and lattice parameters: a = 1.2027 nm, b = 1.2571 nm, c = 0.8690 nm, α = 96.04°, β = 94.80°,

and γ = 68.20° [3]. This structure is shown in Fig. 6.2. In contrast to the other TMPc investigated here,

VOPc is a nonplanar molecule and has a five- coordinate square pyramidal structure with a single electron

associated with VO^{2+} ion [4]. By analyzing X-ray diffraction (XRD) data, Ziolo et al. showed that V atom

is 0.0575 nm above the molecular plane and V-O distance is 0.1580 nm [3].
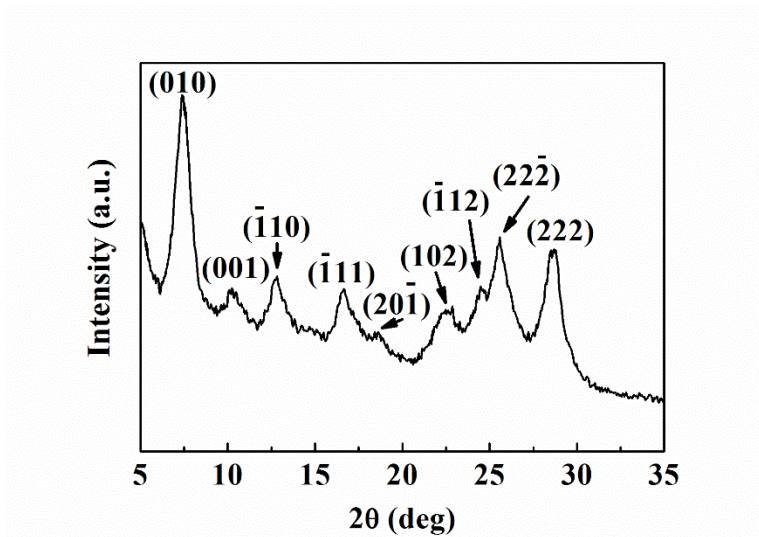
Fig. 6.1 *XRD pattern of VOPc powder sample with Miller Indices of the peaks shown.*
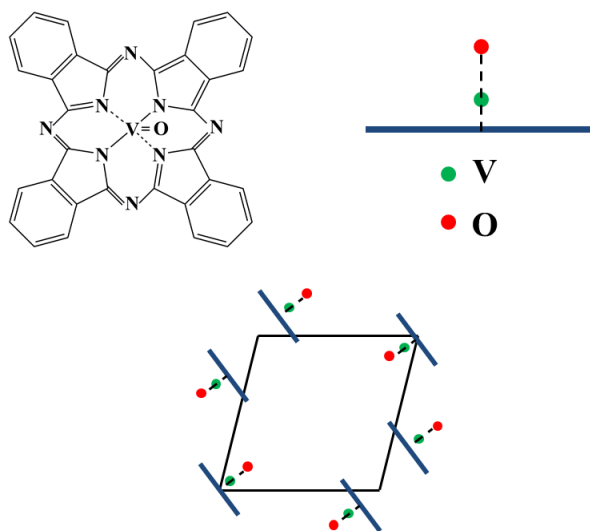
Fig. 6.2 *Molecular structure and unit cell of VOPc (phase II). The lower panel shows a view down the b-axis of the unit cell. The blue lines in the unit cell depict the orientation of the molecular planes of VOPc.*

The scanning electron microscopy of the VOPc powder sample was done using a JEOL 7600 FE-SEM system at the DOE National Energy Technology Laboratory. The SEM micrograph in Fig. 3 shows micron-sized agglomerated particles with some plate-like features of the particles. No additional information was obtainable from this micrograph.
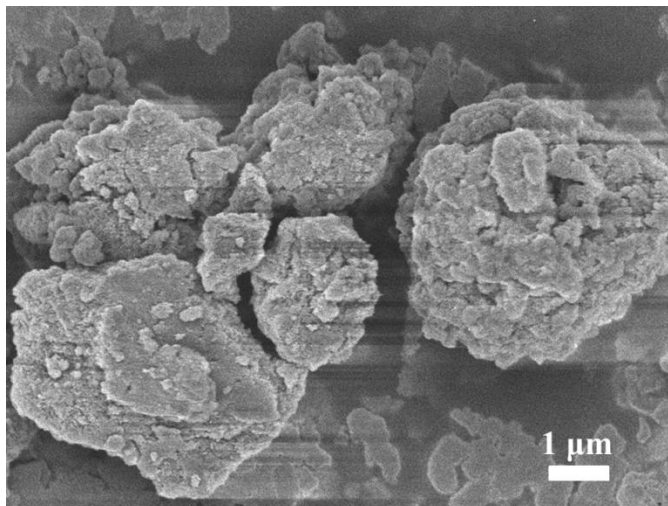
Fig. 6.3 *A Scanning electron micrograph for the VOPc sample. The length of scale bar is 1 μm.*

6.3 Results from Magnetic Measurements, Analysis, and Discussion

6.3.1 Temperature Dependence of DC Magnetization and the Curie-Weiss Law

Measurements of the magnetization M of the VOPc sample as a function of temperature T from 2 K to 300 K and in magnetic field H up to 90 kOe were performed at WVU using the in-house Physical Property Measurement System (PPMS) manufactured by Quantum Design Inc. In addition, performing magnetization measurements at temperatures lower than 2 K was considered quite desirable in this case since such data allows one to determine whether VOPc is a perfect paramagnet or there exists a small exchange coupling between VO^{2+} ions. The magnetization measurements down to 0.5 K in magnetic fields up to 70 kOe were carried out in collaboration with Dr. Li Pi at the High Magnetic Field Laboratory, Chinese Academy of Sciences (CHMFL) in China using a Magnetic Property Measurement System (MPMS) acquired from Quantum Design Inc.

The magnetization measurements performed at the CHMFL are: M vs. T from 0.5 K to 2 K with

H = 1 kOe and M vs. H up to 70 kOe at 0.5 K, 1 K, and 1.5 K. The M vs. T data (from 0.5 K to 2 K) acquired at the CHMFL was normalized to the M vs. T data (from 0.5 K to 300 K) acquired using the in-house PPMS at a single temperature (2 K). Fig 6.4 shows the combined data of the temperature dependence of magnetic susceptibility χ = M/H for VOPc powder sample measured at H = 1 kOe covering the temperature range of 0.5 K to 300 K.

The analysis of the data shown in Fig. 6.4 was done as follows. First the χ vs. T data from 0.5 K to 300 K was fitted to the modified Curie-Weiss (CW) law: $\chi = \chi_o + C/(T - \theta)$. For this purpose, χ_o = - 9.3 $\times 10^{-7}$ emu/gOe was determined by plotting χ vs. 1/T and linearly extrapolating the high temperature data to 1/T $\rightarrow$ 0, as shown in Fig. 6.5. As in the cases of CuPc and CoPc, χ_o contains diamagnetic contributions of both VOPc as well as the plastic sample holder used in the measurements. However χ_o is quite small compared to the measured χ for T < 100 K and so its effects become only noticeable at temperatures T > 100 K.
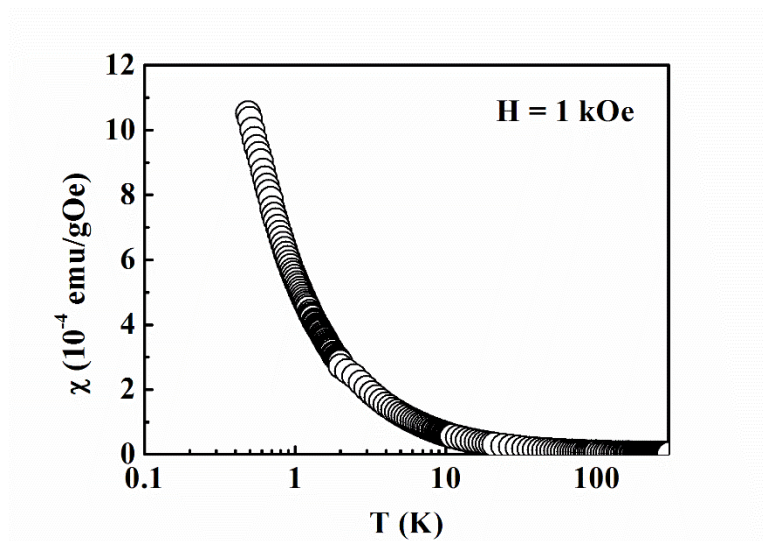
Fig. 6.4 *Magnetic susceptibility χ vs. temperature T of VOPc powder sample.*
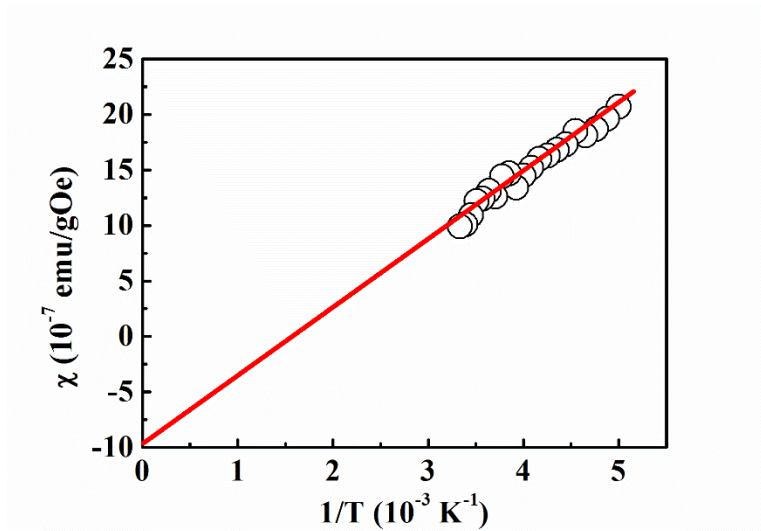
Fig. 6.5 *Plot of magnetic susceptibility χ vs. 1/T for VOPc with H = 1 kOe. The solid line is the linear fit of the experimental data and its intercept with y axis (χ) gives χ_o = - 9.3 × 10^7 emu/gOe.*

After determining χ_o, the data of $(\chi - \chi_o)^{-1}$ was plotted against temperature (Fig. 6.6) yielding a straight line whose slope = 1/C yielded C = 6.266 × 10^{-4} emu-K/gOe. The intercept on the T-axis yields θ = - 0.1 K within the experimental uncertainty, the negative θ signifying antiferromagnetic exchange coupling.
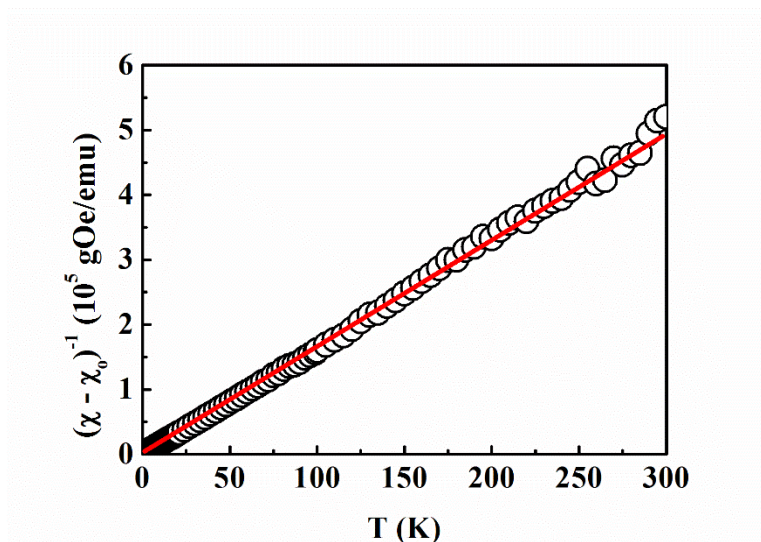
Fig. 6.6 *Plot of temperature dependence of the inverse magnetic susceptibility $(\chi - \chi_o)^{-1}$ of VOPc in H = 1 kOe. The solid line is the linear fit representing CW law.*

The solid lines in Fig. 6.7 are fits to the modified CW law shown for both $\theta = -0.1$ K and $\theta = 0$ K with $\chi_o = -9.3 \times 10^{-7}$ emu/gOe and $C = 6.266 \times 10^{-4}$ emu-K/gOe. It is evident that the choice of $\theta = -0.1$ K provides a better fit to the data especially for T < 2 K. This magnitude of $\theta = -0.1$ K represents a very weak antiferromagnetic exchange coupling between the VO^{2+} ions and the so near-perfect paramagnetic nature of VOPc. In comparison, in the corresponding systems of α-CuPc and β-CuPc [5] and β-CoPc [6], all with S = 1/2, considerably larger magnitudes of $\theta = -2.3$ K, -0.2 K, and -2.5 K respectively were observed. Assuming a linear chain antiferromagnetic system as in α-CuPc and β-CuPc [5] and β-CoPc [6], yields $\theta = 1.29732\ J_{ex}/k_B$ where J_{ex} is the Heisenberg exchange constant in the Hamiltonian $H = -2J_{ex}\Sigma\ S_i \cdot S_{i+1}$ and k_B is the Boltzmann constant. This analysis yields $J_{ex}/k_B = -0.077$ K as the exchange coupling constant in VOPc for $\theta = -0.1$ K. It is evident in Fig. 6.7 that without the χ vs. T measurements reported here for T < 2 K, a case for $\theta = -0.1$ K could not have been made.
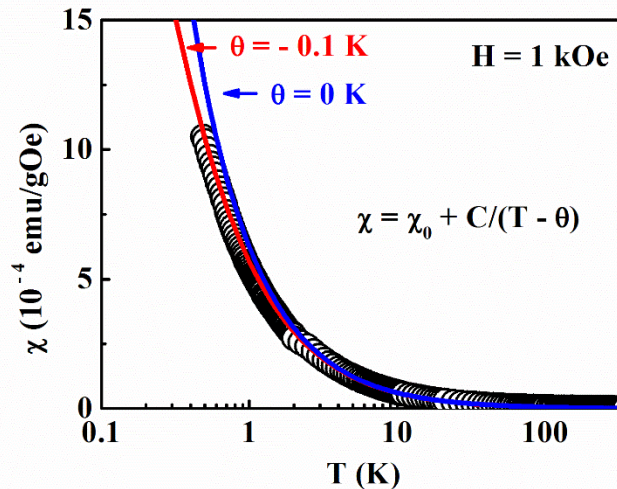
Fig. 6.7 *Magnetic susceptibility χ versus temperature T from 0.5 K to 300 K with H = 1 kOe of VOPc powder sample. The open circles are experimental data and the solid lines are fits to the modified Curie-Weiss law with the parameters: $\chi_o = -9.3 \times 10^{-7}$ emu/gOe, $C = 6.266 \times 10^{-4}$ emu-K/gOe, and $\theta = -0.1$ K and 0 K as shown.*

Using $C = N\mu^2/3k_B$ where N is the number of magnetic ion per gm and μ is the magnetic

moment per ion, the evaluated $C = 6.266 \times 10^{-4}$ emu-K/gOe yields magnetic moment $\mu = 1.704\mu_B$ per

VO^{2+} ion. The molecular weight (MW) = 579.46 g/mol for VOPc is used in these calculations to

determine $N = N_A/MW$ where N_A is the Avogadro's number. This magnitude of $\mu = 1.704\mu_B$ shows the

electronic state of V in VOPc is indeed V^{4+} (electronic configuration: $3d^1$) corresponding to spin S = 1/2

(see table 1.2). For S = 1/2, g = 1.967 is obtained using $\mu^2 = g^2S(S+1)\mu_B^2$. The magnitude of g < 2 due to

orbital contribution is expected for TM ions with d-shell less than half full as is valid for V^{4+} or VO^{2+}.

Electron spin resonance (ESR) is a complementary technique to magnetic measurement to

accurately determine the g-values. Very early brief report by Ingram and Bennet [8] in VOPc reported a

broad absorption with g = 2 with a width of about 500 Oe. Assour et al [9] reported ESR studies in VOPc

diluted (1:1000) in H_2SO_4, H_2Pc and ZnPc yielding $g_\parallel = 1.965$ and $g_\perp = 1.988$ yielding an average g = ($g_\parallel$

+ 2 $g_\perp$)/3 = 1.980. This g-value matches well with g = 1.967 determined here from the magnetic data. To

the best of our knowledge, studies on the temperature dependence of the ESR spectra of undiluted VOPc

have not yet been reported which would provide a better comparison with our magnetic data. At our

suggestion, such ESR measurements are now being undertaken by the research group of Professor Dalal

at Florida State University.

6.3.2 Magnetic Field Dependence of Magnetization

The isothermal data of M vs. H up to 90 kOe measured at 0.5 K, 1 K, 1.5 K, 2 K, 5 K, 10 K, 25

K, 50 K, 100 K, and 300 K for VOPc are shown in Fig. 6.8. To verify the near-perfect paramagnetism of

VOPc, the isothermal data of M vs. H for all temperatures is plotted in terms of M vs. $H/(T − \theta)$ in Fig.

6.9 to check its Brillouin function variation expected for $S = 1/2$ systems given by [7]:

$$M = M_S \tanh \frac{g\mu_B H}{2k_B(T - \theta)} \qquad (6.1)$$
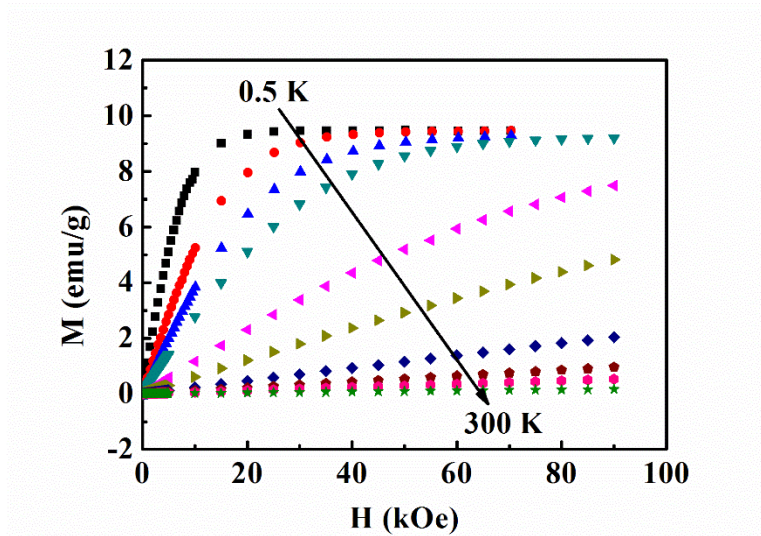
Fig. 6.8 *Magnetization M vs. magnetic field H data for VOPc powder at 0.5 K, 1 K, 1.5 K, 2 K, 5 K, 10 K, 25 K, 50 K, 100 K, and 300 K. Note that the data at 0.5 K, 1 K, and 1.5 K are with H up to 70 kOe; data at other temperatures are with H up to 90 kOe.*
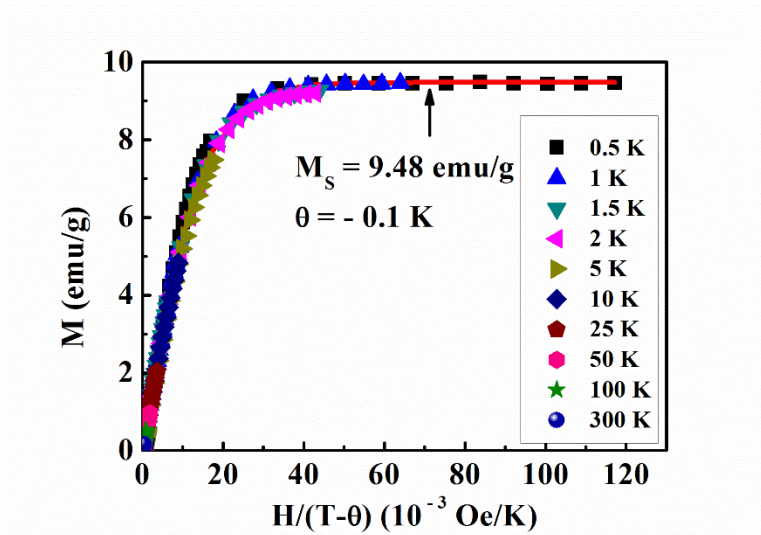
Fig. 6.9 *Plot of magnetization M vs. H/(T - θ) with θ = - 0.1 K for VOPc at 0.5 K, 1 K, 1.5 K, 2 K, 5 K, 10 K, 25 K, 50 K, 100 K, and 300 K. The solid line (red color) is fit to Eq. (6.1) with g = 1.967, M_S = 9.48 emu/g, and θ = - 0.1 K.*

This plot in Fig. 6.9 shows collapsing of all the data on to a single curve which fits Eq. (6.1) very well with θ = - 0.1 K implying the very weak antiferromagnetic exchange coupling between the VO^{2+} ions. Notice that saturation magnetization M_S = 9.46 emu/g at 0.5 K agrees well with the calculated value of M_S = 9.48 emu/g using $M_S = Ng\mu_B S$ with g = 1.967 and S = 1/2. As noted earlier, the molecular weight (MW) = 579.46 g/mol for VOPc is used in these calculations to determine $N = N_A/MW$ where N_A is the Avogadro's number.

6.4 Conclusions

The major conclusions are summarized as following: (i) The electronic state of V in VOPc is shown to be V^{4+} with spin S = 1/2; (ii) The fit of the magnetic susceptibility versus temperature data to the Curie-Weiss law yields θ = - 0.1 K, μ = 1.704 μ_B, and g = 1.967 for spin S = 1/2 for VOPc. θ = - 0.1 K indicates a very weak antiferromagnetic exchange coupling between VO^{2+} ions which implies the near-perfect paramagnetism of VOPc. (iii) The negative g-shift from the free electron value is expected for shells less than half full as is valid for the $3d^1$ configuration of VO^{2+} ions and it results from the partial contribution of the orbital moment via spin-orbit coupling. This is different from the expected positive g-shift reported here for Cu^{2+} and Co^{2+} ions in CuPc and CoPc systems with the electronic configurations of $3d^9$ and $3d^7$ respectively with 3d-shells more than half full; (iv) The collapsing of all the data of M vs. H to a single curve which fits Eq. (6.1) very well with θ = - 0.1 K in terms of the plot of M vs. H/(T - θ) also confirms near perfect paramagnetism in VOPc with very weak exchange coupling between VO^{2+} ions. The experimental magnitude of saturation magnetization M_S = 9.46 emu/g at 0.5 K agrees very well with the calculated magnitude assuming complete alignment of the spins; (v) Measurements of the magnetic

91

susceptibility versus temperature down to 0.5 K and M vs. H measurements at 0.5 K in VOPc were crucial in determining the accurate magnitudes of $\mu = 1.704\,\mu_B$, $g = 1.967$ and $\theta = -0.1$ K in this system.

References

[1] K. Eguchi, T. Takagi, T. Nakagawa and T. Yokoyama, J. Chem. Phys. C. **118**, 17633 (2014).

[2] A.B.P. Lever, J. Chem. Soc. 1861 (1965).

[3] R.F. Ziolo, C.H. Griffiths and J.M. Troup, J. Chem. Soc., Dalton Trans. **11**, 2300 (1980).

[4] H. Adler, M. Paszkiewicz, J. Uihlein, M. Polek, R. Ovsyannikov, T.V. Basova, T. Chasse and H. Peisert, J. Phys. Chem. C. **119**, 8755 (2015).

[5] Z. Wang, K.L. Pisane and M.S. Seehra, IEEE. Trans. Mag. **51**, 2700104 (2015).

[6] Z. Wang, M. Lee, E.S. Choi, J. Poston and M.S. Seehra, J. Magn. Magn. Mater. **407**, 83 (2016).

[7] V. Narang, D. Korakakis and M.S. Seehra, J. Appl. Phys. **116**, 213911 (2014).

[8] D.G.E. Ingram and J. E. Bennett, J. Chem. Phys. **22**, 1136 (1954).

[9] J. M. Assour, J. Goldmacher and S.E. Harrison, J. Chem. Phys. **43**, 159 (1965).

CHAPTER 7.

Magnetic Properties of β – Nickel Phthalocyanine

7.1 Introduction

The nature of magnetism in β-NiPc has been reported to be diamagnetism with the unusual low spin state S = 0 for Ni^{2+} $(3d^8)$ [1-4] as shown in Fig. 1.5 (chapter 1). However, detailed temperature and magnetic field dependence of the magnetization were not provided in these reports. In this chapter, results from the measurement of the magnetization (M) of a β-NiPc sample from 2 K to 300 K and in magnetic fields H up to 90 kOe are reported, analyzed and discussed.
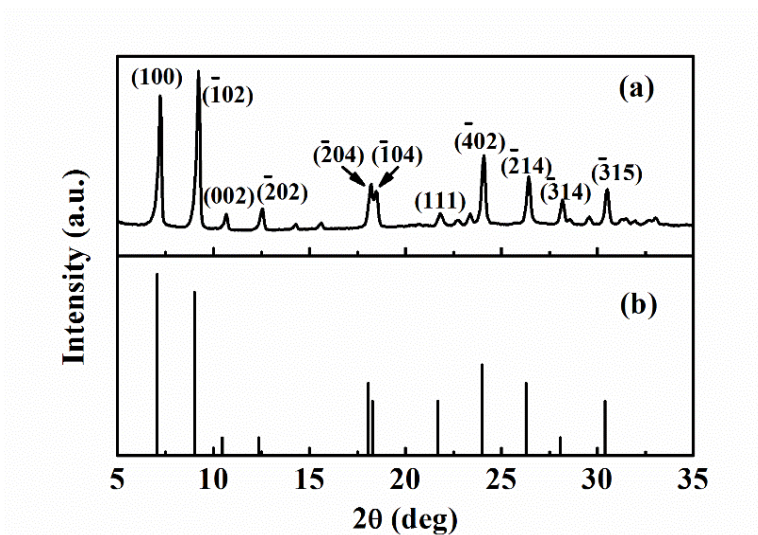
Fig. 7.1 The top panel shows the measured XRD pattern of β-NiPc sample with Miller indices of major lines marked; the bottom panel shows the expected line positions and intensities according to the ICDD data base of β-NiPc.

7.2 Sample and its Structural Characterization

The powder sample of NiPc used here was purchased from Alfa Aesar (stock # 39453) and used

as received. Fig. 7.1 shows the X-ray diffraction (XRD) of the sample measured at room temperature.

This pattern agrees with the expected pattern of β-NiPc (ICDD #00-011-0744) with space group P2$_1$/c and

two molecules per unit cell in the monoclinic structure with lattice parameters: a = 1.49 nm, b = 0.47 nm,

c = 1.99 nm, and β = 121.15°. This structure was shown in Fig. 1.1 of Chapter 1. Note that all the

observed peaks in the XRD pattern match well with the ICDD pattern for β-NiPc.
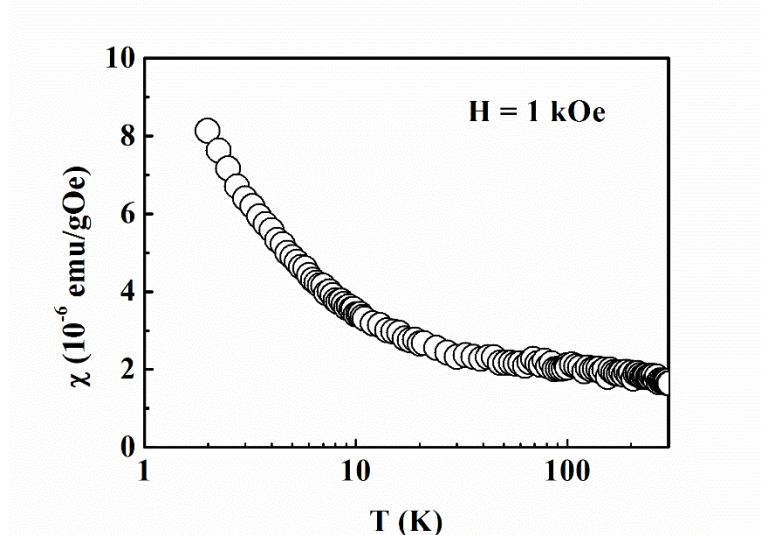
Fig. 7.2 *Magnetic susceptibility χ of β-NiPc vs. temperature T with H = 1 kOe.*

7.3 Results from Magnetic Measurements, Analysis, and Discussion

7.3.1. Temperature Dependence of DC Magnetization

The temperature dependence of the magnetic susceptibility χ = M/H of the sample measured

with H = 1 kOe is shown in Fig. 7.2. This temperature dependence is similar to that of a paramagnet

although the measured magnetic susceptibility is about two orders of magnitude smaller than that

observed in other TMPc samples. For example, χ at 2 K is of the order of 10^{-6} emu/gOe for β-NiPc

compared to 10^{-4} emu/gOe for the CuPc samples at 2 K. Since β-NiPc should be diamagnetic because of

the spin S = 0 state, the χ vs. T data indicates the possible presence of a paramagnetic or ferromagnetic

impurity (e.g. Fe) in the sample. Since the presence of an impurity was not observed in the XRD pattern,

the magnitude of this impurity has to be smaller than about 3 %, the lower detection limit of XRD.

Therefore additional magnetic measurements were undertaken to try to determine the nature of this

impurity. These additional measurements and their discussion and analysis are presented below.
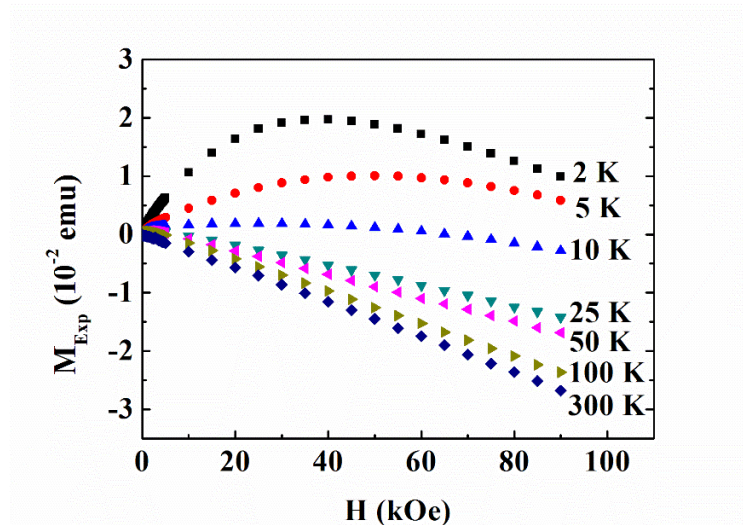
Fig. 7.3 *Magnetization M vs. field H at temperatures indicated for β-NiPc plus the sample holder.*

7.3.2 Magnetic Field Dependence of Magnetization

The isothermal data of M vs. H up to 90 kOe measured at 2 K, 5 K, 10 K, 25 K, 50 K, 100 K,

and 300 K for the β-NiPc powder sample are shown in Fig. 7.3. At the higher temperatures of 25 K to 300

K, the M vs. H variation is characteristic of a diamagnetic material with diamagnetic susceptibility

decreasing with decrease in temperature. However from the data at the lower temperatures, it is evident

that some ferromagnetic impurity must exist in the sample because of the visible rise of magnetization

with increasing H at 2 K, 5 K, and 10 K. Also, it is noted that the measured magnetization is a

combination from both β-NiPc and the sample holder. The sample holder is made of plastic and should be diamagnetic.

In order to obtain the data just from β-NiPc without any contribution from the sample holder, M vs. H measurements at 2 K, 5 K, 10 K, 25 K, 50 K, 100 K, and 300 K for just the sample holder were performed and the data are shown in Fig. 7.4. The fact that the data at each temperature almost follows the same slope (magnetic susceptibility χ) is understandable because the magnetic susceptibility χ should be independent of magnetic field and temperature for diamagnetic materials. Next, the magnetization M data for just β-NiPc at various temperatures were obtained (shown in Fig. 7.5) by subtracting the measured magnetization of the sample holder shown in Fig. 7.4 from the measured magnetization of NiPc plus sample holder shown in Fig. 7.3. The resulting magnetic field dependence of the magnetization of NiPc at different temperatures, now normalized by the mass of NiPc, is shown in Fig. 7.5.
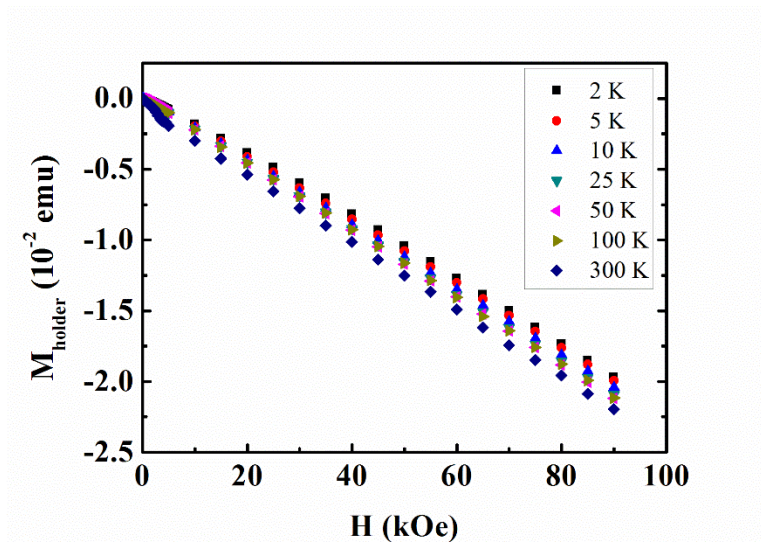
Fig. 7.4 Magnetization M vs. field H at several temperatures for just the sample holder.
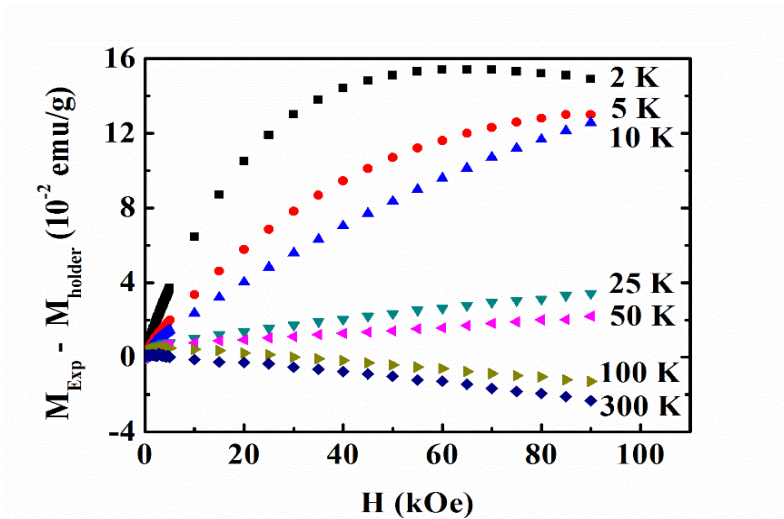
Fig. 7.5 *The magnetization M vs. field H data just for β-NiPc at temperatures shown on the plot.*

The magnetization data of β-NiPc shown in Fig. 7.5 clearly has a ferromagnetic component(M_{FM}) superposed on the diamagnetic component (M_D) with the M_{FM} essentially absent from the data at 300 K. Therefore, the data were analyzed by using the following Eq.:

$$M_{sample} = M_D + M_{FM} = \chi_D H + M_{FM} \tag{7.1}$$

Here χ_D is the diamagnetic susceptibility of pure β-NiPc and should be the same at all temperatures and M_{FM} is magnetization of the impurity. The linear fit of the data for M vs. H at 300 K yields the slope $\chi_D = -3.38 \times 10^{-7}$ emu/gOe (shown in Fig. 7.6). Then the ferromagnetic component M_{FM} for each measured temperature can be determined by:

$$M_{FM} = M_{sample} - \chi_D H \tag{7.2}$$

The magnetic field dependence of M_{FM} was then determined at different temperatures and this temperature dependence of M_{FM} and M_D is shown in Fig.7.7. Assuming M_D to be temperature

97

independent as expected from theory, M_{FM} increases with decrease in temperature.
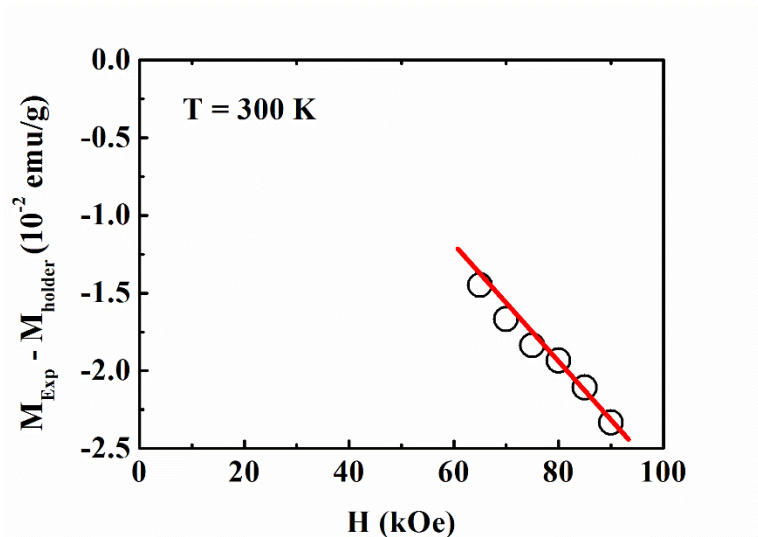
Fig. 7.6 *Plot of magnetization M vs. H for β-NiPc sample at T = 300 K. The solid line is the linear fit of the experimental data for higher H and the slope gives χ_D = - 3.38 × 10^{-7} emu/gOe.*
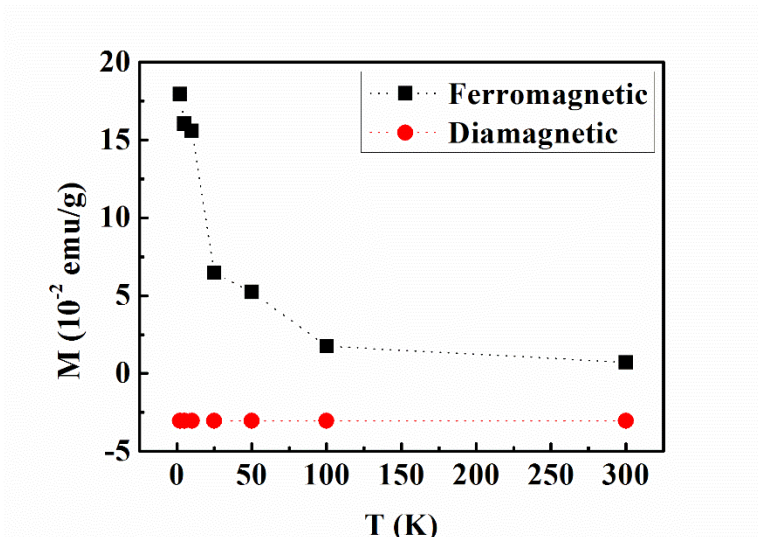
Fig. 7.7 *Temperature dependence of the ferromagnetic component M_{FM} and diamagnetic component M_D for β-NiPc. The dotted lines connecting the data points are visual guides.*

To verify the ferromagnetic character of the impurity, hysteresis loop measurements between + 90 kOe and − 90 kOe were carried out at 2 K, 5 K, 10 K, 25 K, 50 K, 100 K, and 300 K for the β-NiPc

sample. Fig. 7.8 shows the hysteresis loop at 2 K yielding the coercivity H_C = 250 Oe. Similar hysteresis loops and coercivity were observed at 5 K, 10 K, 25, 50 K, and 100 K. The hysteresis data at 300 K was very noisy and not shown here. Fig. 7.9 shows the plot of coercivity H_C vs. temperature T at various temperatures from 2 K to 100 K.

Although the ferromagnetic nature of the magnetic impurity is quite evident from these measurements, it is not possible to identify the chemical phase of the impurity. Therefore attempts were made to detect the magnetic impurity using x-ray photoelectron spectroscopy (XPS) of the sample. XPS was performed using a PHI 5000 VersaProbe XPS with Al-Kα source (hν = 1486.7 eV). The survey scan was performed for β-NiPc powder sample from binding energy ranging from 0 eV to 1000 eV. This range covers all the core levels for the elements N, C, Ni, Fe, Mn, and Co. XPS analysis indicates the impurity is Fe but with very small concentration (atomic concentration less than 0.2 %). However, it was difficult to exactly quantify the concentration because of the weakness of the impurity line. Since Fe oxidizes easily, it is likely that the impurity is really an oxide of iron such as ferrimagnetic magnetite (Fe_3O_4) or maghemite (γ-Fe_2O_3).
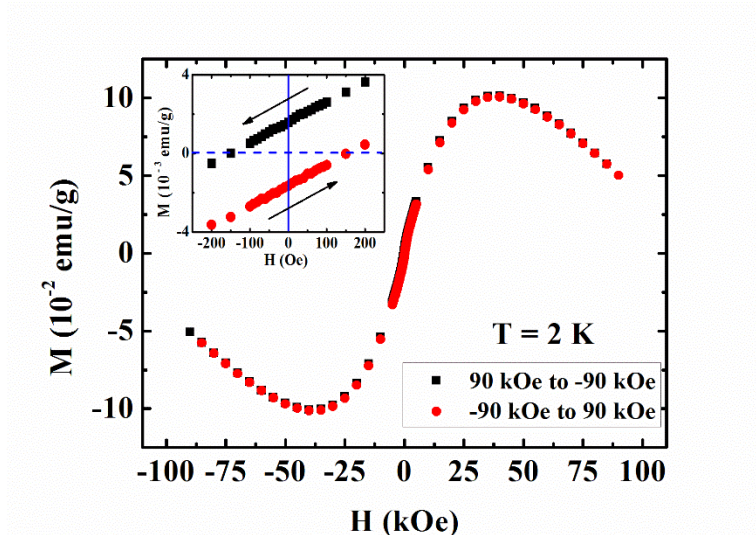
Fig. 7.8 *Hysteresis loop measured between + 90 kOe to – 90 kOe at 2 K for β-NiPc. The inset is the zoom of the low-field region of the hysteresis loop at 2 K.*
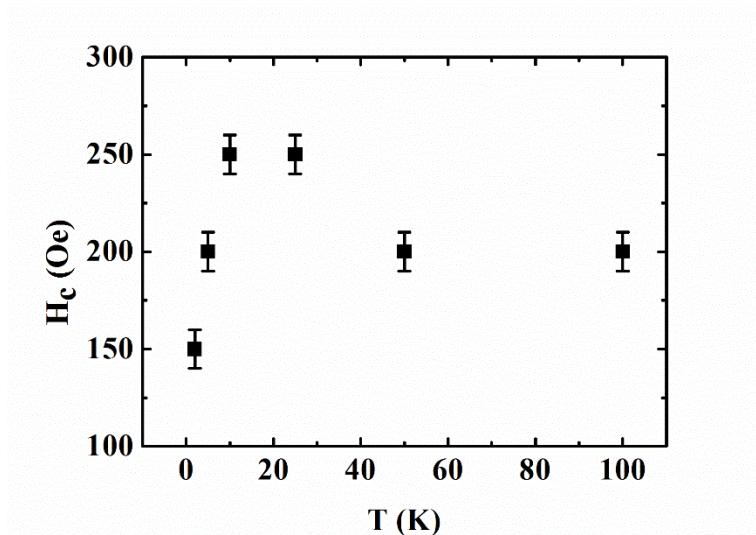
Fig. 7.9 *Coercivity HC vs. temperature T at 2 K, 5 K, 10 K, 25 K, 50 K, and 100 K for β-NiPc.*

7.4 Conclusions

The major conclusions from the results presented in this chapter are as follows: (i) The diamagnetic nature of β-NiPc was confirmed by detailed magnetization measurements and analysis, and the diamagnetic susceptibility χ_D = - 3.38 $\times 10^{-7}$ emu/gOe is obtained. This is in agreement with the room

temperature measurements of χ_D reported for pure β-NiPc, H_2Pc and ZnPc[2]; (2) The ferromagnetic component in the commercial sample of β-NiPc is due to Fe impurity with a concentration of less than 0.2%. However it is highly unlikely that the impurity is Fe metal because Fe gets easily oxidized to its oxides. This concentration is too small to be detected in the standard x-ray diffraction experiments; (3) A procedure is developed to separate the magnetic contributions of pure NiPc from that of the ferromagnetic impurity. However the exact chemical nature of the impurity could not be determined from the techniques employed here.

References

[1] A.B.P. Lever, J. Chem. Soc. 1821 (1965).

[2] C.G. Barraclough, R.L. Martin and S. Mitra, J. Chem. Phys. **55**, 1426 (1970).

[3] N. Marom and L. Kronik, Appl. Phys. A. **95**, 159 (2009).

[4] Z. Hu, B. Li, A. Zhao, J. Yang and J. Hou, J. Phys. Chem. C. **112**, 13650 (2008).

CHAPTER 8.

Magnetic Properties of β- Manganese Phthalocyanine

8.1 Introduction

In this chapter, detailed measurements and analysis of the temperature (2 K to 300 K) and magnetic field (up to 90 kOe) dependence of the dc and ac magnetic susceptibilities in a powder sample of β-MnPc are presented. Previous magnetic studies in β-MnPc have reported it to be a canted ferromagnet below $T_C \approx 8.6$ K [1-7]. However, the recent result of the lack of a λ-type anomaly in the specific heat vs. temperature data near the quoted T_C has questioned the presence of long-range 3-dimensional (3D) magnetic ordering in this system [8, 9]. Therefore, more detailed magnetic measurements and analysis was undertaken to determine the nature of magnetism and magnetic ordering in this system. Our magnetic measurements and analysis presented in this chapter leads to the conclusion that 3D long-range magnetic ordering is absent in β-MnPc. This is supported by the Arrott plots and the lack of a peak in the ac susceptibilities, χ' and χ'', near the quoted T_C. Instead, the system can be best described as an Ising-like chain magnet with Arrhenius relaxation of the magnetization governed by an intra-layer ferromagnetic exchange constant $J_{ex}/k_B = 2.6$ K and the single ion anisotropy energy parameter $|D|/k_B = 8.3$ K. The absence of 3D long range order is consistent with our result of the measured $|D| > J_{ex}$ [10]. A major portion of the results presented in this chapter have been published by the author in a recent paper [11].

8.2 Sample and its Structural Characterization

The powder sample of MnPc was purchased from Sigma Aldrich (stock # 379557) and used as received. The x-ray diffraction (XRD) pattern of the sample performed using a PANAnalytical X'Pert Pro X-ray diffractmeter (Cu-Kα radiation, λ = 0.15148 nm) is shown in Fig. 8.1. The XRD pattern matches perfectly with that expected pattern for β-MnPc (ICDD #02-063-3894) having space group $P2_1/c$ and two molecules per unit cell in the monoclinic structure with lattice parameters: a = 1.4576 nm, b = 0.4755 nm, c = 1.9362 nm and β = 120.7 °. This structure is shown in Fig. 8.2. It is important to note that the pattern given in the ICDD card for β-MnPc is based on calculations and single crystal XRD data of Mason et al [12]. In the previous studies reported on β-MnPc [2-10] XRD patterns of the powder samples of β-MnPc were not reported to the best of our knowledge. The other relevant information from Fig. 8.2 is the distance b = 0.4755 nm between the Mn ions in a chain and the stack angle δ = 45 ° representing orientation of the molecular planes with respect to the b-axis. The Mn^{2+}-Mn^{2+} exchange coupling may result from both superexchange coupling through N atoms as well as direct exchange coupling. However why the overall Mn^{2+}-Mn^{2+} exchange coupling in β-MnPc is ferromagnetic is not yet well understood [13-15].
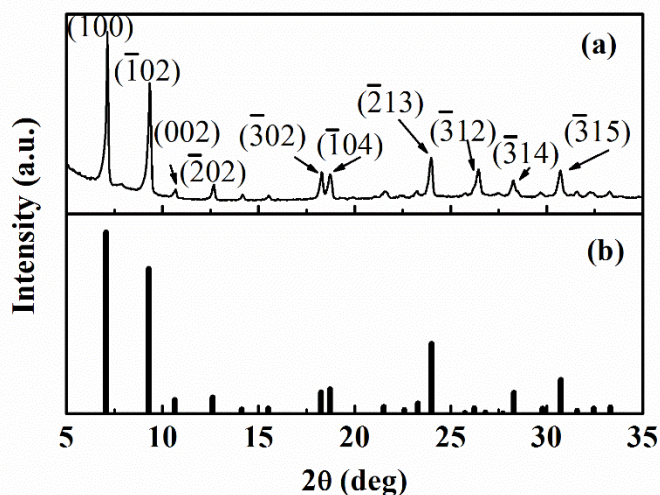
Fig. 8.1 *(a) XRD pattern of the MnPc powder sample with Miller indices of major lines shown. The stick diagram in (b) shows the relative intensities of the lines according to the ICDD card (#02-063-3894) for β-MnPc.*

By measuring the width w of the major Bragg lines, the data was fit to the Williamson-Hall equation: $w \cos\theta = (0.9\lambda / D) + \eta \sin\theta$ where D is the crystallite size and η is the strain. The straight line fit (Fig. 8.3) yielded D = 75(15) nm for the crystallite size and $\eta = 9(2) \times 10^{-3}$ for the strain. The morphology of particles of β-MnPc was examined by scanning electron microscopy (SEM) utilizing a JEOL7600 FE-SEM system at the DOE National Energy Technology Laboratory. The SEM micrograph of Fig. 8.4 shows plate-like morphology of the β-MnPc sample with 2 to 3 μm sides and 50-100 nm thickness, the latter agreeing with the crystallite size of D = 75 (15) nm determined from the analysis of the XRD data discussed above.
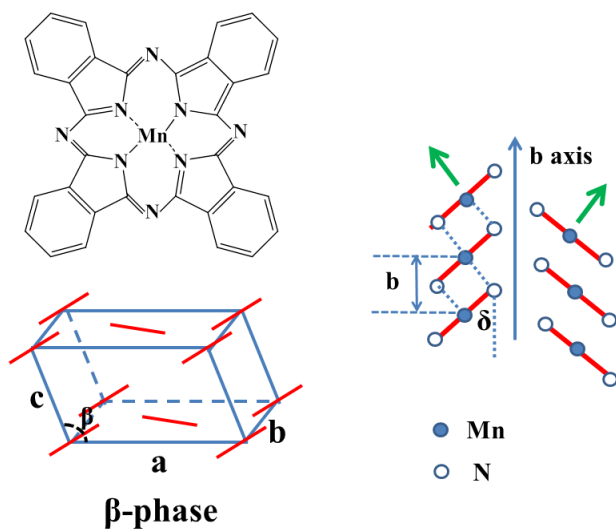
Fig. 8.2 *Molecular model, unit cell, and molecular arrangement of β-MnPc. The red lines in the unit cell depict the orientation of the molecular planes of β-MnPc. The green arrows show the direction of magnetic moment perpendicular to the molecular plane, the discussion on which is given in the text.*
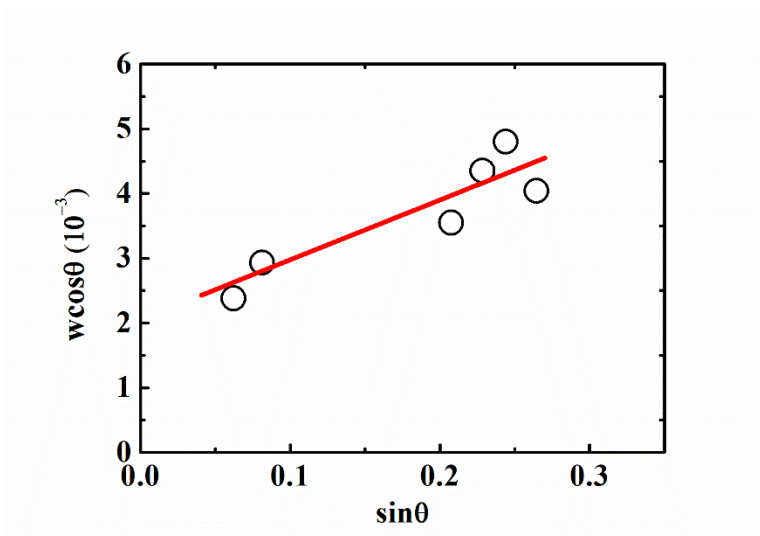
Fig. 8.3 *The plot of w cosθ versus sinθ using prominent Bragg lines of β-MnPc to fit the Williamson-Hall equation: w cosθ = (0.9λ / D) + η sinθ.*
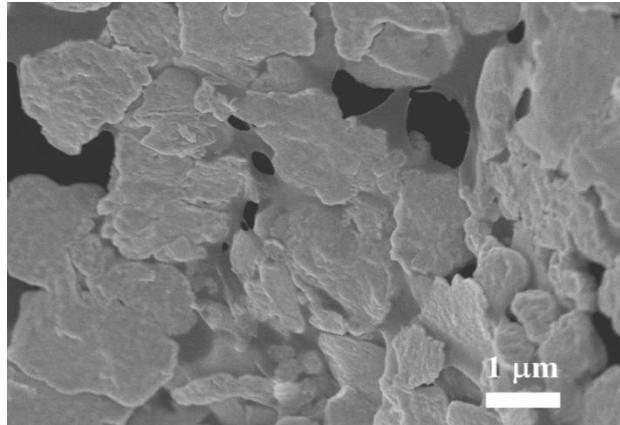
Fig. 8.4 *A scanning electron micrograph for β-MnPc. The length of scale bar is 1 μm.*

8.3 Results from Magnetic Measurements, Analysis, and Discussion

8.3.1. Temperature Dependence of DC Magnetization and the Curie-Weiss Law

The temperature dependence of the magnetic susceptibility χ = M/H measured in applied magnetic fields H = 50 Oe, 200 Oe and 1 kOe is shown in Fig. 8.5. A log-plot is used along the temperature axis to highlight the data at the lower temperatures. In the inset of Fig. 8.5, plot of (dχ/dT) versus T for the H = 1 kOe data is shown yielding a peak near 9 K. Similar analysis was used in earlier papers by several authors to infer a ferromagnetic $T_C \approx 8.6$ K [1-7].
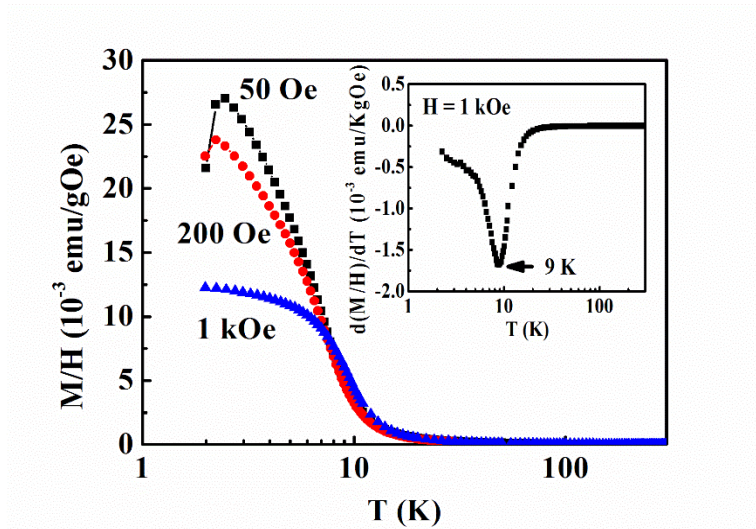
Fig. 8.5 *Magnetic susceptibility χ = M/H vs. temperature for β-MnPc. The inset is the plot of dχ/dT versus T data for the H = 1 kOe data showing a peak at 9 K.*

The analysis of the data was done in a step-wise procedure as follows. First the data of χ vs. T from 2 K to 300 K was fitted to the modified Curie-Weiss (CW) law: $\chi = \chi_o + C/(T-\theta)$. For this purpose, $\chi_o = -4.83 \times 10^{-6}$ emu/gOe was determined by plotting χ vs. 1/T and linearly extrapolating the high temperature data to $1/T \to 0$, as shown in Fig. 8.6. This χ_o includes the diamagnetic contributions of the plastic sample holder and the sample itself. Next, by plotting $(\chi - \chi_o)^{-1}$ vs. T (see inset of Fig. 8.7), the linear fit yielded $C = 4.40 \times 10^{-3}$ emu-K/gOe and $\theta = 12.3$ K, the positive θ signifying ferromagnetic exchange coupling. Note that both β-CuPc and β-CoPc show antiferromagnetic exchange coupling between transition-metal ions whereas β-MnPc shows ferromagnetic exchange coupling although they have the similar crystal structure. In Fig. 8.7, the solid line A represents the fit to the modified CW law with the magnitudes of χ_o, C, and θ listed above. From Fig. 8.7, it is evident that the data of χ vs. T deviates strongly from the CW fit below about 15 K.
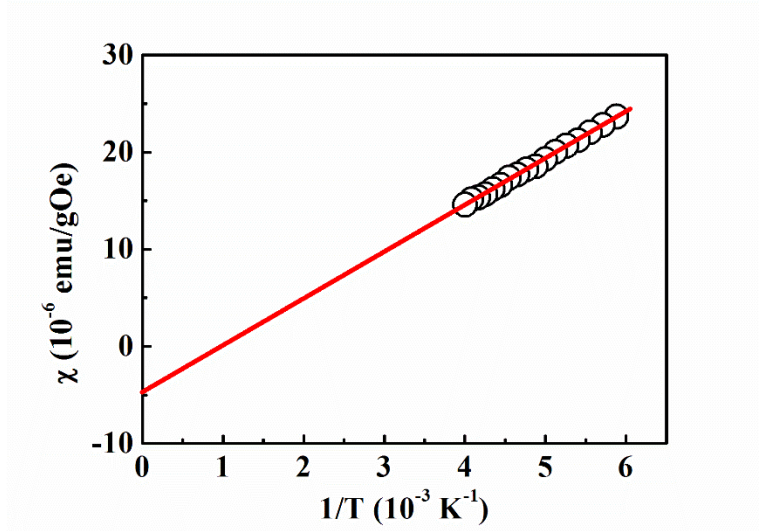
Fig. 8.6 *Plot of magnetic susceptibility χ vs. 1/T for β-CoPc with H = 50 Oe. The solid line is the linear fit of the experimental data and its interception with y axis (χ) gives χ_o = - 4.83 × 10^{-6} emu/gOe.*
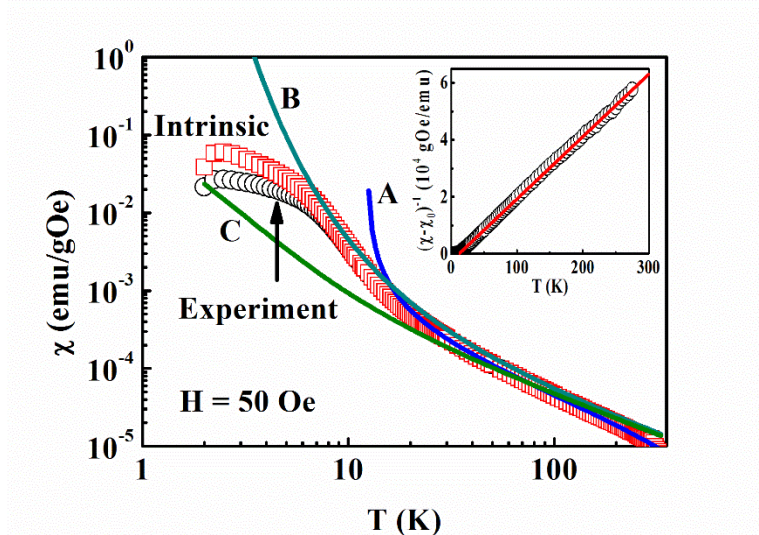
Fig. 8.7 *Magnetic susceptibility χ vs. T with H = 50 Oe for β-MnPc where the "intrinsic" represents data corrected for demagnetizing factors. Solid line A and the inset are fits to the modified Curie-Weiss law with χ_o = - 4.83 × 10^{-6} emu/gOe, C = 4.40 × 10^{-3} emu-K/gOe, and θ = 12.3 K. Solid line B (C) is fit to the Ising (Heisenberg) linear chain model with exchange constant J_{ex}/k_B = 2.6 K.*

Next $C = N\mu^2/3k_B$ where $N = N_A/MW$ is the number of Mn^{2+} ions per gm, N_A is the Avogadro's number and MW = 567.46 g/mol is the molecular weight of β-MnPc, was used yielding μ = 4.467 μ_B as

108

the magnetic moment per Mn^{2+} ion. Also using $\mu^2 = g^2 S(S+1)$ yields g = 2.307 for S = 3/2. If Mn^{2+} in

β-MnPc were in the usual high spin state with S = 5/2, then μ = 5.916 μ_B would have been observed with

g = 2. Note that g = 2.307 is different from the free electron value of 2.00 because of the contribution

from the partially restored orbital moment via spin-orbit coupling as in CuPc and CoPc systems.   The

g-shift is positive since for the $3d^5$ state of Mn^{2+}, the shell is more than half-full as discussed in Chapter II.

The magnitude of μ = 4.467 μ_B is in good agreement with the earlier data of Ref. 1 to 5. The electronic

configuration of the ground state is likely $[(d_{XZ,YZ})^3(d_{XY})^1(d_Z^2)^1]$ or $[(d_{XZ, YZ})^2(d_{XY})^2(d_Z^2)^1]$ as suggested by

Brumboiu et al. [16].

8.3.2. Temperature Dependence of DC Magnetization, Heisenberg Linear Chain, and Ising Linear Chain Analysis

The positive θ = 12.3 K suggests ferromagnetic coupling between Mn^{2+} ions as also noted by

earlier investigators [1-9]. Since χ vs. T in Fig. 8.7 does not fit the CW law below about 15 K, we

attempted fits of the data to the predictions of both the Heisenberg linear chain following our analysis in

β-CoPc [17] and in α-CuPc and β-CuPc using the BF model [18,19] and the Ising linear chain model [8, 9,

20]. The magnetic susceptibility in both cases follows the Eq. (8.1):

$$\chi = \frac{C}{T} \cdot \frac{(1 - \Gamma)}{(1 + \Gamma)} \tag{8.1}$$

However $\Gamma = \coth(y) - (1/y)$ for the Heisenberg linear chains and $\Gamma = \tanh(y)$ for the   Ising linear chains.

Here $y = 2J_{ex}S^2/(k_BT)$ with J_{ex} being the exchange constant in the Heisenberg Hamiltonian $H = -2J_{ex}\Sigma \, \mathbf{S_i} \cdot$

S$_{i+1}$. For the Ising linear chain, Eq. (8.1) reduces to:

$$\chi = \frac{C}{T}\exp(4J_{ex}S^2/k_BT) \qquad (8.2)$$

The fit shown by curve B in Fig. 8.7 represents Eq. (8.2) with C = 4.40 × 10^{-3} emu-K/gOe (determined earlier from the CW fit above 15 K) and J$_{ex}$/k$_B$ = 2.6 K determined from the fit. Curve B fits the data well down to about 6 K and represents a major improvement over the CW fit. The data points marked "intrinsic" represent the corrected intrinsic susceptibility $\chi_g(i) = \chi_g/(1 - 4\pi\rho\chi_g)$ where χ_g is the measured gram susceptibility and ρ = 1.61g/cm^3 is the density of β-MnPc. It is noted that $\chi_g(i)$ takes into account the demagnetization factor of 4π valid for a thin plate with H perpendicular to the plate. Although $\chi_g(i) > \chi_g$ for T < 6 K, it is still less than the magnitude expected for χ from Eq. (8.2) for T < 6 K. As shown by curve C, the data does not fit the predictions of Heisenberg linear chain very well unlike the case for β-CuPc with AFM exchange interaction [19]. The difference between these cases likely result from the larger anisotropy in β-MnPc as reflected in the larger value of g = 2.307 compared to g = 2.10 in β-CuPc [19].

According to Eq. (8.2), a plot of ln(χT/C) against 1/T should yield a straight line. This plot is shown in Fig. 7.8 showing a near linear variation for T > 6 K with the slope = 4S^{2}J$_{ex}$/k$_B$ yielding J$_{ex}$/k$_B$ = 2.6(0.2) K. The deviations from Eq. (8.2) observed in Figs. 7.7 and 7.8 for T < 6 K likely result from the fact that the normalized magnetic correlation length ξ/a = χT/2C (a = cell parameter of the chain) remains finite for the Ising model in the limit T = 0 K [20] because of the energy gap Δ/k$_B$ = 65.5 K determined later. This energy gap leads to the formation of domains separated by sharp domain walls, thus keeping

correlation length finite in the limit T = 0 K [20]. From the plot in Fig. 8.8, near 6 K the normalized

correlation length $\approx e^3/2 \approx 10$, defining the size of the domains along the chain length. A second possible

reason for the departure of the data from the prediction of the Ising model is that our measurements are on

a powder sample and hence the measured χ contains both the parallel and perpendicular susceptibilities,

the latter remaining finite for the Ising model even in the limit of T = 0 K [4, 21].
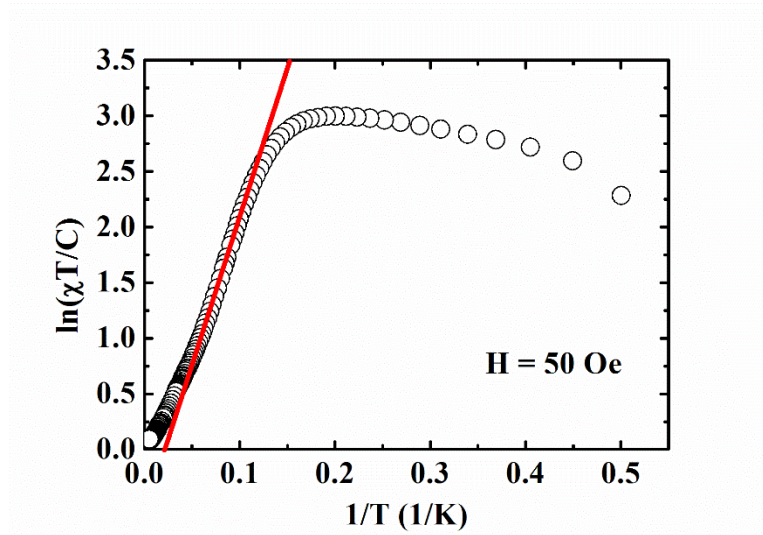
Fig. 8.8 *ln(χT/C) vs. 1/T for β-MnPc. The solid line is the linear fit to Eq. (8.2) with J_{ex}/k_B = 2.6 K.*

8.3.3. Magnetic Field Dependence of Magnetization and Ising Linear Chain Analysis

The magnetic field dependence of the magnetization at 2 K was next fit to the prediction of the

Ising linear chain model. The normalized magnetic field dependence of the magnetization M measured at

2 K for the powder sample of β-MnPc is shown as curve C in Fig. 8.9 using M_S = 31 emu/g determined in

the limit of 1/H $\rightarrow$0 (see inset of Fig. 8.9). The magnetization does not quite saturate even at 90 kOe.

The hysteresis loop of β-MnPc was measured at 2 K between H = + 90 kOe and − 90 kOe with the zoom

of the low-field region shown in the other inset of Fig. 8.9. There is practically no hysteresis within the

experimental uncertainty of about 20 Oe for setting the field to zero. The absence of hysteresis is

consistent with the absence of a long-range ferromagnetic ordering.
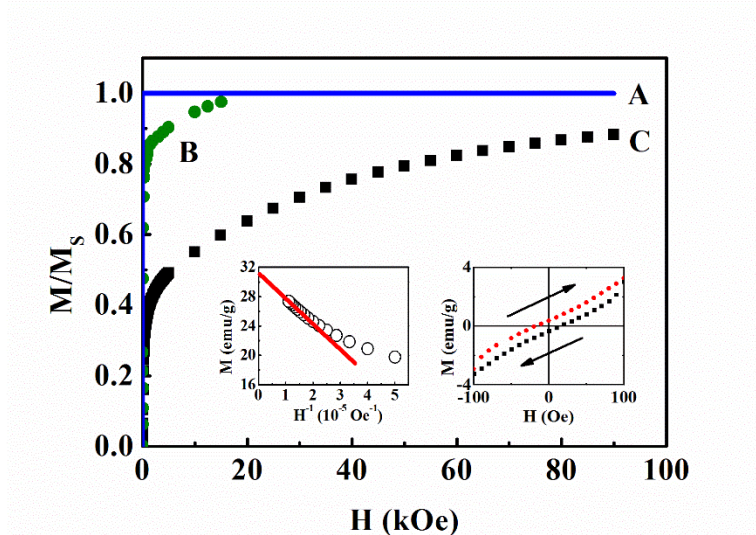
Fig. 8.9 *Solid line A is the calculated curve using Eq. (8.3). Curve C represent our experimental data taken at 2 K on the powder sample of β-MnPc and normalized to $M_S = 31$ emu/g determined in the limit $1/H \rightarrow 0$ (left inset). Data represented by curve B is the experimental data of M vs. H at 4.2 K for single crystal of β-MnPc along the easy axis and taken from the paper by Mitra et al. [5].The right inset is the zoom of the low-field region of the hysteresis loop.*

The M vs H variation for Ising-linear chain magnet is predicted to follow the equation

[20]:

$$\frac{M}{M_S} = \frac{\sinh(\mu H/k_B T)}{\sqrt{\sinh^2(\mu H/k_B T) + \exp(-8J_{ex}S^2/k_B T)}} \tag{8.3}$$

The solid line A shown in Fig. 8.9 is the calculated curve using Eq. (8.3) for T = 2 K and μ = 4.467 μ_B,

J_{ex}/k_B = 2.6 K and S = 3/2 evaluated earlier for β-MnPc. This curve saturates at very low magnetic fields

unlike our experimental data for the powder sample of β-MnPc. The data shown in curve B is the

experimental data taken from the paper by Mitra et al [5] which was measured at 4.2 K in single crystal of

β-MnPc with H up to 15 kOe applied along the easy axis; it reaches near-saturation at around 3 kOe closer to the predicted variation of Eq. (8.3). Note that the data in curve B was reproduced from the original paper [5] using the internet-available software "digitizer". This software allows one to take a scanned image of a plot and digitize values off the plot by clicking the mouse on each data point. The data was then saved and replotted. Both curves B and C show rapid rise in M at very low H followed by a gradual increase at the higher H. For the powder sample, the lack of rapid saturation even up to 90 kOe is likely due to the contributions from the afore-mentioned perpendicular susceptibility [4, 21]. The domains canted relative to the b-axis [5, 7] are the likely reason for this slow rate of saturation of the magnetization. This domain structure taken from the paper by Awaga et al. [6] is shown in Fig. 8.10.
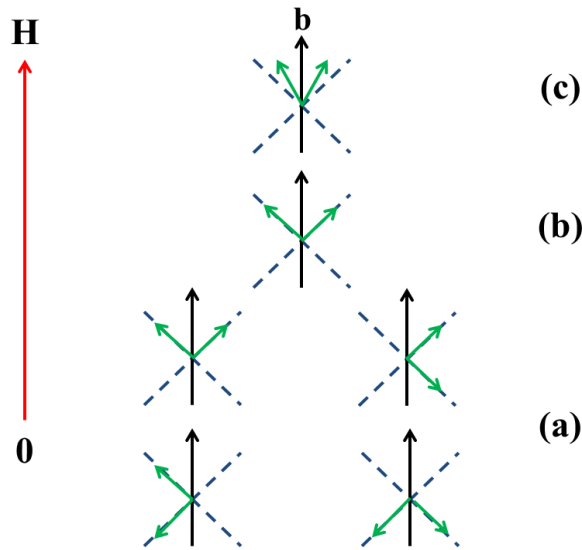
Fig. 8.10 Domain structure in β-MnPc reproduced from the paper by Awaga et al. [6]. The applied magnetic field is along the b-axis (black arrow), the two green arrows show the moments on the neighboring chains. (a) Four kinds of magnetic domains at zero field. (b) Single domain under the magnetic field. (c) Rotation of the magnetic moments toward the magnetic field.
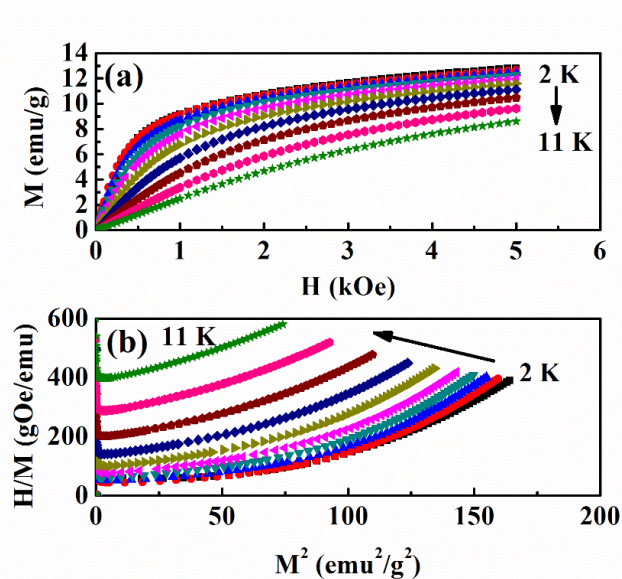
Fig. 8.11 *(a) Magnetization M vs. magnetic field H for β-MnPc measured in 1 K intervals between 2 K and 11 K; (b) Data of (a) plotted as H/M vs. M^2.*

8.3.4 Arrott Plots

According to the Landau theory of phase transitions [22], near T_C the magnetization M in a magnetic field H should follow the equation: $MH = a(T–T_C)M^2 + bM^4$ where a and b temperature-independent constants. This equation can be rearranged as:

$$\frac{H}{M} = bM^2 + a(T - T_C) \qquad (8.4)$$

Therefore, plots of H/M vs. M^2 at different temperatures bracketing the expected T_C should have a positive or negative intercept depending on whether $T > T_C$ or $T < T_C$. At $T = T_C$, the plot should go through the origin. These are called the Arrott plots and they present a way of accurately locating the T_C of a ferromagnet [23-25]. For this purpose, M vs. H was measured for H up to 5 kOe at one-degree temperature interval between 2 K and 11 K bracketing the presumed T_C near 9 K and the data are shown in Fig. 8.11 (a). The Arrott plots resulting from this data are shown in Fig. 8.11 (b). None of the plots intersect the M^2 axis at any temperature ruling out traditional T_C. However, using a linear extrapolation

from the higher M^2 values to zero, a case can be made for $T_C \approx 9$ K as done in the earlier paper by Miyoshi et al [3-4]. However, validity of such extrapolation is questionable in view of the data presented in Fig. 8.11.

8.3.5 Temperature Dependence of Specific Heat

A case against 3D ordering in β-MnPc with a ferromagnetic T_C can also be made from the published data of the temperature dependence of heat capacity C by Taguchi et al [8-9]. Again, using the web-accessed software "Digitizer", this data was digitized and it is re-plotted in Fig. 8.12. There is no λ-type anomaly in the C vs. T; instead there is a broad peak with the center at around 12 K. This result also rules out the traditional long-range 3D order in β-MnPc since in case of a second order transitions, a λ-type peak in the C vs T. data should be observed [26]. It is also noted that in the neutron diffraction studies of β-MnPc carried out 5 K by Figgis et al [27], "no clear evidence for any magnetic contribution to the Bragg intensities" could by convincingly found.
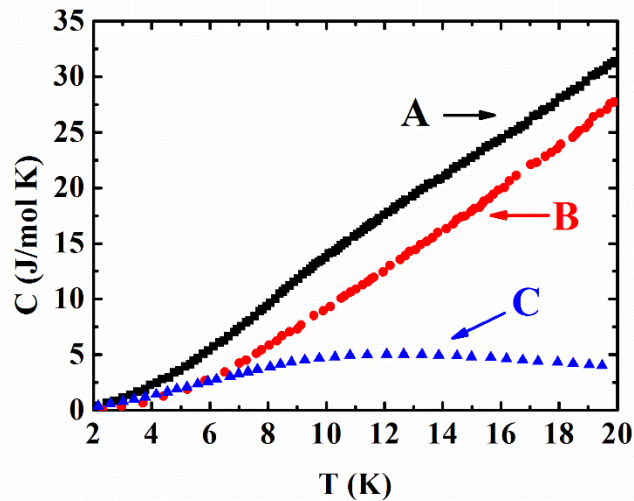
Fig. 8.12 *Temperature dependence of total heat capacity (A), estimated lattice contribution (B), and magnetic contribution to the heat capacity (C) of pristine β-MnPc. The lattice contribution to the heat capacity was estimated from that of β-NiPc in which Ni^{2+} has non-magnetic configuration.*

8.3.6 Temperature and Frequency Dependence of AC Susceptibilities

The temperature dependence of ac susceptibilities, χ' and χ'', of β-MnPc was measured at six different frequencies namely f_m = 10, 50, 100, 500, 1000, and 5000 Hz using H_{ac} = 5 Oe and H_{dc} = 0 Oe. The results in Fig. 8.13 clearly show a peak in χ'' near 3 K which shifts to higher temperatures with increase in f_m. The temperature dependence of χ' is such that the expected relation $\chi'' \sim \partial(\chi'T)/\partial T$ is satisfied [28, 29]. Importantly there is no peak in either χ' or χ'' in the 8 K to 10 K range where earlier studies [1-7] had reported the location of T_C from dc susceptibilities using analysis similar to that shown in the inset of Fig. 7.5. These results combined with a lack of λ-type anomaly in the specific heat provide convincing proof that the long-range 3D ordering is not present in β-MnPc. We also measured the effect of non-zero H_{dc} on χ' and χ''. The results for one frequency comparing the data for H_{dc} = 0 Oe with that for H_{dc} = 200 Oe are shown in Fig. 8.14. The log-plot is used for χ'' to show measurable values of χ'' beginning around 14 K. However, the effect of non-zero dc fields is to shift the peak in χ'' near 3 K only slightly to a lower temperature.
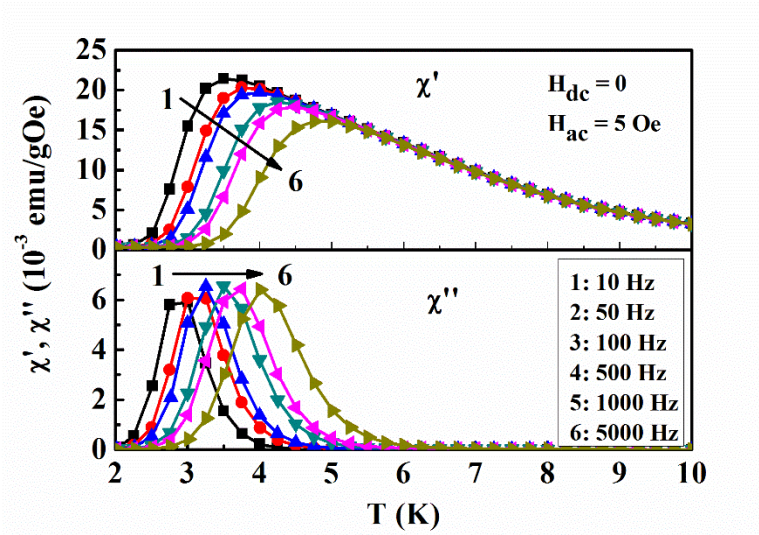
Fig. 8.13 *Frequency dependence of the ac susceptibilities χ' and χ'' for β-MnPc measured in zero applied static field with H_{ac} = 5 Oe at several frequencies between 10 Hz and 5000 Hz.*
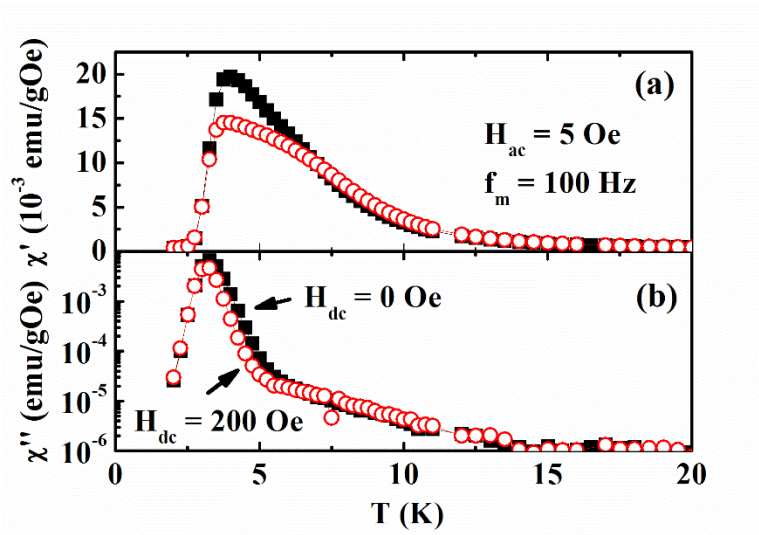
Fig. 8.14 *Temperature dependence of the ac susceptibilities χ' and χ'' for β-MnPc in H_{dc} = 0 Oe (a) and H_{dc} = 200 Oe (b) with H_{ac} =5 Oe at frequency of 100 Hz.*

The shift in the peak position of χ'' to higher temperatures with increase in f_m is similar to the observations in magnetic nanoparticles [28-31] where the peak in χ'' defines the blocking temperature T_B given by:

$$T_B = T_o + \frac{\Delta}{k_B \ln(f_o/f_m)} \qquad (8.5)$$

Here Δ is the anisotropy energy defining the barrier to flipping of the magnetization, f_o is the characteristic attempt frequency of the system and T_o represents the strength of the interparticle interaction (IPI). Another parameter that defines IPI is the parameter Φ defined by [31]

$$\Phi = \frac{\delta T_B}{T_B \delta(\log_{10} f_m)} \qquad (8.6)$$

In Eq. (8.6), δT_B represents change in T_B with change $\delta(\log_{10} f_m)$ in the measurement frequency f_m. Usually $\Phi > 0.13$ implies that IPI is negligible and hence $T_o = 0$. For the result shown in Fig. 8.13 for β-MnPc, $\Phi = 0.14$ is determined signifying negligible IPI and $T_o = 0$. This value $\Phi = 0.14$ rules out the possibility of spin-glass like ordering proposed by Taguchi et al. [8, 9] since for spin glasses $\Phi < 0.05$ [31].

To determine Δ and f_o for our system, $1/T_B$ was plotted against $\ln f_m$ with the slope yielding Δ/k_B and intercept yielding f_o. The results of the changes in T_B with $\ln f_m$ are plotted in Fig. 8.15 with the solid lines fit to Eq. (8.5) with $T_o = 0$, $f_o = 5.9 \times 10^{10}$ Hz and $\Delta/k_B = 65.5$ K. Taguchi et al. [8] also reported ac data on β-MnPc similar to our data shown in Fig. 8.13; however, they did not carry out any analysis of the data. I re-plotted the ac data of Ref. 8 using the software "Digitizer"; our analysis of that data is also shown in Fig. 8.15 yielding identical magnitude of f_o but slightly larger $\Delta/k_B = 69.4$ K .

The physical interpretation of the results from the analysis of χ' and χ'' presented above in β-MnPc is considered next. In the χ vs. T data of Fig. 8.7, the data was fitted to Eq. (8.2) valid for Ising chain magnet. According to Glauber's theory for one-dimensional Ising chain, the relaxation rate $f = 1/\tau$

follows the Eq. (8.7) [20, 32, 33]

$$f = f_o \exp(-\Delta/k_B T) \tag{8.7}$$

In Eq. (8.7), $\Delta = (8J_{ex} + |D|)S^2$ with J_{ex} being the exchange interaction, $|D|$ is the single ion anisotropy and

f_o is the characteristic frequency of the system. As the temperature is varied, then at a certain temperature

T_B, f becomes equal to the measuring frequency f_m yielding

$$T_B = \frac{\Delta}{k_B \ln(f_o/f_m)} \tag{8.8}$$

Eq. (8.8) is equivalent to Eq. (8.5) with $T_o = 0$.
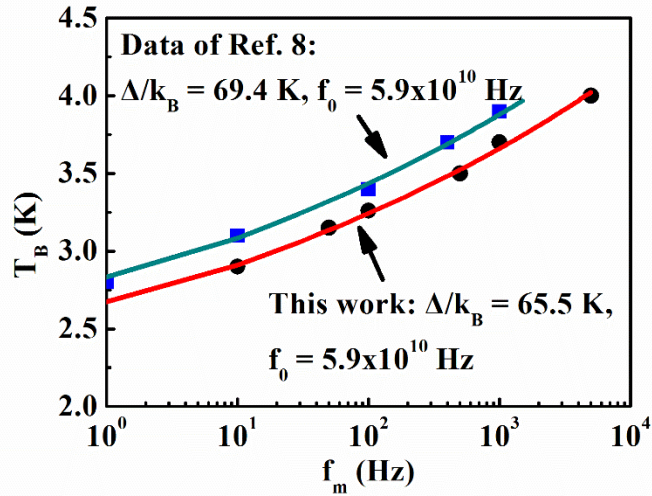
Fig. 8.15 *Plot of the blocking temperature T_B vs. fm with the solid curves fits to Eq. (8.8) with the parameters of the fits shown. The closed circles and squares are data points.*

Using the the fits of the data in Fig. 8.15, $\Delta/k_B = 65.5$ K is determined. Substituting $J_{ex}/k_B = 2.6$

K determined earlier (Fig. 8.7) in $\Delta = (8J_{ex} + |D|)S^2$ yields $|D|/k_B = 8.3$ K as the magnitude of single ion

anisotropy. This magnitude of $|D|/k_B = 8.3$ K is considerably smaller than the theoretical estimate of $|D|/k_B$

= 58 K given in Ref. 1. However, $|D|/k_B = 8.3$ K is still considerably larger than the magnitude of exchange constant $J_{ex}/k_B = 2.6$ K. This is important because theoretically Moriya [10] has shown that for $|D|/J > 1$, long range order is not possible and T_C goes to zero. These results of the determination of $|D|/k_B = 8.3$ K and $J_{ex}/k_B = 2.6$ K and establishing $|D| > J$ are important contributions of this work since they explain all the other experimental observations such as lack of λ-type anomaly, canting of the moments of the neighboring chains relative to the b-axis and absence of coercively at 2 K. It is noted that using $\Delta/k_B = 69.4$ K determined from the fit of ac data of Taguchi et al. [8] in Fig. 7.15 yields slightly larger $|D|/k_B = 10$ K. However all the above arguments are still valid as long as D is larger than J_{ex}.

8.3.7 Cole-Cole Analysis

The data of Fig. 8.13 showing plots of $\chi''(\omega)$ and $\chi'(\omega)$ vs. temperature measured at different frequencies are next anlyzed in terms of the Cole-Cole analysis [34]. The Cole-Cole equations for the complext susceptibility $\chi(\omega) = \chi'(\omega) - i\chi''(\omega)$ at a single temperature are given by [34]:

$$\chi'(\omega) = \chi_S + \frac{(\chi_0 - \chi_S)[1 + (\omega\tau)^{1-\alpha}\sin(\alpha\pi/2)]}{1 + 2(\omega\tau)^{1-\alpha}\sin(\alpha\pi/2) + (\omega\tau)^{2(1-\alpha)}} \tag{8.9}$$

$$\chi''(\omega) = \frac{(\chi_0 - \chi_S)(\omega\tau)^{1-\alpha}\cos(\alpha\pi/2)]}{1 + 2(\omega\tau)^{1-\alpha}\sin(\alpha\pi/2) + (\omega\tau)^{2(1-\alpha)}} \tag{8.10}$$

Here χ_0 (χ_S) is the isothermal (adiabatic) susceptibility in the limit of lowest (highest) frequency, τ is the relaxation time at the frequency $f = \omega/2\pi$ and α is a measure of the distribution of relaxation times. For $\alpha = 0$, Eqs. (8.9) and (8.10) reduce to equations characteristic of a single relaxation time (Debye process). For $\alpha = 1$, $\chi''(\omega) = 0$ and $\chi'(\omega) = (\chi_0 + \chi_S)/2$. For spin-glasses with a wide distribution of relaxation times, α approaching 0.9 may be observed [35]. The Cole-Cole analysis involves plotting $\chi''(\omega)$ vs. $\chi'(\omega)$

at a fixed temperature and fitting it to the following equation derived from Eq. (8.9) and (8.10) [36]:

$$\chi''(\chi') = -\frac{\chi_0 - \chi_S}{2\tan[(1-\alpha)\pi/2]} + \{(\chi' - \chi_S)(\chi_0 - \chi') + \frac{(\chi_0 - \chi_S)^2}{4\tan^2[(1-\alpha)\pi/2]}\} \qquad (8.11)$$
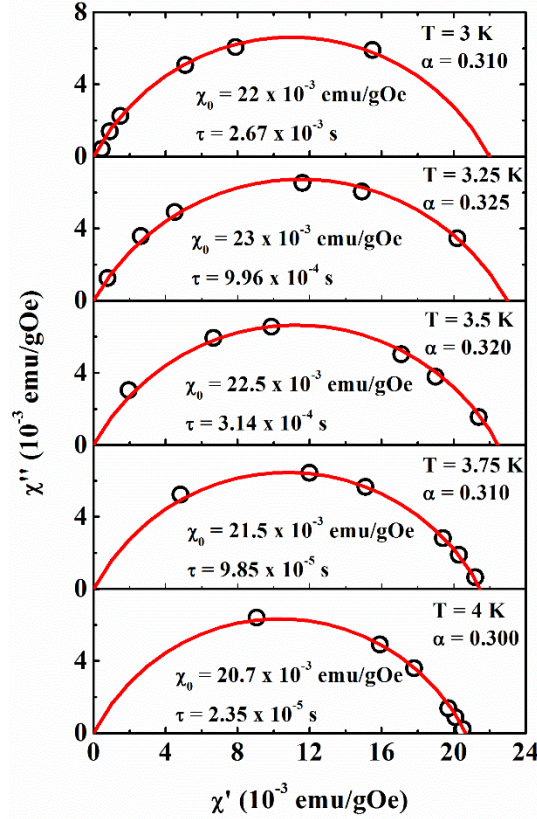
Fig. 8.16 *Cole-Cole diagram at various temperatures from 3 K to 4 K for β-MnPc. The solid lines represent least-squares fits to Eq. (8.11) with the magnitudes of the various parameters determined from the fits listed in the figure.*

For α = 0, the plot of χ" vs. χ' is a semicircle. For α > 0, the plot is an arc which becomes increasingly compressed as α increases such that for α = 1, the plot is a straight line corresponding to χ"=0. For β-MnPc, the Cole-Cole plots are shown in Fig. 8.16 for five temperatures between 3 K and 4 K with the solid lines

121

as fits to Eq. (8.11) using $\chi_S = 0$. The magnitude of $\alpha = 0.31 \pm 0.01$ signifies that there is some distribution in the relaxation time although the system is far from being a spin-glass. This distribution likely results from distribution in the length of domains along the chain length in β-MnPc as noted earlier.

The mean relaxation time τ at each temperature T was next determined from the equation for χ'' given by Eq. (8.10) using the magnitudes of α listed in Fig. 8.16 for each temperature. Assuming the Arrhenius relaxation $\tau = \tau_0\exp(\Delta E/k_B T)$, the plot of $\ln\tau$ vs. (1/T) is shown in Fig. 8.17. The plot yields a linear fit with $\tau_0 = 2.73 \times 10^{-11}$ s ($f_0 = 1/\tau_0 = 3.66 \times 10^{10}$ Hz) and $(\Delta E/k_B) = 56.0$ K. These magnitudes are in good agreement with those determined from the analysis in Fig. 8.15 assuming a single relaxation time.
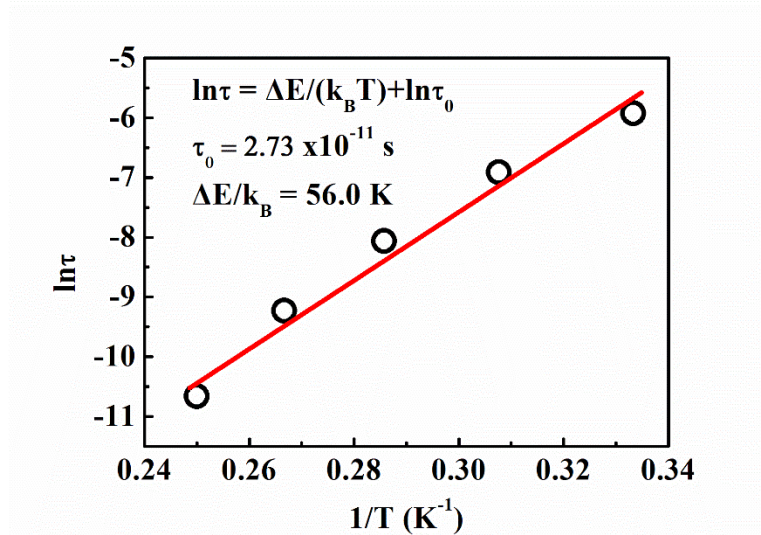
Fig. 8.17 *Determination of τ_0 and the activation energy for β-MnPc from the $\ln\tau$ vs. 1/T plot.*

8.4 Discussion

Here the major results from this chapter are summarized and briefly discussed. First, the non-saturation of M even at 90 kOe in the plot of M vs. H at 2 K in Fig. 8.9 is partly due to the fact that these measurements are on a powder sample. However, following the arguments in the papers by Mitra et

al. [5] and Awaga et al. [6], the magnetic moment in a given chain in β-MnPc is perpendicular to the molecular plane because of the single ion anisotropy D and the magnetic moments in two neighboring chains are canted away from each other with respect to the b-axis (see Fig. 8.1) This leads to four types of domains as shown in Fig. 8.10 in additions to domains along the chains resulting from the gap parameter Δ. This canting and domains hinder the rapid saturation of the magnetization as evident in Fig. 8.9.

Second, the magnitude of the saturation magnetization is calculated from $M_S = Ng\mu_B S$ where N is the number of Mn^{2+} ions per gm. Using g = 2.307 and S = 3/2 determined in this work, yields M_S = 34.05 emu/g at absolute zero, to be compared with the experimental estimate of $M_S \approx 31$ emu/g determined at 2 K in Fig. 8.9. This is considered to be a good agreement between the experimental and measured values given the limitations noted above. The close agreement for the magnitudes of f_o and $(\Delta E/k_B)$ determined using the Cole-Cole analysis of Fig. 8.17 and a single relaxation frequency of Fig. 8.15 suggests that to a good approximation, β-MnPc has a single relaxation time following Arrhenius relaxation.

Third, in the dc susceptibility measurements of Mitra et al in β-MnPc, a weak plateau in the χ vs. T data near 3 K was tentatively associated with interlayer antiferromagnetic (AFM) exchange coupling between Mn^{2+} ions but without providing any quantitative reasoning or rationale for such association [5]. In our χ vs. T data shown in Fig. 8.7 with H = 50 Oe, a peak is clearly noticeable near 2.5 K. However comparing this with our data from ac susceptibilities in Figs. 8.13 and 8.14, this peak is likely associated with the relaxation phenomenon discussed in Section 7.3.6 above. Thus we can rule out the presence of interlayer AFM exchange coupling which, if present, would make the moments in the neighboring chains

align in opposite directions and lead to 3D long range ordering at a specific temperature as observed in linear ferromagnetic chain system $CoNb_2O_6$ [37]. In $CoNb_2O_6$, in addition to the presence of ferromagnetic intra-layer exchange coupling between the Co^{2+} ions with spin S =1/2, significant antiferromagnetic interlayer exchange coupling is also present leading to complex H-T phase diagram with transitions at 2.95 K and 1.97 K. Importantly, these transitions are accompanied by peaks in χ vs. T and C vs T data making $CoNb_2O_6$ a quasi-one-dimensional Ising ferromagnet [37]. In contrast, results in β-MnPc with spin S = 3/2 for Mn^{2+} ions show absence of peaks in the temperature dependence of χ, χ', and χ'' near the presumed $T_C \approx 8$ K and. Furthermore, in the C vs. T data, only a broad peak at around 12 K is observed (Fig. 8.12). As noted earlier, the neutron diffraction measurements at 5 K by Figgs et al [27] showed no clear evidence for magnetic contributions to Bragg intensities. Moreover, unlike in $CoNb_2O_6$, in β-MnPc there is no evidence for any field induced transition in the M vs. H data of Fig. 8.9 at least up to about 90 kOe. Also, the calculated saturation magnetization for complete alignments of the moments is very close to the measured value of Fig. 8.9.

Finally, as noted earlier, the deviation of the χ vs. T behavior below 6 K from Eq. (8.2) of the Ising chain model is likely due to domains resulting from the presence of single ion anisotropy and energy gap $\Delta/k_B = 65.5$ K [20]. These results show that β-MnPc is a one-dimensional Ising-like chain magnet with strong single ion anisotropy but without three-dimensional long range magnetic ordering. This conclusion represents a major departure from results presented in previous investigations of β-MnPc [1-7] and so it is an important contribution of this work. This work has also demonstrated the importance of a careful use of the ac susceptibilities in determining the nature of magnetism in a variety of materials.

8.5 Conclusions

The major conclusions from the results presented in this chapter are as follows:(i) The electronic state of Mn^{2+} in β-MnPc with $3d^5$ electrons has the effective spin S = 3/2 violating Hunds' rules; (ii) The fits of the magnetic susceptibility versus temperature data to the Curie-Weiss law yields θ = 12.3 K, μ = 4.467 $μ_B$, and g = 2.307 for spin S = 3/2 for β-MnPc; (iii) The magnetic susceptibility versus temperature data fits well to the Ising linear chain model yielding exchange constant J_{ex}/k_B = 2.6 K; (iv)The magnitude of single ion anisotropy constant $|D|/k_B$ = 8.3 K is determined and its magnitude being larger than the exchange constant J_{ex}/k_B = 2.6 K is crucial since it explains the lack of the 3D magnetic ordering in this system and also the alignment of the magnetic moments perpendicular to the molecular planes as shown in Fig. 8.2; (v)The lack of 3D ordering in β-MnPc is also supported by the Arrott plots and the reported measurements of , specific heat and neutron scattering; (vi) The Cole-Cole analysis of the frequency dependence of $χ''$ (ω) and $χ'$ (ω) suggests β-MnPc has a single relaxation time with some distribution; and finally (vii) it si shown that β-MnPc can be best described as an Ising-like chain magnet with Arrhenius relaxation of the magnetization governed by an intra-layer ferromagnetic exchange constant J_{ex}/k_B = 2.6 K and the single ion anisotropy energy parameter $|D|/k_B$ = 8.3 K.

References

[1] C.G. Barraclough, R.L. Marti, S. Mitra and R.C. Sherwood, J. Chem. Phys. **53**, 1638 (1970).

[2] C.G. Barraclough, A.K. Gregson and S. Mitra, J. Chem. Phys. **60**, 962 (1974).

[3] H. Miyoshi, H. Ohya-Nishiguchi and Y. Deguchi, Bull. Chem. Soc. Japan. **46**, 2724 (1973).

[4] H. Miyoshi, Bull. Chem. Soc. Japan. **47**, 561 (1974).

[5] S. Mitra, A.P. Oregson, W.E. Hatfield and R.R. Weller, Inorg. Chem. **22**, 1729 (1983).

[6] K. Awaga and Y. Maruyama, Phys. Rev. B. **44**, 2589 (1991).

[7] H. Yamada, T. Shimada and A. Koma, J. Chem. Phys. **108**, 10256 (1998).

[8] Y. Taguchi, T. Miyake, S. Margadonna, K. Kato, K. Prassides and Y. Iwasa, J. Magn. Magn. Mater. **310**, 1229 (2007).

[9] Y. Taguchi, T. Miyake, S. Margadonna, K. Kato, K. Prassides and Y. Iwasa, J. Am. Chem. Soc. **128**, 3313 (2006).

[10] T. Moriya, Phys. Rev. **117**, 635 (1960).

[11] Z. Wang and M.S. Seehra, J. Phys.: Condens. Matter. **28**, 136002 (2016).

[12] R. Mason, G.A. Williams and P.E. Fielding, J. Chem. Soc. Dalton Trans. **4**, 676 (1979).

[13] W. Wu, A. Kerridge, A.H. Harker and A.J. Fisher, Phys. Rev. B. **77**, 184403 (2008).

[14] W. Wu, A.J. Fisher and N.M. Harrison, Phys. Rev. B. **84**, 024427 (2011).

[15] W. Wu, N.M. Harrison and A.J. Fisher, Phys. Rev. B. **88**, 024426 (2013).

[16] I.E. Brumbiou et al, J. Phys. Chem. A. **118**, 927 (2014).

[17] Z. Wang, M. Lee, E.S. Choi, J. Poston and M.S. Seehra, J. Magn. Magn. Mater. **407**, 83 (2016).

[18] J.C. Bonner and M.E. Fisher, Phys. Rev. **135**, A640 (1964).

[19] Z. Wang, K.L. Pisane and M.S. Seehra, IEEE Trans. Magn. **51**, 2700104 (2015).

[20] C. Coulon, H. Miyasaka and R. Clerac, Struct. Bond. **122**, 163 (2006).

[21] M.E. Fisher, J. Math. Phys. **4**, 124 (1963).

[22] H.E. Stanley, "Introduction to Phase Transitions and Critical Phenomena" (Oxford University Press., New York 1971) page 167.

[23] A. Arrott, Phys. Rev. **108**, 1394 (1957).

[24] I. Yeung, R. Roshko and G. Williams, Phys. Rev. B. **34**, 3456 (1986).

[25] V.S. Babu, A.S. Pavlovic and M.S. Seehra, J. Appl. Phys. **79**, 5230 (1996).

[26] V. Narang, D. Korakakis and M.S. Seehra, J. Magn. Magn. Mater. **368**, 353 (2014).

[27] B.N. Figgs, R. Mason and G.A. Williams, Acta Cryst. B. **36**, 2963 (1980).

[28] J-O. Andersson, C. Djurberg, T. Jonsson, P. Svedlindh and P. Noldblad, Phys. Rev. B. **56**, 13983 (1997).

[29] V. Singh, M.S. Seehra and J. Bonevich, J. Appl. Phys. **105**, 07B518 (2009).

[30] K.L. Pisane, E.C. Despeaux and M.S. Seehra, J. Magn. Magn. Mater. **384**, 148 (2015).

[31] J.L. Dormann, L. Bessais and D. Fiorani, J. Phys. C. **21**, 2015 (1988).

[32] R.J. Glauber, J. Math. Phys. **4**, 294 (1963).

[33] H. Miyasaka, R. Clerac, K. Mizushinma, K. Sugiura, M. Yamashita, W. Wernsdorfer and C. Coulon, Inorg. Chem. **42**, 8203 (2003).

[34] K.S. Cole and R.H. Cole, J. Chem. Phys. **9**, 341 (1941).

[35] M. Balanda, Act Phys. Pol. A. **124**, 964 (2013).

[36] M. Hagiwara, J. Magn. Magn. Mater. **177-181**, 89 (1998).

[37] T. Liang, S.M. Koohpayeh, J.W. Krizan, T.M. McQueen, R.J. Cava and N.P. Ong, Nat. Commun. **6**, 7611 (2015).

CHAPTER 9.

Conclusions, Future Directions, Publications and Presentations

9.1 Conclusions:

Detailed investigations of the magnetic properties of transition-metal phthalocyanines $(C_{32}H_{16}N_8TM)$ with TM = VO, Mn, Co, Ni, and Cu have been presented in this dissertation. Using the analysis of the temperature and magnetic field dependence of the magnetization and ac susceptibilities, the focus was on determining the electronic states of the TM ions, the magnitude and sign of the exchange coupling between the TM ions and the nature of magnetic ordering, if any, in these systems. These results are summarized in Table 9.1. For β-MnPc, β-NiPc and β-CoPc, the resulting electronic states violate the Hunds' rules, the reasons for which are discussed at appropriate places in the dissertation. The exchange coupling between the TM ions in α-CuPc, β-CuPc, β-CoPc and VOPc is antiferromagnetic whereas it is ferromagnetic in β-MnPc.

Regarding the nature of magnetic ordering in these systems, α-CuPc, β-CuPc, β-CoPc and VOPc are shown to be Heisenberg linear chain systems with measurable intra-chain exchange coupling (see Table 9.1) but no inter-chain coupling. Consequently 3-dimensional magnetic ordering is absent. For β-NiPc, the effective spin S = 0 makes this material a diamagnetic although the sample of β-NiPc investigated in this work is shown to have Fe-based ferromagnetic impurity with concentration less than 0.2%.

Table 9.1 *Major results of this dissertation. Notice that AFM, DM, and FM represent antiferromagnetic, diamagnetic, and ferromagnetic respectively.*

	Electronic configuration	Electronic state	Spin	Nature of spin coupling	J_{ex}/k_B (K)	Heisenberg chain/Ising chain	g-value
α-CuPc	$3d^9$	Cu^{2+}	1/2	AFM	- 1.7	Heisenberg	2.21
β-CuPc	$3d^9$	Cu^{2+}	1/2	AFM	- 0.2	Heisenberg	2.10
β-CoPc	$3d^7$	Co^{2+}	1/2	AFM	- 1.5	Heisenberg	2.49
VOPc	$3d^1$	V^{4+}	1/2	AFM	- 0.077	Heisenberg	1.967
β-NiPc	$3d^8$	Ni^{2+}	0	DM			
β-MnPc	$3d^5$	Mn^{2+}	3/2	FM	2.6	Ising-like	2.307

The case of β-MnPc is unusual among the TMPc systems not only because of the ferromagnetic exchange coupling between the Mn^{2+} ions but also because several previous studies had reported it to be a canted ferromagnet with $T_C \approx 9$ K. However analysis of the ac and dc magnetic susceptibilities of β-MnPc presented in this dissertation has ruled out the presence of 3-dimensional ferromagnetic ordering in β-MnPc. Instead the system is shown to be Ising-like chain with intra-chain ferromagnetic coupling with the presence of domains. This is one of the important contributions of their work. A remaining theoretical

question which is not yet answered is why the exchange coupling is ferromagnetic in β-MnPc in contrast to the antiferromagnetic coupling in the other TMPc systems. The role of single ion anisotropy present in β-MnPc but absent in other TMPc system is shown to be very important for the lack of 3-dimensional ordering in β-MnPc. Therefore it is speculated that the single ion anisotropy may also have some role in making the exchange coupling in β-MnPc ferromagnetic.

9.2 Future Directions:

A few suggestions for possible future research in transition metal phthalocynanines are listed below:

(1) Although the exchange constant J_{ex}/k_B was obtained accurately by fitting the χ vs. T data to the Bonner-Fisher model (for α-CuPc, β-CuPc, and β-CoPc) or the Ising linear chain model (for β-MnPc), more theoretical work is needed to explain the sources of the exchange coupling: direct coupling, super-exchange coupling, or both.

(2) Theoretical work is needed to explain why the exchange coupling in β-MnPc is ferromagnetic in contrast to the antiferromagnetic coupling in other TMPc systems.

(3) In order to exploit TMPc for practical applications as organic semiconductors, additional experimental investigations using high-quality thin films of TMPc and their appropriate testing and characterization can be carried out. Previous studies reported in the thin films of some of these TMPc systems are referenced at appropriate places in this dissertation.

(4) One of the interesting aspects of TMPc systems is the variety in crystal structures leading to different phases such as α, β, γ, etc. Investigations of the magnetism for these phases could be carried out if these different could be stabilized and good quality samples could be prepared.

(5) Since the TMPc structure is planar and so highly anisotropic, their magnetic properties are likely to be quite anisotropic also. To investigate this anisotropy, magnetic studies in single crystals with magnetic field applied along different crystallographic directions are needed. Some initial studies in tiny single crystals of β-MnPc were reported by Mitra et al (see Fig. 8.9). However, techniques need to be developed to grow large single crystals of the TMPc systems which will allow measurements of these magnetic anisotropies more accurately.

9.3 Publications and Presentations:

Below, publications in refereed journals and presentations made at professional meetings by the author are listed.

9.3.1 Publications

[1] **Z. Wang**, K. L. Pisane, and M. S. Seehra, *Magnetic determination of the electronic state of Cu and exchange interactions in the α- and β-phases of molecular semiconductor Copper Phthalocyanine ($C_{32}H_{16}N_8Cu$)*, IEEE. Trans. Magn. **51**, 2700104/1-4 (2015).

[2] **Z. Wang**, M. Lee, E.S. Choi, J. Poston, and M.S. Seehra, *Low temperature, high magnetic field investigations of the nature of magnetism in the molecular semiconductor β-Cobalt Phthalocyanine ($C_{32}H_{16}CoN_8$)*, J. Magn. Magn. Mater. **407**, 83-86 (2016).

[3] **Z. Wang** and M.S. Seehra, *Ising-like chain magnetism, Arrhenius magnetic relaxation, and case against 3D magnetic ordering in β-Manganese Phthalocyanine ($C_{32}H_{16}MnN_8$)*, J. Phys. Condens. Matter. **28**, 136002/1-9, (2016).

[4] **Z. Wang**, L. Pi, and M.S. Seehra, *Magnetic studies reveal near-perfect paramagnetism in the molecular semiconductor Vanadyl phthalocyanine ($C_{32}H_{16}N_8VO$).* (under review).

[5]. **Z. Wang** and M. S. Seehra, Nature of magnetic ordering and exchange interactions in the layered *β-Co(OH)$_2$.* (in preparation).

[6] **Z. Wang**, K. Sierros, D. Korakakis, and M.S. Seehra, *Development of indigo-based nonvolatile write-once-read-many-times memory device*. (in preparation).

9.3.2. Conference Presentations

[1] **Z. Wang** and M.S. Seehra, *Unusual features of magnetism in transition-metal-doped phthalocyanines $C_{32}H_{16}N_8TM$ (TM = Mn, Fe, Co, Ni, Cu)*, APS March Meeting, Baltimore, Mar. 2016.

[2] **Z. Wang**, L. Pi, and M.S. Seehra, *Magnetic studies reveal near-perfect paramagnetism in the molecular semiconductor Vanadyl phthalocyanine ($C_{32}H_{16}N_8VO$)*, APS March Meeting, Baltimore, Mar. 2016.

[3] **Z. Wang** and M. S. Seehra, *Ising chain magnetism and Arrhenius magnetic relaxation in the molecular semiconductor β-manganese phthalocyanine ($C_{32}H_{16}MnN_8$)*, MMM-Intermag Joint Conference,

San Diego, USA, Jan. 2016.

[4] **Z. Wang**, M. Lee, E.S. Choi, J. Poston, and M.S. Seehra, *Nature of magnetism in the molecular semiconductor Cobalt Phthalocyanine ($C_{32}H_{16}CoN_8$): low temperature, high magnetic field invstigations*, PPHMF-8, Tallahassee, USA, Jan. 2015.

[5] **Z. Wang**, M. Lee, E.S. Choi, J. Poston, and M.S. Seehra, *Nature of magnetism in the molecular semiconductor cobalt phthalocyanine ($C_{32}H_{16}CoN_8$): low temperature, high magnetic field investigations*, APS Mid-Atlantic Meeting, Morgantown, USA, Oct. 2015.

[6] **Z. Wang**, K. Sierros, M.S. Seehra, and D. Korakakis, *Development of write-once-read-many-times memory device based on biodegradable indigo*, 57th Electronic Materials Conference, Columbus, USA, June 2015.

[7] **Z. Wang**, K. L. Pisane, and M. S. Seehra, *Magnetic determination of the electronic state of Cu and exchange interactions in the α- and β-phases of molecular semiconductor Copper Phthalocyanine ($C_{32}H_{16}N_8Cu$)*, Intermag Conference, Beijing, China, May 2015.

[8] **Z. Wang**, K. L. Pisane, K. Sierros, M. S. Seehra, and D. Korakakis, *Device applications and structural and optical properties of Indigo –A biodegradable, low-cost organic semiconductor*, APS March Meeting, San Antonio, USA, Mar. 2015.

[9] **Z. Wang**, K. Sierros, D. Korakakis, M. S. Seehra, *Indigo – A biodegradable, low-cost organic semiconductor for device applications*, APS Mid-Atlantic Meeting, State College, USA, Oct. 2014.

APPENDIX A.

Proposal Submitted to NHMFL

Proposal Title: Understanding the nature of magnetism in transition-metal substituted phthalocyanines through high-field, low-temperature magnetic measurements at the NHMFL

PI: Mohindar S. Seehra, Ph.D., Eberly Distinguished Professor Emeritus & Research Professor, West Virginia University, Morgantown, WV. Email: mseehra@wvu.edu

Co-investigator: Zhengjun Wang, Ph.D. student at West Virginia University (WVU) working with the PI. Zhengjun will carry out the proposed experiments at the NHMFL;

Email: zwang3@mix.wvu.edu

A.1. Background

Transition-metal-substituted phthalocyanines (MPc, M =Mn, Fe, Co, Ni and Cu) with the formula $C_{32}H_{16}N_8M$ represent a family of planar molecular magnetic materials with semiconducting properties and strong optical absorption in the uv-visible range. Consequently they are being investigated for potential applications in solar cells, organic LEDs, transistors, gas sensors and storage devices [1, 2]. Also, the electronic structure of MPc has become of particular recent interest for applications in spintronics [3]. Recent work using density functional theory and scanning tunneling microscopy of MPc adsorbed on Ag (100) surface has indicated inadequacy of the Hunds' Rules to predict the electronic and magnetic properties of the transition metal dopants in MPc [4,5]. Therefore, thorough investigations of their magnetic properties covering a wide temperature range and high magnetic fields are needed to fully

understand the nature of magnetism in the MPc system. The experiments proposed here using the low temperature, high field facilities of the NHFML will supplement the experimental work being done at West Virginia University.

A.2. Initial studies at WVU and need for the use of facilities at the NHMFL:

The powder samples of MPc being used here were acquired from commercial sources and annealed in some cases to produce the proper crystalline phase (α-phase and β-phase). X-ray diffraction is used to verify/establish the crystalline phase of the material before magnetic measurements are undertaken. The magnetic measurements at WVU are being performed employing a physical property measurement system (PPMS) acquired from Quantum Design Inc. Because of the limitations of the PPMS, these measurements of the magnetization M cover the temperature range of 2 K to 350 K and magnetic fields up to 90 kOe (9 T) only. As discussed below, measurements down to 0.1 K and in magnetic fields up to 18 T are needed to fully understand and interpret the nature of magnetism in these materials.

Recently, results from our initial studies of the magnetic properties of the α- and β-phase of CuPc were accepted for presentation at the Intermag 2015 Conf. to be held in Beijing, China during May 2015. A manuscript on this work has also been submitted for publication in the conference proceedings to be published in IEEE Transaction on Magnetics [6]. These measurements were interpreted in terms of the Bonner-Fisher model of Heisenberg linear chain [7]. As shown in Fig. A.1, in α-CuPc we could barely observe the maximum in M vs. T predicted by this model near 2.2 K whereas the predicted position of the maximum in β-CuPc is around 0.25 K. Therefore measurements down to about 0.1 K are needed to verify

this model. In the M vs. H measurements at 2 K in α-CuPc, M is not saturated even at 90 kOe. Although

our calculations and fit to the data did yield intra-chain exchange constant J_{ex}/k_B = 3.4 K (0.4 K) in

α-CuPc (β-CuPc) with Cu^{2+} electronic state, measurements down to 0.1 K and in H up to 18 kOe will

convincingly validate the model.

In MnPc, CoPc and FePc, some initial measurements of M vs. T down to 2 K (Fig. A.2) and M

vs. H up to 9 kOe (Fig. A.3) have also been done. No maximum in M vs. T is observed down to 2 K and

M at 2 K is not saturated for H up to 9 kOe. Although these data are not yet analyzed, it is evident that

measurements to lower T and higher H values will be essential for understanding the nature of magnetism

in these materials. This is the motivation for the proposed experiments using the facilities of the NHMFL.

Specific details of these proposed experiments are given below.
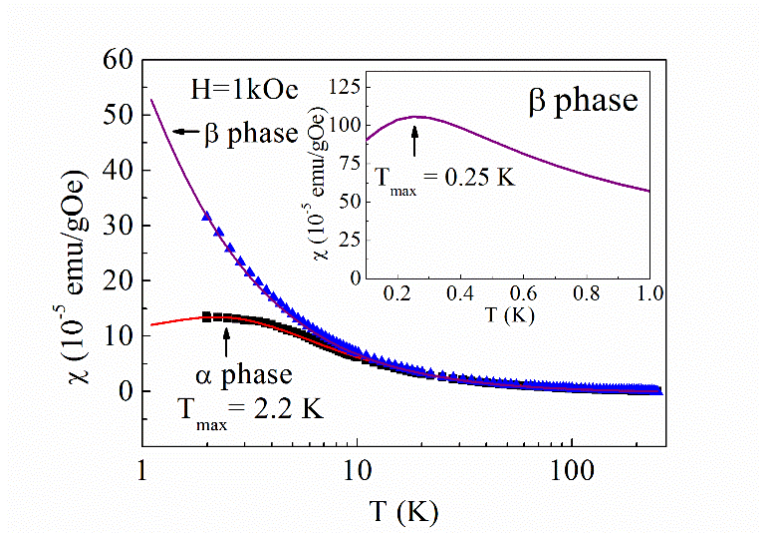
Fig. A.1 *The data of χ vs. T for the α- and β-phase of CuPc are fitted to Bonner-Fisher model with the solid lines as fits yielding the exchange constant J_{ex}/k_B=3.4 K (0.4 K) for α (β) phase. The fit also gives T_{max} = 2.2 K for α-phase and calculated T_{max} = 0.25 K for β-phase (see inset).*
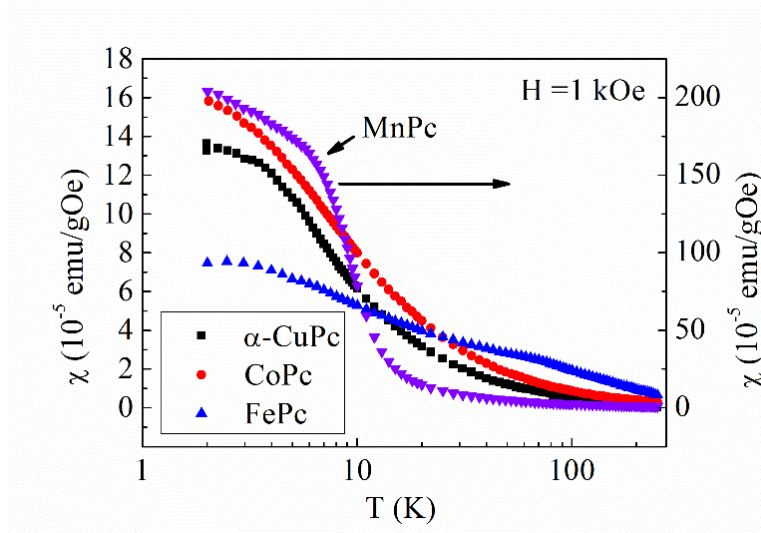
Fig. A.2 *Magnetic susceptibility (χ) vs. temperature (T) of α-CuPc, MnPc, FePc and CoPc measured in the applied magnetic field of 1 kOe.*
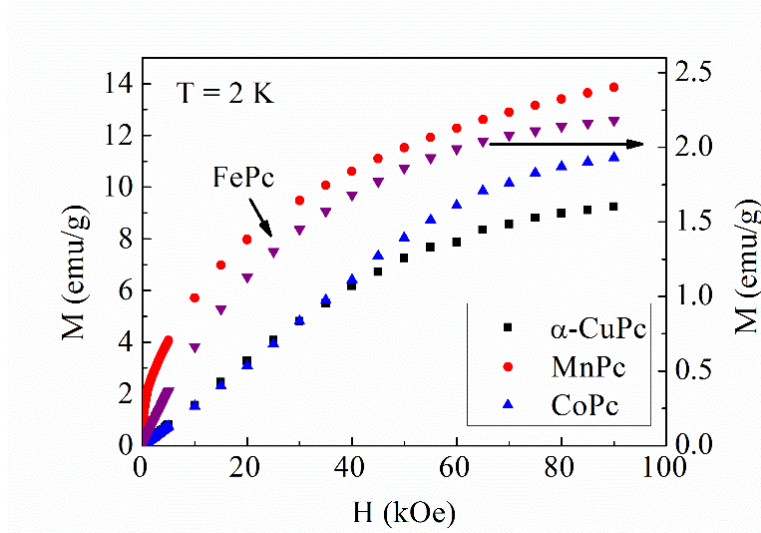
Fig. A.3 *Magnetization (M) vs. magnetic field (H) data of α-CuPc, MnPc, CoPc, and FePc at 2 K. Note the lack of saturation of M even at 90 kOe.*

A.3. Specifics of the proposed experiments:

The goal of our project is to measure magnetization M in the MPc samples (M = Cu, Mn, Co, Fe) in the temperature range of 0.1 K to about 10 K in close temperature intervals and isothermal

measurements M vs. H using H up to 18 T at a low temperature, say 1 K. These new set of data will supplement the data taken at WVU covering the temperature range of 2 K to 300 K and using H up to 9 T. Our search of the different magnet systems available at the NHMFL suggest that the SCM1 magnet system may be most appropriate for our needs although we are certainly open to other suggestions from the staff at the NHMFL. Considering one day devoted to each sample, it is anticipated that a five day window might be the appropriate time frame needed for our experiments. Since Mr. Wang does not have prior experience working at the NHMFL, he will need guidance and assistance in doing these measurements. In a previous project carried out by my graduate student James Rall at the NHMFL, Dr. E.S. Choi was our collaborator.

References

[1] N. McKeown., Phthalocyanine Materials: Synthesis, Structure and Function. Cambridge, U.K.: Cambridge University Press (1998).

[2] L. Lozzi, S. Santucci, S. La Rosa, B. Delley, S. Picozzi., J. Chem. Phys, **121**, 1883-1889 (2004).

[3] M. Warner., et al., Nature, **503**, 504-508 (2013).

[4] A. Mugarza., et al., Phys. Rev. B, **85**, 155437/1-13 (2012).

[5] W. Wu, N. M. Harrison, A. J. Fisher., Phys. Rev. B, **88**, 024426/1-9 (2013).

[6] Z. Wang, K. L. Pisane, M. S. Seehra., "Magnetic determination of the electronic state of Cu and

exchange interactions in the α- and β-phases of molecular semiconductor Copper Phthalocyanine ($C_{32}H_{16}N_8Cu$)", IEEE. Trans. Magn. (submitted).

[7] J. C. Bonner, M. E. Fisher., Phys. Rev, **135**, A640-A658 (1964).

<center>**APPENDIX B.**</center>

<center>**ACMS Sequences**</center>

This appendix lists three typical magnetization measurement sequences. Additional details are available in the PPMS ACMS User's Manual [1].

B.1 Zero-field-cool and Field-cool (ZFC-FC) DC Magnetization Measurement from 2 K to 350 K with H = 1 kOe:

Set Temperature 10K at 10K/min. Fast Settle

Wait For Temperature, Delay 3600 secs, No Action

Set Temperature 2K at 5K/min. Fast Settle

Wait For Temperature, Delay 3600 secs, No Action

ACMS Locate at 10 Oe 1000 Hz

Set Magnetic Field 1000.0Oe at 100.0Oe/sec, Linear, Persistent

Wait For Field, Delay 0 secs, No Action

****** ZFC M vs T ************

Scan Temp from 2K to 60K at 2K/min, in 59 steps, Uniform, No O'Shoot

    DC Mag 5 Scans Stickyrange Flags=33554439

<center>141</center>

End Scan

Scan Temp from 62K to 100K at 2K/min, in 20 steps, Uniform, No O'Shoot

    DC Mag 5 Scans Stickyrange Flags=33554439

End Scan

Scan Temp from 105K to 350K at 4K/min, in 128 steps, Uniform, No O'Shoot

    DC Mag 5 Scans Stickyrange Flags=33554439

End Scan

*********FC M vs T*********

Set Temperature 10K at 10K/min. Fast Settle

Wait For Temperature, Delay 3600 secs, No Action

Set Temperature 2K at 5K/min. Fast Settle

Wait For Temperature, Delay 3600 secs, No Action

Scan Temp from 2K to 60K at 2K/min, in 59 steps, Uniform, No O'Shoot

    DC Mag 5 Scans Stickyrange Flags=33554439

End Scan

Scan Temp from 62K to 100K at 2K/min, in 20 steps, Uniform, No O'Shoot

DC Mag 5 Scans Stickyrange Flags=33554439

End Scan

Scan Temp from 105K to 350K at 4K/min, in 128 steps, Uniform, No O'Shoot

DC Mag 5 Scans Stickyrange Flags=33554439

End Scan

Set Magnetic Field 0.0Oe at 100.0Oe/sec, Oscillate, Persistent

Wait For Field, Delay 0 secs, No Action

Set Temperature 100K at 10K/min. Fast Settle

Wait For Temperature, Delay 3600 secs, No Action

B.2 Magnetic Hysteresis Loop (between – 90 kOe to 90 kOe) at 2 K:

Set Temperature 10K at 10K/min. Fast Settle

Wait For Temperature, Delay 3600 secs, No Action

Set Temperature 2K at 5K/min. Fast Settle

Wait For Temperature, Delay 3600 secs, No Action

ACMS Locate at 10 Oe 1000 Hz

*** M vs H at 2 K****

Scan Field from 0.0Oe to 100.0Oe at 100.0Oe/sec, in 11 steps, Uniform, Linear, Persistent

    DC Mag 5 Scans Stickyrange Flags=33554439

End Scan

Scan Field from 150.0Oe to 950.0Oe at 100.0Oe/sec, in 17 steps, Uniform, Linear, Persistent

    DC Mag 5 Scans Stickyrange Flags=33554439

End Scan

Scan Field from 1000.0Oe to 5000.0Oe at 100.0Oe/sec, in 41 steps, Uniform, Linear, Persistent

    DC Mag 5 Scans Stickyrange Flags=33554439

End Scan

Scan Field from 10000.0Oe to 90000.0Oe at 100.0Oe/sec, in 17 steps, Uniform, Linear, Persistent

    DC Mag 5 Scans Stickyrange Flags=33554439

End Scan

Scan Field from 85000.0Oe to 10000.0Oe at 100.0Oe/sec, in 16 steps, Uniform, Linear, Persistent

    DC Mag 5 Scans Stickyrange Flags=33554439

End Scan

Scan Field from 5000.0Oe to 1000.0Oe at 100.0Oe/sec, in 41 steps, Uniform, Linear, Persistent

    DC Mag 5 Scans Stickyrange Flags=33554439

End Scan

Scan Field from 950.0Oe to 150.0Oe at 100.0Oe/sec, in 17 steps, Uniform, Linear, Persistent

    DC Mag 5 Scans Stickyrange Flags=33554439

End Scan

Scan Field from 100.0Oe to -100.0Oe at 100.0Oe/sec, in 21 steps, Uniform, Linear, Persistent

    DC Mag 5 Scans Stickyrange Flags=33554439

End Scan

Scan Field from -150.0Oe to -950.0Oe at 100.0Oe/sec, in 17 steps, Uniform, Linear, Persistent

    DC Mag 5 Scans Stickyrange Flags=33554439

End Scan

Scan Field from -1000.0Oe to -5000.0Oe at 100.0Oe/sec, in 41 steps, Uniform, Linear, Persistent

    DC Mag 5 Scans Stickyrange Flags=33554439

End Scan

Scan Field from -10000.0Oe to -90000.0Oe at 100.0Oe/sec, in 17 steps, Uniform, Linear, Persistent

DC Mag 5 Scans Stickyrange Flags=33554439

End Scan

Scan Field from -85000.0Oe to -10000.0Oe at 100.0Oe/sec, in 16 steps, Uniform, Linear, Persistent

DC Mag 5 Scans Stickyrange Flags=33554439

End Scan

Scan Field from -5000.0Oe to -1000.0Oe at 100.0Oe/sec, in 41 steps, Uniform, Linear, Persistent

DC Mag 5 Scans Stickyrange Flags=33554439

End Scan

Scan Field from -950.0Oe to -150.0Oe at 100.0Oe/sec, in 17 steps, Uniform, Linear, Persistent

DC Mag 5 Scans Stickyrange Flags=33554439

End Scan

Scan Field from -100.0Oe to 100.0Oe at 100.0Oe/sec, in 21 steps, Uniform, Linear, Persistent

DC Mag 5 Scans Stickyrange Flags=33554439

End Scan

Scan Field from 150.0Oe to 950.0Oe at 100.0Oe/sec, in 17 steps, Uniform, Linear, Persistent

DC Mag 5 Scans Stickyrange Flags=33554439

End Scan

Scan Field from 1000.0Oe to 5000.0Oe at 100.0Oe/sec, in 41 steps, Uniform, Linear, Persistent

DC Mag 5 Scans Stickyrange Flags=33554439

End Scan

Scan Field from 10000.0Oe to 90000.0Oe at 100.0Oe/sec, in 17 steps, Uniform, Linear, Persistent

DC Mag 5 Scans Stickyrange Flags=33554439

End Scan

Set Magnetic Field 5000.0Oe at 100.0Oe/sec, Linear, Persistent

Wait For Field, Delay 0 secs, No Action

Set Magnetic Field 0.0Oe at 100.0Oe/sec, Oscillate, Persistent

Wait For Field, Delay 0 secs, No Action

Set Temperature 300K at 10K/min. Fast Settle

Wait For Temperature, Delay 3600 secs, No Action

B.3. AC Magnetization Measurement from 2 K to 20 K with H$_{dc}$ = 0 Oe and H$_{ac}$ = 5 Oe, the AC field frequencies are: 11.3 Hz, 53.1 Hz, 101.4 Hz, 511.3 Hz, 1055.6 Hz, 3005.7 Hz, 5011.5 Hz, 7092.4 Hz, and 9013.5 Hz.

Set Temperature 45K at 10K/min. Fast Settle

Wait For Temperature, Delay 3600 secs, No Action

Set Temperature 2K at 20K/min. Fast Settle

Wait For Temperature, Delay 1800 secs, No Action

ACMS Locate at 10 Oe 1000 Hz

Scan Temp from 2K to 20K at 1K/min, in 41 steps, Uniform, No O'Shoot

    AC Mag 5 Oe 11.3, 53.1, 101.4, 511.3, 1055.6, 3005.7, 5011.5, 7092.4, 9013.5 Hz 1 Sec Stickyrange

Flags=33554439

End Scan

Set Temperature 300K at 10K/min. Fast Settle

Wait For Temperature, Delay 3600 secs, No Action

Reference

[1] PPMS ACMS User's Manual, Quantum Design Inc.